DETECTION AND ATTRIBUTION OF COMPOUND HYDROMETEOROLOGICAL EXTREMES

YOU JIEWEN

PhD

The Hong Kong Polytechnic University

2024

The Hong Kong Polytechnic University

Department of Land Surveying and Geo-Informatics

Detection and Attribution of Compound Hydrometeorological Extremes

YOU Jiewen

A Thesis

Submitted in Partial Fulfilment of the Requirements

for the Degree of Doctor of Philosophy

April 2024

CERTIFICATE OF ORIGINALITY

I hereby declare that this thesis is my own work and that, to the best of my knowledge and belief, it reproduces no material previously published or written, nor material that has been accepted for the award of any other degree or diploma, except where due acknowledgement has been made in the text.

(Signed)

YOU, Jiewen (Name of student)

Abstract

Compound hydrometeorological extremes refer to the simultaneous or sequential occurrence of multiple climate drivers and hazards (especially floods and heat waves). These compound events often have more severe consequences compared to when these disasters occur individually. Therefore, detecting and understanding compound hydrometeorological extremes are crucial for formulating effective adaptation and mitigation strategies to address the threats posed by climate warming.

Although research on the detection and attribution of compound hydrometeorological extremes has received increasing attention in recent years, certain limitations still exist in previous studies. (1) Sparse in-situ tide gauge stations restrict the continuous spatiotemporal assessment of compound flood risk; (2) Despite extensive studies on individual phenomena, the potential lagged dependence between heat waves and heavy rainfall is often overlooked; (3) Knowledge about emerging compound events, particularly humid heat and pluvial flooding, remains poorly understood on a global scale.

To address these limitations, innovative methodologies have been developed for a comprehensive assessment of compound hydrometeorological extremes, focusing particularly on compound flood hazards and compound heat-flood hazards. (1) A vine copula ensemble machine learning, combined with a Bayesian hierarchical model is proposed for predicting compound flood risk at ungauged sites. (2) Detection, attribution, and projection methods are employed to address the frequently overlooked lagged dependence between heatwaves and heavy rainfall. (3) A comprehensive global analysis of emerging compound humid heat and pluvial flood events is conducted to improve the understanding of compound hazards using innovative methods for robust detection and attribution.

The key findings include: (1) The vine copula ensemble model outperforms traditional methods, showing 29.09% and 19.35% improvements in two datasets. The Bayesian hierarchical model effectively predicts storm surges at ungauged stations with about 11% error. Compound flooding analysis reveals 14.54% of extreme storm surges in Hong Kong coincided with heavy rainfall. (2) In China, 22% of land areas experienced statistically significant consecutive heat wave

and heavy rainfall events within 7 days. The shorter and hotter heat waves are more likely to be followed by heavy rainfall. This phenomenon is associated with atmospheric convection and moisture convergence, with projections showing increased frequency and abruptness throughout the 21st century. (3) Global, successive heat-pluvial and pluvial-heat occurred more frequently than expected by chance, with a 20% per decade increase due to warming. These events are associated with vapor pressure deficit anomalies.

The findings of this dissertation enhance the understanding of compound hydrometeorological extremes. The probabilistic and continuous estimation of compound flooding advances methodologies in flood risk assessment, emphasizing the importance of addressing multi-hazard flood risks in coastal cities. The investigations into consecutive heat wave and heavy rainfall events provide insights into mitigating or eliminating the impacts of these back-to-back extreme events. The global analysis of compound humid heat and pluvial flooding extremes highlights the need for strategies to cope with overlapping vulnerabilities due to compound hot and wet extremes, particularly in areas prone to such events.

Keywords: Climate change; Compound hydrometeorological extremes; Storm surges; Pluvial flooding; Extreme heat

List of Publications

[1] **You, J.**, & Wang, S. (2021). Higher probability of occurrence of hotter and shorter heat waves followed by heavy rainfall. *Geophysical Research Letters*, *48*(17), e2021GL094831. https://doi.org/10.1029/2021GL094831

[2] **You, J.**, Wang, S., Zhang, B., Raymond, C., & Matthews, T. (2023). Growing Threats from Swings Between Hot and Wet Extremes in a Warmer World. *Geophysical Research Letters*, *50*(14), e2023GL104075. https://doi.org/10.1029/2023GL104075

[3] **You, J.**, Wang, S., Zhang, B., Moradkhani H. (2023). Spatiotemporal Prediction of Continuous Storm Surge Extremes along China's Coastline: A Probabilistic Data-Driven Approach. *Water Resources Research*, under revision.

[4] **You, J.**, Wang, S., Zhang, B (2024). Spatially Seamless and Temporally Continuous Assessment on Compound Flood Risk. *Journal of Hydrology*, under review (minor revision).

Acknowledgements

In finishing this significant phase of my life, my doctoral dissertation, I'm filled with deep emotions and tremendous gratitude for those who've been my support, help, inspiration, and love throughout this journey.

First and foremost, I'm truly thankful to my supervisor, Dr. Shuo Wang, for his kind support and professional guidance throughout my doctoral studies. A memorable moment was when Dr. Wang spent his expertise and time thoroughly reviewing my first manuscript on the last day of the year, marking it extensively with red edits. His revision significantly improved the quality of my initial research on compound extreme events. His patience, care, and invaluable opportunities like teaching experience, proposal writing, and participating in academic conferences (including the AGU Annual Meeting) have greatly enriched my PhD experience. Without Dr. Wang's wise advice and profound knowledge, the successful completion of my PhD studies would remain an unfulfilled dream. I'm also thankful to my co-supervisor, Prof. Zhilin Li, for his kind support and great help during every significant phase of my doctoral studies.

The friendship and intellectual engagement from my colleagues at the Hydroclimate Research Lab is extraordinary. I extend my heartfelt thanks to Dr. Boen Zhang, Huijiao Chen, Yamin Qing, Mo Zhou, Yangyang Jing, Dr. Xiangfei Li, Sijie Tang, Qiang Yu, Jian Li, Fengjia Zhou, and Huiying Li. Our weekly meetings were not just a forum for academic discussion but a source of inspiration, fostering a collaborative and supportive research environment.

I'm also grateful to the research staff, administrative personnel, and classmates in the Department of Land Surveying and Geo-Informatics (LSGI). Their kind help and support have significantly contributed to my academic and personal growth.

Special thanks to my co-authors Dr. Colin Raymond, Dr. Tom Matthews, and Prof. Hamid Moradkhani for their collaboration, and gratitude to the anonymous reviewers for their insightful comments and suggestions that have greatly enhanced the quality of my publications. I would like to express my sincere appreciation to the members of my PhD examination committee, including

Dr. Yang Xu, Prof. Zhenzhong Zeng, and Dr. Xiaosheng Qin, for their invaluable time and constructive feedback.

To my beloved family—my mother, father, brother, sister, and fiancée—no words can express my gratitude for your endless love, unwavering support, and sacrifices. Your unconditional belief in me has been my greatest source of strength and motivation. Your love is the wind beneath my wings, propelling me forward, and for that, I am forever grateful.

As I reflect on this journey, the Latin saying "*Per aspera ad astra*" resonates deeply with me. Through the challenges, I strive for the stars. This journey, fueled by persistence, love, and support, has reached its conclusion, and I am grateful to each one of you who has been part of this journey. Your presence in my life is valued, and for that, I offer my deepest thanks and appreciation.

Sincerely,

Jiewen YOU

August 2024

Table of contents

List of Figures

List of tables

Chapter 1. Introduction

This chapter offers an overview of the research context, including a review of existing literature on compound hydrometeorological extremes. It also discusses the identification of research gaps and the significance of these gaps, outlines the aims and objectives of the research, and provides a summary of the overview of the dissertation.

1.1 Background

Hydrometeorological extremes, such as floods and heat waves, are primary drivers of global and regional natural disasters. These events trigger widespread economic losses, ecological damage, food scarcity, and significant mortality (UNDRR & CRED, 2020; WEF, 2020). Global warming further exacerbates these phenomena, increasing their severity and frequency. Among these, floods are one of the most common natural disasters globally, originating from heavy rainfall, runoff, and the rising sea level. These conditions can flood extensive areas, disrupting daily life and causing significant damage to infrastructure. Heat waves, by contrast, are characterized by extended periods of extreme heat, posing serious risks to human health, agriculture, and the availability of water resources. Recently, more special attention has been paid to compound hydrometeorological extreme events. These compound events are characterized by simultaneous or sequential events involving various climate drivers and hazards (Zscheischler et al., 2018, 2020; Raymond, Horton, et al., 2020; De Ruiter et al., 2020; Bevacqua et al., 2021), amplifying impact on human health, urban infrastructure, and other socio-economic aspects. The critical characteristics of these phenomena highlight the pressing need for enhanced detection, comprehensive understanding, and proactive risk assessment and resilience planning.

Coastal flooding is a notable coastal-specific hazard among hydrometeorological extremes. This type of flooding often results from storm surges during tropical cyclones, leading to significant damage in low-lying areas. A storm surge is a dangerous phenomenon that occurs when there is an abnormal rise in sea level caused primarily by low atmospheric pressure and strong winds from tropical and extra-tropical cyclones (Cid et al., 2017; Muis et al., 2016; Tadesse et al., 2020). This dangerous phenomenon could have devastating impacts on coastal communities (Bevacqua et al., 2019; Boumis et al., 2023; Wahl et al., 2015; Zhang & Wang, 2021). In China,

storm surge is considered the most severe marine hazard and has caused a direct economic loss of over 1,427 billion RMB in the past decade (Bulletin of China marine disaster, 2023; Ji et al., 2021; Wang et al., 2021a). Therefore, the spatiotemporal characteristics of storm surges serve as an important basis for disaster risk management in coastal areas (Martzikos et al., 2021).

Storm surge and other driving factors, such as rising sea levels and increased runoff from heavy rainfall, could coincide to cause flooding in a particular area. Such flood events triggered by the simultaneous occurrence of multiple sources of flooding are referred to as compound flooding (Bevacqua et al., 2019; Fang et al., 2021; Wahl et al., 2015). The interactions between different factors increase the complexity and severity of the flood event. As a result, compound flood events are often more severe and damaging than individual flooding factor acting alone. Recent compound flood events have resulted in damages and losses of human life in many countries around the world, such as Typhoon Lekima in 2019, Cyclone Amphan in 2020, Hurricane Ida in 2021, Hurricane Ian in 2022, and Typhoon Doksuri in 2023. Low-lying coastal cities are highly vulnerable to compound flooding due to their proximity to both sea and river systems (Gao et al., 2023; Moftakhari et al., 2017). During a tropical storm or hurricane, heavy rainfall may lead to inland flooding while strong winds cause storm surges along the coast. When these storm surges coincide with high tides or are exacerbated by rising sea levels, coastal areas may experience even greater inundation. Runoff from heavy rainfall can further contribute to flooding in depressed areas, and this combination can overwhelm the local drainage and flood defense systems, leading to more extensive and damaging floods (Lai et al., 2023; Toyoda et al., 2023). It is estimated that approximately 23% of the world's population resides within 100 kilometers of coastlines and at elevations under 100 meters above sea level (Small and Nicholls, 2003). The high density of population and infrastructure in coastal regions increases the vulnerability of these areas to compound flood events. Furthermore, compound flood risk is projected to increase with future sea level rise in a warming climate (Kulp and Strauss, 2019). In order to effectively respond to compound flooding in coastal areas, it is essential to assess and understand the associated risk (Feng et al., 2023; Matos et al., 2023), particularly through a spatially seamless and temporally continuous assessment of compound flood risk.

Another hydrometeorological extreme phenomenon that requires attention in the context of global climate change is extreme heat, including heat waves and humid heat. Heat waves are

characterized by prolonged periods of abnormally high temperatures. Humid heat, or heat stress, is caused by a combination of high temperatures and elevated humidity levels. This combination more accurately represents the physiological triggers of heatstroke and dehydration, and therefore is more likely to reflect dangerous conditions (Mora et al., 2017; Raymond et al., 2021). Heat-related extreme weather poses great challenges to public health, agriculture and the overall sustainability of ecosystems. And as temperatures are projected to rise, the frequency and severity of these events are expected to increase, necessitating adaptation strategies to mitigate their effects.

The study of compound hydrometeorological extremes can be further extended between compound heat and flood hazards. Due to the interaction and interdependence between temperature and precipitation, there may be a lagged connection between heat waves and heavy rainfall (Chen et al., 2021; Liu et al., 2019; Zhang & Villarini, 2020). This interaction can form a consecutive heat wave and heavy rainfall event, in which two extreme weather phenomena occur in back-to-back sequences. There is growing evidence that the sequential occurrence of heavy rainfall after the end of heat waves is likely to cause flash flooding, which can cause extensive damage to water quality, fundamental infrastructures, crop yields, and human livelihood. For instance, a heat wave was followed by heavy rainfall and flooding in 2019 in Australia, thereby leading to severe economic losses and environmental issues (Cowan et al., 2019; Zhang & Villarini, 2020). Similar abrupt alternations from preceding severe heat waves to thunderstorms and flash floods also occurred around the world, causing widespread socioeconomic losses (BBC News, 2020; Cappucci, 2019; ITV News, 2020). Therefore, exploring the probability of occurrence and evolution characteristics of compound heat wave and heavy rainfall events is crucial for revealing how these weather systems interact with each other and for improving the predictive skill of compound extremes under a warming climate. This is particularly important in China that is expected to experience more intense heat waves and heavy rainfall events throughout the 21st century (Deng et al., 2020; Sun et al., 2017; Wu et al., 2019).

In addition to heavy rainfall following heat waves, further consideration needs to be given to the emerging twinned hazards from both sides: successive heat-pluvial events and pluvial-heat events. These compound events could pose more considerable challenges to society. On the one hand, the combined impact of two extreme events can result in more extensive damage compared to when each event occurs separately (Kawase et al., 2020; Mukherjee & Mishra, 2021; De Ruiter

et al., 2020; Zscheischler et al., 2020). On the other hand, in such compound events, the lack of preparation and recovery time can further amplify adverse effects. For successive heat-pluvial events, a sequence of heat extremes followed by pluvial flooding occurred in the United States in September 2017 (Cappucci, 2019), in the United Kingdom in August 2020 (ITV Weather, 2020) and in South Korea in July 2020 (Min et al., 2022), leading in each case to severe infrastructure damages, livestock deaths, and flood-related morbidity/mortality. The considerable source of concern is that people are generally not well prepared for high-intensity rainfall during prolonged hot weather; when it does occur, it can be so rapid that people have little time to adjust and safely evacuate (De Ruiter et al., 2020; Matthews et al., 2019; Raymond, Horton, et al., 2020). As an example of a successive pluvial-heat event, Japan experienced heavy rainfall and subsequent extreme heat in July 2018, causing more than 300 fatalities and large economic losses (Kawase et al., 2020; Wang et al., 2019). The landfalls of tropical cyclones Irma and Ida in Florida and Louisiana, respectively, led to notable health impacts on residents who in the storms' aftermath were without air conditioning to combat the typical high heat stress values of late summer (Chatlani & Madden, 2021; Skarha et al., 2021). In such cases, the subsequent extreme heat adds to impacts in affected areas because the damage to infrastructure such as roads and power grids makes it more difficult to avoid heat exposure, and to obtain treatment in the case of heat illness (Issa et al., 2018). These recent examples highlight the importance of investigating the temporally compounding characteristics of heat-pluvial and pluvial-heat extremes more broadly.

1.2 Literature review on compound flood hazards

Storm surges, particularly during tropical cyclones, are a key factor in coastal flooding, often leading to the breaching of flood defenses by extreme water levels. Predicting these surges is crucial for accurate coastal flood analysis, as they significantly contribute to the risk and impact of such events. The in-situ tide gauge records provide critical observation-based storm surge information to support coastal flood risk assessments. However, these measurements often cover a relatively short time span, which is not suitable for trend detection and extreme value analysis (Tadesse & Wahl, 2021). To overcome this issue, two types of approaches have been proposed to estimate the storm surges based on spare data: physical and statistical methods. Physical methods refer to hydrodynamic models driven by process-based shallow-water equations and atmospheric forcing that induce surge and wave, are relatively accurate but computationally expensive

(Bloemendaal et al., 2019; Howard et al., 2010; Muis et al., 2020; Shimura et al., 2022). Physical models provide valuable insights into the processes, but they require significant computational resources and may be limited by the accuracy of underlying physics and assumptions (Fernández-Montblanc et al., 2019; Ramos-Valle et al., 2020). In contrast, statistical methods can be used to quantify the relationship between storm surges and explanatory variables, such as wind speed, atmospheric pressure, and sea surface temperature (Cid et al., 2018; Tadesse et al., 2020). This allows for the development of data-driven models that can simulate storm surges efficiently by making the best use of available data.

It is important to provide a temporally-continuous estimate of storm surges for better understanding of the long-term trend and variability of coastal flood events. Physical models used for storm surge simulation are often based on single events (Wang & Liu, 2021). This is because physical models require detailed information about storm surge characteristics, such as wind speed, atmospheric pressure, and precipitation, which are often difficult to obtain for historical events (Arns et al., 2020; Zijl et al., 2013). To overcome these limitations, machine learning approaches have been widely used to reconstruct long-term storm surge records, such as the data-driven model developed by Tadesse et al. (2020) for global storm surge reconstruction, with a focus on providing long-term and temporally seamless reconstructions of storm surges. However, these models do not provide a spatially and temporally continuous estimate of storm surges (Cid et al., 2018; Tadesse & Wahl, 2021), which is necessary to gain a better understanding of the spatiotemporal patterns of storm surges and to support disaster risk management and adaptation in coastal zones (Beck et al., 2020; Martzikos et al., 2021; Shimura et al., 2022). Therefore, there is an urgent need to develop new approaches which can provide continuous estimates of the spatiotemporal distribution of storm surges.

Spatial extrapolation of storm surges at ungauged stations along the coastline is also useful for decision-making in coastal flood risk management and adaptation, which can estimate the spatially-continuous distribution of storm surge heights with coverage for entire coastal areas (Calafat & Marcos, 2020). In previous studies, a variety of methods were proposed for probabilistic storm surge prediction that took into account uncertainties to estimate the storm surges at ungauged sites. For example, Beck et al. (2020) proposed a copula-based hierarchical Bayesian spatial model and then Calafat & Marcos (2020) performed a probabilistic analysis using the Bayesian

hierarchical model to estimate the spatially-continuous storm surges in Europe. While previous studies have conducted probabilistic prediction of storm surges, there is still a lack of spatially-temporally-continuous probabilistic prediction of storm surges for providing a comprehensive understanding of the spatiotemporal variability of storm surge events. This is particularly important in China due to its extensive coastline and high population density in coastal areas, making it vulnerable to coastal flooding caused by storm surges.

In addition to coastal flood hazards induced by storm surges, an increasing number of studies are now examining the simultaneous occurrence of coastal and pluvial flooding. Pluvial flooding, resulting from heavy rainfall, leads to water overflow on the ground surface when the intensity of the rain surpasses the drainage system's capacity. This type of flooding typically results in water accumulation in urban regions, particularly in low-lying coastal areas with inadequate drainage systems. Pluvial flooding, when combined with coastal flooding, can lead to a phenomenon known as compound flooding in coastal regions (Sun et al., 2024; Xu et al., 2023). This is a significant issue as it can cause more severe damage than either type of flooding alone. Growing studies have been conducted to understand the dynamics and impacts of compound flooding. For instance, a study by Wahl et al. (2015) highlighted the increased risk of compound flooding in low-lying coastal cities due to climate change. Similarly, a study by Bevacqua et al. (2019) in emphasized the need for considering compound flooding in flood risk assessments, as ignoring the interaction between pluvial and coastal flooding can significantly underestimate the flood risk.

Compound flooding occurs when heavy rainfall (pluvial flooding) coincides with high sea levels (coastal flooding), leading to a complex and amplified flood risk. In this area, the synergy of various factors, with storm surges as a notable component, is pivotal in fully understanding the full spectrum of coastal flood risks. Ground-level observations using tidal gauge stations are essential in this process, as they provide highly accurate and direct measurements of local conditions. These tidal gauge stations are particularly beneficial for monitoring storm surges and sea-level rise (Cid et al., 2018; Tadesse & Wahl, 2021). In contrast, higher resolution and better spatial-temporal continuity products are increasingly utilized to identify precipitation characteristics, enhancing understanding of rainfall patterns over a larger area (Beck et al., 2019; Sun et al., 2018). However, this reliance on tidal gauge stations for storm surges and sea level rise

introduces a significant limitation: a predominantly point-based approach in previous studies (Tadesse et al., 2020; Wahl et al., 2015). This method restricts the comprehensive understanding of the broader spatial and temporal dynamics of compound flood risk along the whole coastline. One key limitation is the lack of information at ungauged sites (Beck et al., 2020; Calafat and Marcos, 2020), which may lead to gaps in data and potentially overlook critical areas of risk. In the context of a warming climate and an accelerating water cycle, it becomes imperative to integrate spatially seamless and temporally continuous data for storm surges, sea level, and precipitation into compound flood risk assessments in coastal areas. This integrated approach is necessary to effectively manage the complex nature of compound flooding under a warming climate.

Compound flood risk assessment can be broadly categorized into numerical and statistical modeling methods (Sun et al., 2024; Xu et al., 2023). Numerical models such as Delft3D (Deltares, 2013), SCHISM (Zhang et al., 2016) and ADCIRC (Luettich et al., 1992) are useful for evaluating flood risk at ungauged sites by simulating water body movements and generating detailed data on flood levels and extents (Santiago-Collazo et al., 2019). These models account for various flood types (fluvial, pluvial, and coastal flooding) and employ different coupling techniques to simulate interactions between flood sources (Gallien et al., 2018; Zhang and Najafi, 2020). However, their limitations include high computational demands and the necessity for extensive, detailed input data, which are challenging to acquire at ungauged sites. Conversely, statistical models provide a viable alternative when physical modeling is impractical due to data or computational constraints. They analyze relationships and interactions among flood drivers (Jane et al., 2020; Zheng et al., 2014), using data to estimate compound flood likelihood and severity at gauged sites (Lai et al., 2023). Common methods in statistical modeling include the threshold excess method, conditional method, correlation coefficient method, copula function, etc. (Coles et al., 1999). Despite their utility, the effectiveness of these models is hindered at ungauged sites due to data scarcity, which may lead to inaccurate compound flood risk assessment.

1.3 Literature review on compound heat and flood hazards

Having reviewed the literature on compound flood hazards in the previous section, I now extend our literature review on compound heat and flood hazards, a critical area where both

thermal and aqueous extremes intersect and interact. Heat waves and heavy rainfall are regarded as two of the most frequent and widespread severe hydrometeorological hazards. Heat waves are characterized by a period of abnormally high temperatures lasting three or more days, and heavy rainfall is a primary cause of flooding. Different from concurrent heat waves and droughts, heat waves and heavy rainfall are usually considered as isolated events, given that the two contrasting weather extremes seldom co-occur in the same place (Mukherjee & Mishra, 2021; Ridder et al., 2020). There are a number of studies have been conducted to investigate heat waves and heavy rainfall events that occur in isolation (Day et al., 2018; Donat et al., 2016; Perkins-Kirkpatrick & Lewis, 2020). Nonetheless, there may be a lagged connection between heat waves and heavy rainfall in consideration of the interaction and mutual dependence between temperature and precipitation (Chen et al., 2021; Liu et al., 2019; Zhang & Villarini, 2020), but little effort has been made to examine the compound occurrence of heat waves and heavy rainfall events as well as physical mechanisms and characteristics.

There are a number of generally accepted hypotheses and evidence that show the potential of the compound occurrence of heat waves and heavy rainfall. For instance, it is projected that precipitation intensity will increase as the climate warms, which is primarily described by the Clausius-Clapeyron (C-C) relation, indicating that the atmospheric moisture-holding capacity will increase approximately 7% as per degree temperature rise (Trenberth et al., 2003). Despite the C-C rate scaling is not applicable to all regions around the world and lower or super C-C rates are observed elsewhere (Held & Soden, 2006; Lenderink et al., 2017; Lepore et al., 2015; Utsumi et al., 2011), the rising temperatures should increase the atmospheric water-holding capacity to some extent, which may result in more condensed moisture favorable for the occurrence of heavy rainfall (Molnar et al., 2015; Wang et al., 2017). Heat waves are often characterized by prolonged high temperature and high humidity in the lower atmosphere. The heat forcing combined with moist accumulation may contribute to atmospheric instability and trigger convection for precipitable water at the local scale (Berg et al., 2013; Fowler et al., 2021; Randall et al., 1992). As a result, water vapor convergence may be enhanced, leading to the occurrence of sudden heavy rain after the end of a heat wave. These hydrological processes and atmospheric dynamics could potentially lead to a consecutive heat wave and heavy rainfall (CHWHR) event. At a relatively large scale, there may be a lagged connection between heat waves and heavy rainfall as a result of the thermodynamic effects, circulation shift and land-sea-atmospheric feedbacks (Chen et al., 2020a;

Deng et al., 2020; Fischer et al., 2007; Giorgi et al., 2011; Randall et al., 1992; Shang et al., 2020). The termination of a heat wave could be associated with a shift from a large-scale atmospheric blocking to circulation anomalies as well as monsoon oscillation, accompanied with thunderstorms, tropical cyclones or atmospheric rivers (Boschat et al., 2015; Raghavendra et al., 2019), potentially leading to the sudden occurrence of heavy rainfall after the end of a heat wave.

Recent studies have increasingly focused on extreme humid heat and pluvial flooding, which have devastating impacts on humans, ecosystems, and society (You et al., 2023; Mora et al., 2017; Raymond, Matthews, et al., 2020; Tellman et al., 2021). Previous studies have typically considered one hazard (humid heat or pluvial flooding) and its impacts at a time. In recent years, a number of studies have investigated the spatiotemporal compounding of multiple extremes, defined as "compound events" (Bevacqua et al., 2021; Raymond, Horton, et al., 2020; Zscheischler et al., 2018, 2020). Compared to the well-established compound events that occur simultaneously such as concurrent droughts and heat waves (Mukherjee & Mishra, 2021; Ridder et al., 2020), temporally compounding events that occur in close succession have yet to be well-understood, especially in the case of consecutive hot and wet extremes where the transition may be associated with convection and therefore difficult to forecast. This difficulty bears on the challenge of quantifying the causal link between extreme heat and nearby pluvial flooding, which seldom occur at precisely the same location and involve a range of atmosphere-ocean-land interactions at various scales.

A rapid transition from hot to wet conditions may occur because of large-scale processes related to the water cycle, atmospheric dynamics, and their feedbacks; in the subtropics and mid-latitudes, for example, this can include the movement of features such as areas of enhanced monsoon convection or the jet stream meandering (Shang et al., 2020; Shimpo et al., 2019; Swain et al., 2016; Wang et al., 2019). There may also be direct linkages: high temperatures are a key factor contributing to atmospheric instability, potentially leading to or enhancing localized precipitation events that terminate previous heat events through strong evaporational cooling (Berg et al., 2013; Fowler et al., 2021; Wang et al., 2017). The other side of the coin is the occurrence of pluvials followed by heat events, which may be associated with tropical cyclone-released diabatic heating effects or region-scale thermal advection (Chen et al., 2021; Emanuel, 2003; Hart et al., 2007; Parker et al., 2013; Sukhovey & Camara, 1995). Another important physical mechanism is

that the elevated moisture fluxing into the atmosphere during a pluvial event can increase atmospheric latent heat content, which may result in higher near-surface wet-bulb temperatures favourable for the occurrence of humid heat (Liu et al., 2017, 2019; Matthews et al., 2022; Speizer et al., 2022).

Compared to well-understood underlying dependent drivers (e.g., concurrent drought and heat waves), quantifying the relationship between temporally compounding hot and wet extremes remains challenging. Recent work has, however, made progress. For example, analysis in the central United States found that a high percentage of floods are preceded by a heat stress event (Zhang & Villarini, 2020). Elsewhere, assessments of consecutive heat wave and heavy rainfall events in China found an increased probability of hotter and shorter heat waves followed by heavy rainfall compared to heat waves not followed by heavy rainfall (You & Wang, 2021). Consecutive heat and pluvial events have also been investigated in previous studies, again focused on China (Chen et al., 2021; Liao et al., 2021). Globally, an increasing percentage of floods are likely to be accompanied by hot extremes, using observed dry bulb temperature for the identification of heat extremes and hydrological models for the simulation of flood hazards (Gu et al., 2022). Compared to dry heat, however, humid heat measures (that include the effects of both temperature and humidity) better capture the physiological drivers of heat stress and therefore are more likely to reflect dangerous conditions (Mora et al., 2017; Raymond et al., 2021). More importantly, the use of coarse-resolution general circulation models (GCMs) (~100–300 km) and conceptual hydrological models may lead to considerable uncertainty in projecting spatially resolved flood risks caused by heavy precipitation (Duethmann et al., 2020; Grimaldi et al., 2019; Zhang et al., 2021). Consequently, there is a need for thorough assessments of the spatiotemporal detections of temporally compounding heat and pluvial events, as well as attribution of the underlying factors.

1.4 Research gap and significance

Despite considerable efforts that have been made to identify and attribute compound hydrometeorological extremes, most previous studies are still subject to some key limitations. These research gaps hinder a comprehensive understanding of compound hydrometeorological extreme events.

(1) Lack of in-situ tide gauge stations and records. In-situ tide gauge stations provide records of sea water levels, which is one of the important bases for understanding compound flood risks. However, there are practical constraints on the number and distribution of these stations, leading to sparse spatial coverage. In addition, the data collected from different stations may cover different time periods, resulting in discontinuities in the data over time. Therefore, innovative research methods are needed to address the continuous spatiotemporal distribution of storm surges and sea level rise, which could contribute to a better understanding of the spatiotemporal dynamics of compound flooding and enhance coastal disaster risk management capabilities.

(2) Lack of associated research on compound heatwaves and heavy rainfall events. Despite the well-understood mechanisms of heat waves and heavy rainfall, current knowledge on the abrupt transitions from deadly heat waves to devastating downpours remains unclear as they are usually treated as isolated events in previous studies. Furthermore, physical mechanisms and characteristics associated with the occurrence of compound heatwaves and heavy rainfall events remain unclear, hampering our understanding of spatiotemporal patterns and evolutionary processes of this type of compound hazards. In addition, little is known about the projected future changes of compound heatwaves and heavy rainfall events and associated compound risks in a warming climate.

(3) Limited understanding of emerging compound events globally. Knowledge about emerging compound events, such as those involving humid heat and pluvial flooding, remains inadequately understood globally. This shortfall is exacerbated by the reliance on robust detection and reliable attribution methodologies, which are crucial for validating results concerning complex compound events under conditions of autocorrelation and multiple testing. This gap in both knowledge and methodology poses a significant challenge, constraining our capacity to accurately forecast and mitigate the impacts of such events on a global scale. Additionally, the lack of in-depth insights into the physical mechanisms and attributes of these compound events further hampers our capacity to understand their spatiotemporal behaviors and evolutionary trends effectively.

Addressing these gaps is vital for advancing our comprehension and response to compound hydrometeorological extremes, highlighting the urgent need for targeted research in these areas.

1.5 Research aims and objectives

The overarching aim of the dissertation is to provide incremental knowledge and understanding of the challenges on compound hydrometeorological extremes, with a specific focus on compound flood hazards and compound heat-flood hazards. To achieve this aim, the dissertation is divided by several specific objectives, outlined as follows:

(1) Developing a data-driven probabilistic framework for storm surge prediction. This dissertation aims to construct a probabilistic model using vine copula and ensemble machine learning, coupled with the Bayesian Hierarchical Model (BHM) approach. The objective is to provide a robust framework for accurately estimating continuous storm surge extremes. This model framework will offer decision-makers continuous probabilistic forecasts, aiding in effective mitigation and strategic planning for infrastructure in a changing climate.

(2) Providing a comprehensive assessment of compound flood risk. By integrating ensemble machine learning with copula statistical methods, this dissertation seeks to conduct a thorough spatial-temporal analysis of compound flood risk. This approach is designed to inform urban planning and the development of climate change mitigation strategies, highlighting the need to address multi-hazard flood risks in coastal urban areas.

(3) Investigating a new type of temporally compounding events, referred to as CHWHR. The dissertation will investigate CHWHR events, focusing on their occurrence, driving mechanisms, and future projections. It aims to provide a systematic assessment of CHWHR events in the context of a changing climate and analyze the lagged interplay between heat waves and heavy rainfall. This research will deepen our understanding of CHWHR as a new type of compound extreme and offer crucial insights for implementing effective adaptation and mitigation measures.

(4) Global analysis of temporally humid heat and pluvial flood events. This objective involves a global analysis of the frequency changes in temporally compounding humid heat and pluvial flood events, and the factors influencing these events. Reliable statistical tests are proposed to ensure the validity of the results for complex compound events. The goal is to acquire a comprehensive understanding of these compound events, detect occurrences, analyze the decomposition of warming or moistening effects, and identify key influencing factors.

1.6 Dissertation overview

As shown in Figure 1.1, this dissertation is structured to address the intricacies and challenges associated with compound hydrometeorological hazards in a warming climate, with a particular focus on two critical aspects: (1) compound flood hazards, and (2) compound heat and flood hazards. This dissertation is organized as follows. Chapter 2 lays the foundation by offering a detailed description of the data acquisition and the research methods used for performing spatiotemporal continuous prediction and characterizing different compound extremes. Chapter 3 presents a probabilistic, data-driven framework for the spatiotemporal prediction of continuous storm surge extremes and subsequently focused compound flood risk assessment in Hong Kong. The flood risk assessment is conducted at a local scale in Hong Kong due to its detailed tide gauge data and it is highly susceptible to the combination of rising sea levels, dense urban layout, and intense rainfall, making it an ideal case study for compound coastal flood risk assessment. Chapter 4 presents the detection, attribution and projection of consecutive heat wave and heavy rainfall events across China. This study is assessed on a regional scale in China due to the availability of detailed, long-term observation-based gridded precipitation and temperature datasets for historical detection, CORDEX fine-resolution data under different warming scenarios for future projections, and the country's diverse climate zones. In Chapter 5, the scope widens to a global scale, presenting in-depth analyses of successive heat-pluvial and pluvial-heat events. These compound events are analyzed at a global scale because I find some media coverage of these occurrences outside China, but the global picture remains largely unknown. This global perspective allows for the identification of broader patterns and trends, providing a comprehensive understanding of these phenomena. Concluding the dissertation, Chapter 6 synthesizes the findings and suggests future directions in compound hydrometeorological studies.

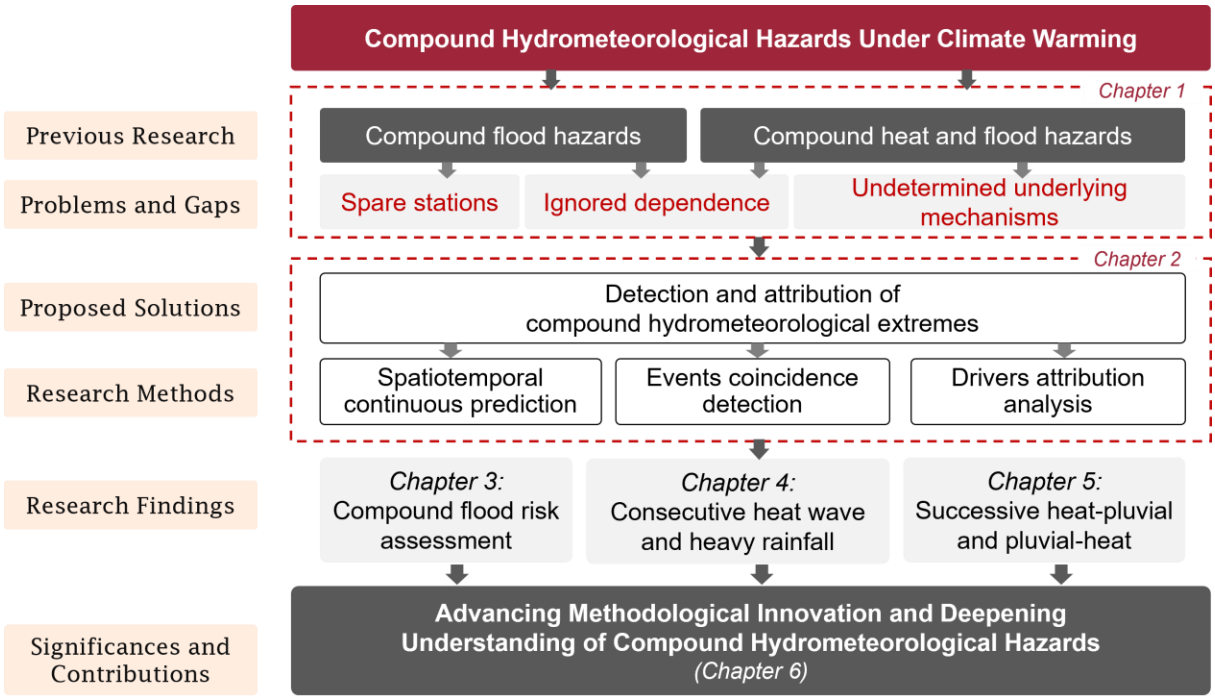

Figure 1.1 The framework of the dissertation.

Chapter 2. Data and methodology

This chapter presents both the data description and the research methodology used for analyzing compound hydrometeorological extremes, along with the associated proposed techniques for identifying and evaluating their compounding features. Firstly, this chapter provides a description of the innovative ensemble machine learning and Bayesian Hierarchical Model (BHM) framework I have developed, essential for the spatiotemporal prediction of continuous storm surge extremes and comprehensive analysis of compound flooding. Definitions and methods for identifying heat waves and heavy rainfall events are outlined, aiding in understanding their lagged dependencies. Furthermore, this chapter defines and characterizes humid heat, pluvial flooding, and their compound events. Finally, the chapter presents the moving-blocks bootstrap resampling-based significance test that I have proposed, designed specifically for the detection of compound events. It also describes the innovative application of field significance tests that I have introduced in the realm of compound event attribution.

2.1 Data descriptions

In this dissertation, I have employed a diverse range of datasets, broadly categorized into three groups: observational data, reanalysis products, and model simulations.

For observational data, this includes daily gridded information on temperature and precipitation, along with tidal gauge station data. The temperature and precipitation data, which is gridded daily at a spatial resolution of $0.5^{\circ} \times 0.5^{\circ}$, was sourced from the China Meteorological Data Service Center. This data is an interpolation from 2,472 station observations covering the period from January 1, 1961, to the present (Zhao et al., 2014). Regarding tidal gauge station data, hourly sea level data from 16 tide gauges along the coast of China was derived from the Global Extreme Sea Level Analysis (GESLA) tide gauge dataset (Haigh et al., 2021). For the Hong Kong region data was downloaded from six open-access tidal gauge stations operated by the Hong Kong Observatory (Hong Kong Observatory, https://www.hko.gov.hk/en/cis/climat.htm). These stations provide daily mean sea level measurements and four distinct tidal phases.

The reanalysis products include the 5^{th} generation ECMWF (The European Centre for Medium Range Weather Forecasts) global reanalysis (ERA5) (Hersbach et al., 2020)

(https://cds.climate.copernicus.eu/cdsapp#!/dataset/reanalysis-era5-single-levels) and reanalysis data from the National Centers for Environmental Prediction (NCEP, https://psl.noaa.gov/data/gridded/data.ncep.reanalysis.html). The choice to use these reanalysis datasets is due to their inclusion of four essential variables (daily mean temperature, precipitation, specific humidity, and air pressure at 2m from the surface) with global coverage at the daily timescale, which allows for a comprehensive and uniform analysis across different regions and time periods. Large-scale atmospheric variables from ERA5, like convective available potential energy (CAPE), convective inhibition (CIN), and vertically integrated moisture divergence (VIMD), were used to explore the physical processes behind compound events. Additionally, daily atmospheric variables like sea-level pressure (SLP), sea-surface temperature (SST), precipitation (Prep), and wind speeds at 10 meters (WindU and WindV), were also sourced from the ERA5 Reanalysis dataset. I also employed the precipitation dataset from MSWEP (Multi-Source Weighted-Ensemble Precipitation, Version 3), which can be downloaded at https://www.gloh2o.org/mswep/. The MSWEP dataset is acclaimed for its accuracy and wide-ranging applicability, providing precipitation data at a finely detailed spatial resolution of 0.1° (Beck et al., 2019).

Finally, the model simulations involved high-resolution CORDEX-CORE regional climate models to project future changes in the likelihood of compound events in China (https://esgf-data.dkrz.de/search/cordex-dkrz). An ensemble of three model runs, including MOHC-HadGEM2-ES, MPI-M-MPI-ESM-LR and NCC-NorESM1-M from CORDEX-CORE were selected under the Representative Concentration Pathway (RCP) 8.5 that represented a high-emission scenario.

2.2 Modeling framework for spatiotemporal prediction of continuous storm surge extremes

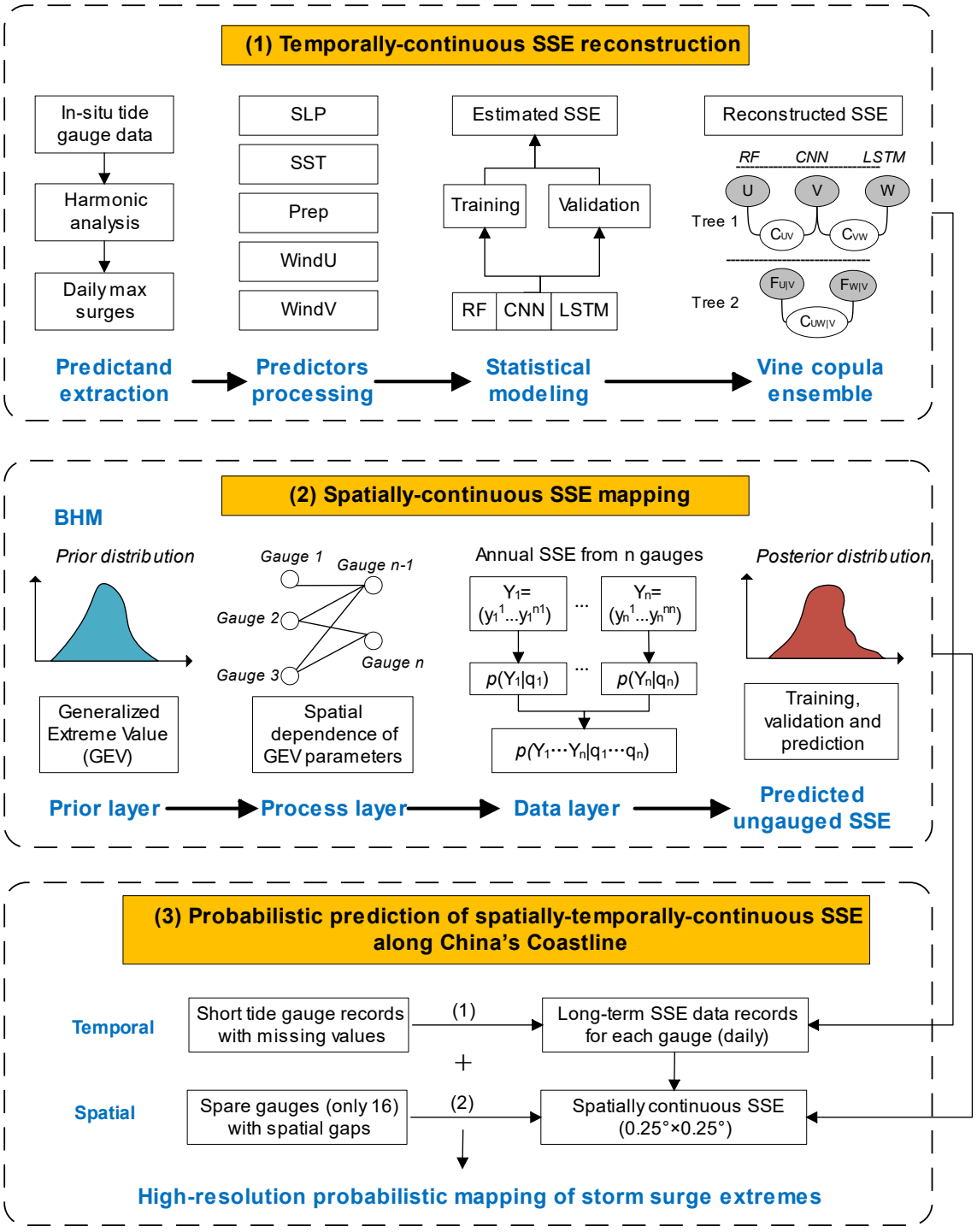

Figure 2.1 The proposed modeling framework designed to improve the estimation of storm surge extremes (SSE) along China's coastline.

2.2.1 Temporally-continuous storm surge extremes reconstruction

As shown in Figure 2.1, I first extracted and processed the predictand and predictors to achieve temporally-continuous storm surge extremes (SSE) reconstruction, and then conducted model training and validation using three individual models including Random Forest (RF), Convolutional Neural Network (CNN), and Long Short-Term Memory (LSTM). Lastly, I used vine copula to combine the outputs of the three different models.

For predictand processing, I used the daily maximum surge extracted from sea level data. This was achieved through a classical harmonic analysis, which involved the following four steps. First, the hourly sea level time series from tide gauges were detrended by removing the annual mean sea level. Second, the astronomical tide was obtained through harmonic analysis with 67 tidal constituents on a year-by-year basis using the T_Tide package (Pawlowicz et al., 2002). Third, non-tidal residuals were obtained by subtracting the astronomical tide from the detrended sea level time series, and the non-tidal residuals were considered as storm surges in this study. Lastly, the daily maximum surge was calculated from the hourly time series of non-tidal residuals.

For predictors processing, I used five key predictors, namely SLP, SST, WindU, WindV, and Prep, and the five predictors were used to model the SSE. These atmospheric variables were chosen based on their relevance and influence on storm surge, which were commonly used for modeling the SSE (Cid et al., 2018; Tadesse et al., 2020). I first determined the optimal area surrounding the tide gauges where predictor information was used to train and validate the statistical models. A geographic grid centered on each tide gauge location is selected, termed a 'box'. This 'box' comprises a 3 × 3 grid, where each cell represents a specific area dimension ($0.25^{o}\times0.25^{o}$), encompassing the tide gauge at the center. This configuration allows for the effective incorporation of data that reflects the immediate meteorological conditions influencing storm surges while balancing computational efficiency. To include the delay effect of predictors on the daily maximum surge, I used the time-lagging predictors as far back as 24 hours. After that, I standardized the predictor matrix to account for the different units used by each predictor. To reduce the dimensionality of the model, Principal Component Analysis was applied to the predictor and only the principal components that explain 95% of the variance were retained (Hotelling, 1933).

For statistical modeling, I employed three state-of-the-art machine learning methods, namely RF, CNN and LSTM, to train and validate the pre-processed predictor matrix, which captured the complex non-linear relationship between predictors (atmospheric variables) and the predictand (daily maximum surge). RF is a widely used data-driven method and has shown a promising performance in accurately modeling the SSE. CNN is a type of deep learning neural network and can be used to learn complex spatiotemporal patterns from the input data (e.g., SSE, SLP, SST, etc.) and their variations over time. LSTM, on the other hand, is a type of recurrent neural network (RNN) architecture that can make predictions on sequential data. In the context of storm surge modeling, LSTM is more useful as it can capture temporal dependencies and long-term patterns in atmospheric variables that affect surge levels. For model validation, I utilized the 10-fold cross-validation technique to train and validate the model by dividing the dataset into 10 equally-sized subsets, and each subset was used once for validation while the remaining 9 subsets were used for training. The model performance was assessed using Pearson's correlation (corr) and Root Mean Squared Error (RMSE):

$$corr = \frac{\sum_{i=1}^{n} (x_i - \bar{x})(y_i - \bar{y})}{\sqrt{\sum_{i=1}^{n} (x_i - \bar{x})^2}\sqrt{\sum_{i=1}^{n} (y_i - \bar{y})^2}} \quad 2\text{-}1$$

$$RMSE = \sqrt{\frac{\sum_{i=1}^{n} (y_i - x_i)^2}{n}} \quad 2\text{-}2$$

where x_i and y_i denote the observed and predicted SSE, respectively. Similarly, $\bar{x}$ and $\bar{y}$ represent the mean values of the observed and predicted SSE, respectively.

To overcome the limitations of individual models and address the uncertainty of storm surge prediction, I developed a vine copula ensemble approach that combined the outputs of three different models (RF, CNN, LSTM). The approach involves four steps: (1) selecting the optimal marginal distribution for each model output from a set of 13 probability distributions using the Kolmogorov–Smirnov (K–S) test and maximum likelihood estimation; (2) using vine copula to link the marginal distributions of different model outputs together to construct the conditional quantile functions of the ensembled SSE; (3) fitting vine copula by considering seven types of bivariate copulas as pair-copula family candidates, including elliptical copulas (Gaussian and Student t), Archimedean copulas (Clayton, Gumbel, Frank, and Joe), and the two-parameters

hybrid Archimedean copula BB1, to construct the vine copula; (4) fitting vine copula with two different structures. For C-vine copulas, an example of the conditional distribution of the SSE is expressed as follows:

$$
\begin{aligned}
F(y \mid x_{RF}, x_{CNN}, x_{LSTM}) &= \frac{\partial C_{y,LSTM \mid RF,CNN}\left(F(y \mid x_{RF}, x_{CNN}), F(x_{LSTM} \mid x_{RF}, x_{CNN})\right)}{\partial F(x_{LSTM} \mid x_{RF}, x_{CNN})} \\
&= \frac{\partial C_{y,LSTM \mid RF,CNN}\left(\frac{\partial C_{y,CNN \mid RF}\left(F(y \mid x_{RF}), F(x_{CNN} \mid x_{RF})\right)}{\partial F(x_{CNN} \mid x_{RF})}, \frac{\partial C_{LSTM,CNN \mid RF}\left(F(x_{LSTM} \mid x_{RF}), F(x_{CNN} \mid x_{RF})\right)}{\partial F(x_{CNN} \mid x_{RF})}\right)}{\partial\left(\frac{\partial C_{\mathrm{LSTM,CNN} \mid \mathrm{RF}}\left(F(x_{LSTM} \mid x_{RF}), F(x_{CNN} \mid x_{RF})\right)}{\partial F(x_{CNN} \mid x_{RF})}\right)} \\
&= h\begin{Bmatrix} h[h(u_y, u_{RF}, \theta_{RF\ y}), h(u_{CNN}, u_{RF}, \theta_{RF\ CNN}), \theta_{CNN\ y \mid RF}], \\ h[h(u_{LSTM}, u_{RF}, \theta_{RF\ LSTM}), h(u_{CNN}, u_{RF}, \theta_{RF\ CNN}), \theta_{CNN\ LSTM \mid RF}], \theta_{LSTM\ y \mid RF\ CNN} \end{Bmatrix}
\end{aligned}
\tag{2-3}
$$

For D-vine copulas

$$
\begin{aligned}
F(y \mid x_{RF}, x_{CNN}, x_{LSTM}) &= \frac{\partial C_{y,RF \mid CNN,LSTM}\left(F(y \mid x_{CNN}, x_{LSTM}), F(x_{RF} \mid x_{CNN}, x_{LSTM})\right)}{\partial F(x_{RF} \mid x_{CNN}, x_{LSTM})} \\
&= \frac{\partial C_{y,RF \mid CNN,LSTM}\left(\frac{\partial C_{y,CNN \mid LSTM}\left(F(y \mid x_{LSTM}), F(x_{CNN} \mid x_{LSTM})\right)}{\partial F(x_{CNN} \mid x_{LSTM})}, \frac{\partial C_{RF,LSTM \mid CNN}\left(F(x_{RF} \mid x_{CNN}), F(x_{LSTM} \mid x_{CNN})\right)}{\partial F(x_{LSTM} \mid x_{CNN})}\right)}{\partial\left(\frac{\partial C_{RF,LSTM \mid CNN}\left(F(x_{RF} \mid x_{CNN}), F(x_{LSTM} \mid x_{CNN})\right)}{\partial F(x_{LSTM} \mid x_{CNN})}\right)} \\
&= h\begin{Bmatrix} h[h(u_y, u_{LSTM}, \theta_{LSTM\ y}), h(u_{CNN}, u_{LSTM}, \theta_{CNN\ LSTM}), \theta_{CNN y \mid LSTM}], \\ h[h(u_{RF}, u_{CNN}, \theta_{RF\ CNN}), h(u_{LSTM}, u_{CNN}, \theta_{CNN\ LSTM}), \theta_{RF\ LSTM \mid CNN}], \theta_{RF\ y \mid CNN\ LSTM} \end{Bmatrix}
\end{aligned}
\tag{2-4}
$$

where the ensembled SSE is denoted by y. The RF-, CNN- and LSTM-predicted SSE is denoted by x_{RF}, x_{CNN}, and x_{LSTM}, respectively. θ_y, θ_{RF}, θ_{CNN} and θ_{LSTM} represent the corresponding marginal cumulative probability. For more details on vine copula, please see Alipour et al., 2022 and Zhang et al., 2022.

2.2.2 Spatially-continuous storm surge extremes mapping

I used a Bayesian hierarchical model (BHM) for probabilistic modeling of annual maximum storm surge extremes (SSE) at the 16 tide gauges along China's coastline and predicting SSE at ungauged locations. The BHM consists of a prior layer, a process layer, and a data layer.

In the prior layer, I specify the prior distribution for the annual maximum surge at each location. Based on previous studies, I assume that the annual maximum surge follows a generalized extreme value (GEV) distribution. The GEV distribution is a three-parameter distribution that can model extreme values of a random variable, and it is a suitable prior distribution for modeling extreme storm surges. For a random variable *x*, the GEV probability density function is defined as:

$$F(x) = \begin{cases} \left(1 + \xi\left(\frac{x-\mu}{\sigma}\right)\right)^{-1/\xi} & \text{if } \xi \neq 0 \\ e^{-(x-\mu)/\sigma} & \text{if } \xi = 0 \end{cases} \quad \text{2-5}$$

where μ is the location parameter, representing the location of the distribution on the x-axis. σ is the scale parameter, representing the spread or variability of the distribution. ξ is the shape parameter, which governs the tail behavior of the distribution. I assume that the location parameter of the GEV distribution varies in both time and space, and the scale and shape parameters vary only in space over the entire study domain, following the previous study (Calafat & Marcos, 2020).

In the process layer, I modeled the spatial and temporal processes that underlie the observed data, sharing information between locations. I assume that the observed data follows a max-stable process, which means that the maximum of a set of random variables is also a random variable that follows a GEV distribution (Calafat & Marcos, 2020; Reich & Shaby, 2012). I modeled the max-stable process using a spatial process that captures residual dependence among the annual maxima, indicating that multiple locations may be affected by the same event. The spatial process introduces random effects in the location and scale parameters of the GEV distribution, which allows us to make predictions of the annual maxima at ungauged locations.

In the data layer, I specified the likelihood function for the observed data. I assume that the annual maximum surge at each location and year follows a GEV distribution with location and scale parameters that are influenced by the spatial process. The likelihood function allows us to estimate the parameters of the GEV distribution and the spatial process based on the observed data.

Following previous studies, the likelihood function for the observed data is expressed as:

$$Y_t(\mathrm{s}_i) \mid \theta_t(\mathrm{s}_i), \mu_t(\mathrm{s}_i), \sigma(\mathrm{s}_i), \xi, \alpha \overset{\text{ind}}{\sim} \text{GEV}\left(\mu_t^*(\mathrm{s}_i), \sigma_t^*(\mathrm{s}_i), \alpha\xi\right) \quad \text{2-6}$$

where $Y_t(\mathbf{s}_i)$ represents the annual maximum surge for year t and at location s. θ represents the spatial process that captures residual dependence among the annual maxima surges. In the GEV distribution, μ is the time-varying location parameter, σ is the spatially-varying scale parameter and ξ is the shape parameter. And α is a parameter that controls the relative contribution of small-scale errors. The parameter α ranges from 0 to 1, with smaller values having more weights on the large-scale patterns captured by the spatial process and larger values allowing for more small-scale variabilities in the residuals.

The location parameter was assumed to vary smoothly with time and is modeled as a spatiotemporal integrated random walk. The initial states of the location parameter and its trend were modeled using Gaussian processes with specified covariance functions. The logarithm of the scale parameter is modeled as a spatial process using a Gaussian process with a specified covariance function. The scale parameter is restricted to be positive values.

Model parameters were estimated by maximizing their joint posterior distribution given the observed data. This was done by Bayesian inference through Markov Chain Monte Carlo (MCMC) sampling. Specifically, I run the Hamiltonian Monte Carlo (HMC) algorithm with four MCMC chains of 2,000 iterations each, with a warm-up period of 1,000 iterations. Once the posterior distributions of model parameters were obtained, I used them to predict the surge at ungauged locations and to create a spatially-continuous map of storm surges for the entire study region. This was done by simulating from the posterior predictive distribution, which considered the uncertainty in model parameters.

2.2.3 Probabilistic prediction of spatially-temporally-continuous storm surge extremes

To achieve probabilistic prediction of spatially-temporally-continuous storm surge extremes (SSE), I integrated the methods introduced above (Figure 2.1). First, I used the temporally-continuous SSE reconstruction approach to convert the short-term tide gauge records that contained missing values into the long-term SSE data records on a daily basis for each gauge. This approach enables the temporally-continuous estimates of the SSE at any given time. Next, I

employed the spatially-continuous SSE mapping methods to interpolate the temporally-continuous but spatially-sparse gauges (which comprise only 16 tide gauges) into spatially-continuous SSE at ungauged locations, with a spatial resolution of 0.25°×0.25°. By combining these two approaches, I can produce reliable and accurate probabilistic predictions of spatially-temporally-continuous SSE along China's coastline.

2.3 Compound flooding identification and analysis

2.3.1 Harmonic analysis

Harmonic analysis, a mathematical discipline within the domain of signal processing and time series analysis, is employed in this study to decompose sea level data into its constituent waves (Pawlowicz et al., 2002). Harmonic analysis represents functions or signals as combinations of basic waves, extending and applying principles from Fourier series and transforms. Specifically, in the context of extracting storm surge values, this method was utilized to identify the periodic components present in the sea level data and to extract daily maximum storm surges (Figure 2.2).

Initially, the sea level time series obtained from tide gauges underwent a detrending process. This was achieved using the following equation for detrending:

$$X_t^{'} = X_t - \bar{X}_{annual}$$

where $X_t^{'}$ represents the detrended sea level at time t, X_t is the original sea level at time t, and $\bar{X}_{annual}$ is the calculated annual mean sea level. This equation ensures that any long-term increase or decrease in sea level, potentially due to climatic changes or other non-periodic factors, is not considered in the analysis of short-term events like storm surges. Following the detrending, the astronomical tide was extracted using harmonic analysis techniques. This involves fitting a model to the data, comprising sinusoidal components characterized by specific frequencies, amplitudes, and phases. Typically, frequencies were selected to align with known tidal constituents. In this study, 67 such constituents were considered. The harmonic model formula is expressed as:

$$S(t) = \sum A_n \cos(2\pi f_n t + \varphi_n) \quad 2\text{-}7$$

where $S(t)$ represents the sea level at time t, A_n stands for the amplitude of the nth harmonic (n is 67 in this study), f_n denotes the frequency of the nth harmonic, φ_n represents the phase of the nth harmonic and the sum is taken over all harmonics.

Once the harmonic model is established, it facilitates the prediction of sea levels at any given time. The daily maximum storm surge value was then derived by subtracting the predicted tide, as determined by the harmonic model, from the observed sea level. This computation yielded the non-tidal residual, which serves as an indicator of daily maximum storm surge heights.

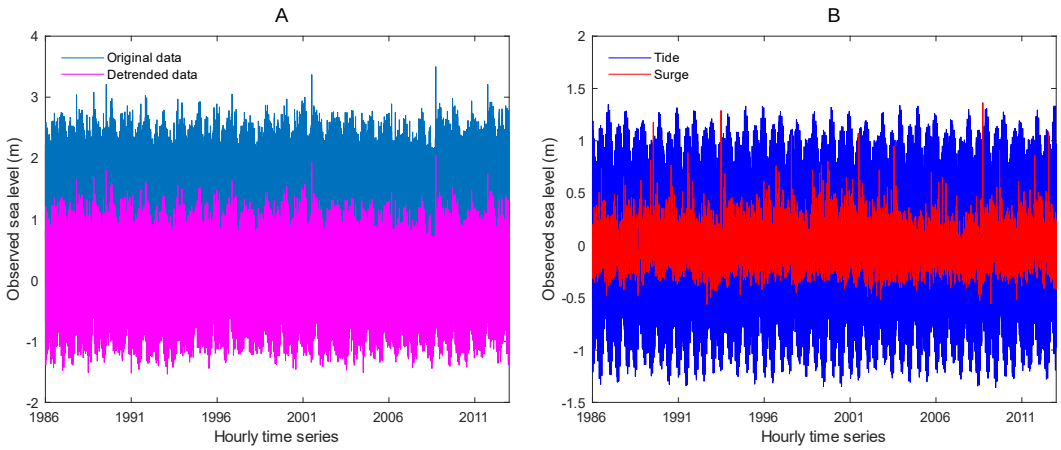

Figure 2.2 Illustration of extracting daily maximum storm surges from tidal gauge data using a harmonic analysis. 'Original data' refers to the observed sea level, while 'Detrended data' indicates the original data minus the annual trend. 'Tide' denotes the astronomical tide, and 'Surge' signifies the storm surge, each extracted using harmonic analysis techniques.

2.3.2 Identification and characterization of compound flooding

The simultaneous occurrence of multiple coastal flood drivers, such as extreme storm surge, sea level rise, and heavy rainfall, is uncommon but can result in catastrophic impacts. This study focuses on analyzing compound flood events caused by the concurrent occurrence of these factors. The methodology involves the Peaks Over Threshold approach to identify each type of extreme event. Extreme storm surge events are characterized as days where the maximum storm surges exceed the 95th percentile of historical data. Similarly, sea level rise events were identified as days where the daily mean sea level surpasses its 95th percentile during the 1979–2022 period. For heavy rainfall, I define events as days where rainfall exceeds the 95th percentile of precipitation on wet

days, calculated based on daily rainfall time series on days with rainfall of at least 1 mm. Compound flooding is thus defined by the concurrent manifestation of extreme storm surges, sea level rise, and heavy rainfall within a single day.

2.3.3 Mann-Kendall test

The Mann-Kendall test, a non-parametric approach, was used for analyzing trends among extreme storm surges, sea level rise, and heavy rainfall (Kendall, 1975; Mann, 1945). This method is advantageous for datasets that may not follow a normal distribution and is robust against the influence of outliers. The Mann-Kendall test assesses the relative magnitudes of data points, rather than their actual values, making it well-suited for datasets exhibiting non-linear trends or influenced by external, non-controlled factors. The test involves calculating the Kendall tau statistic, a measure of correlation, defined as:

$$\tau = \frac{2}{n(n-1)} \sum_{i=1}^{n-1} \sum_{j=i+1}^{n} sgn\left(x_j - x_i\right) \qquad 2\text{-}8$$

where n is the number of data points, x_i and x_j are data values in time series, and sgn is the sign function. A positive τ value indicates an increasing trend, while a negative value implies a decreasing trend. I determined the significance of observed trends at a 95% confidence level, enabling us to evaluate the likelihood of these trends occurring by chance. This method conforms to established practices in trend analysis, providing a reliable foundation for interpreting temporal changes.

2.3.4 Copula functions and return periods calculations

The copulas were used to model and analyze the dependencies between multiple variables among extreme storm surges, sea level rise, and heavy rainfall. Copulas are mathematical tools that link the individual distributions of single-dimensional variables to form a composite multivariate distribution. Copulas allow the combination of diverse marginal cumulative distribution functions (CDFs) to create multivariate CDFs, offering versatile modeling capabilities. This is formally expressed by Sklar's Theorem (Sklar, 1959), which states that for any multivariate CDFs $F(x_1, x_2, \ldots, x_n)$ with margins $F_1, \ldots, F_n$, there exists a copula C such that:

$$F(x_1, x_2, \dots, x_n) = C\big(F_1(x_1), F_2(x_2), \dots, F_n(x_n)\big) \quad \text{2-9}$$

where F represents the joint CDF of the multivariate distribution, $F_1, F_2, \dots, F_n$ are the marginal CDFs of the individual variables, and C is the copula function that binds these margins together. The corresponding multivariate density is:

$$f(x_1, \dots, x_n) = f_1(x_1) \cdot \dots \cdot f_n(x_n) \cdot c(u_1, \dots, u_n) \quad \text{2-10}$$

A generic bivariate copula function can be expressed as:

$$C_\theta(u, v) = \Phi_\theta(\Phi^{-1}(u), \Phi^{-1}(v)) \quad \text{2-11}$$

where $C_\theta(u, v)$ represents the copula function for two variables u and v, which are the cumulative probabilities under their respective marginal distributions. Φ and Φ^{-1} denote the CDF and inverse CDF of a standard distribution, respectively. θ is the parameter that models the dependency structure between u and v. This formulation demonstrates how a parametric copula can be utilized to model the joint distribution of two variables, accounting for their dependency structure.

For the construction of copula models, an array of several widely used probability distributions was utilized to approximate the theoretical CDF for extreme storm surges, sea level rise, and heavy rainfall. These distributions include exponential, gamma, generalized extreme value, generalized Pareto, logistic, log-logistic, lognormal, normal, three-parameter log-logistic, Gumbel, and Weibull. The optimal CDF was selected based on the minimum values obtained from the Akaike information criterion (AIC), defined as:

$$\text{AIC} = 2k - 2l \quad \text{2-12}$$

where k represents the count of parameters in the probability distributions, and l denotes the maximum log-likelihood value for the optimal parameter set, as determined by the maximum likelihood estimation. Several commonly used copula families, including Clayton, Frank, Gaussian, Joe, Student-t, Gumbel, and BB1, were considered potential candidates for constructing the copula models. The optimal copula model was determined based on the criterion of the lowest

AIC with the Kolmogorov–Smirnov (K–S) statistic. The equations of joint CDFs of these copula models are shown in Table 2-1 (Nelsen et al., 2006).

Table 2-1 The frequently utilized copula models.

Copula	Joint cumulative distribution function (CDF) in copula models
Clayton	$C(u,v) = (u^{-\theta} + v^{-\theta} - 1{,}0)^{-1/\theta}$
Frank	$C(u,v) = -\frac{1}{\theta} ln\left[1 + \frac{(exp(-\theta u) - 1)(exp(-\theta v) - 1)}{exp(-\theta) - 1}\right]$
Gaussian	$C(u,v) = \int_{-\infty}^{\phi^{-1}(u)} \int_{-\infty}^{\phi^{-1}(v)} \frac{1}{2\pi\sqrt{1-\theta^2}} exp\left(\frac{2\theta xy - x^2 - y^2}{2(1-\theta^2)}\right) dsdw$
Joe	$C(u,v) = 1 - \left[(1-u)^{\theta} + (1-v)^{\theta} - (1-u)^{\theta}(1-v)^{\theta}\right]^{1/\theta}$
Student-t	$C(u,v) = \int_{-\infty}^{t_{\theta_2}^{-1}(u)} \int_{-\infty}^{t_{\theta_2}^{-1}(v)} \frac{\Gamma((\theta_2+2)/2)}{\Gamma(\theta_2/2)\pi\theta_2\sqrt{1-\theta_1^2}} \left(1 + \frac{x^2 - 2\theta_1 xy + y^2}{\theta_2}\right)^{(\theta_2+2)/2} dsdw$
Gumbel	$C(u,v) = exp\left\{-\left[(-ln(u))^{\theta} + (-ln(v))^{\theta}\right]^{1/\theta}\right\}$
BB1	$C(u,v) = \left\{1 + \left[(u^{-\theta_1} - 1)^{\theta_2} + (v^{-\theta_1} - 1)^{\theta_2}\right]^{1/\theta_2}\right\}^{-1/\theta_1}$

Utilizing the best-fitting marginal distributions, I computed return levels for the return period of '2 years', '5 years', '10 years', '20 years', '50 years', and '100 years', under two distinct scenarios: univariate and trivariate analysis. The univariate analysis pertains to situations where

only a single flood driver exceeds its 95th percentile. In contrast, the trivariate analysis focuses on compound flood scenarios when storm surges, sea level rise, and heavy rainfall concurrently surpass their 95th percentiles. The return period concept is fundamentally the inverse of the exceedance probability, which is derived by calculating the area above the target value in the probability density function. By examining these return periods, I gain insights into the likelihood and intensity of flood events driven by various flood drivers. The formula for the return period calculation can be represented as:

$$T = \frac{1}{1 - Pr(X < x)} = \frac{1}{1 - F_X(x)} \quad \text{2-13}$$

where Pr stands for 'Probability' and $Pr(X < x)$ refers to the probability that the variable X will take a value less than a specific threshold x. F_X is the cumulative distribution function of the random variable evaluated at x.

2.4 Detection and attribution of heat wave, heavy rainfall and CHWHR events

2.4.1 Identification and characterization of extremes events

In Chapter 4, a heat wave event is defined when its daily maximum temperature exceeds the 90th percentile of daily maximum temperature (CTX90pct) for at least three consecutive days during the extended summer season (May–September). This percentile is determined for each location and each calendar day with a moving window, which is based on ranking historical 15-day samples surrounding the calendar day (7-day before and after) during the 30-year baseline period (1961–1990). Thus, a total of 450 samples were used to calculate the 90th percentile value. The percentile-based threshold has been proved reasonable and commonly used in previous studies (Perkins & Alexander, 2013; Perkins-Kirkpatrick & Lewis, 2020; Sun et al., 2017).

A heavy rainfall event is detected when daily rainfall is higher than the 95th percentile of precipitation in wet days. This percentile is calculated for each location based on the days with rainfall amount larger than 1 mm/day in the 1961–1990 period. The definition used to identify heavy rainfall events is recommended by the Expert Team on Climate Change Detection and Indices (ETCCDI, http://etccdi.pacificclimate.org/) at the World Meteorological Organization,

which is widely recognized and consistent with previous studies (Casanueva et al., 2016; Zhai et al., 2005).

The consecutive heat waves and heavy rainfall (CHWHR) events refer to the phenomenon of heat waves being followed by heavy rainfall within a prescribed temporal interval. It should be noted that I only consider the sequential occurrence of heavy rainfall after the end of a heat wave as a CHWHR event and did not consider the occurrence of heavy rainfall during heat waves. Considering the time lag that may exist between heat wave and heavy rainfall events, I selected potential impact-related intervals of 1 day, 3 days and 7 days that represented a relatively short time span for identifying the CHWHR events. Heat wave and heavy rainfall events are identified separately when the corresponding index exceeds the predefined thresholds. A heat wave event is defined when its daily maximum temperature exceeds the 90th percentile of daily maximum temperature for at least three consecutive days during the extended summer season (May–September). This percentile is calculated for each location and each calendar day, using a 15-day moving window surrounding the calendar day during the 30-year baseline period (1961–1990). And a heavy rainfall event is detected when daily rainfall is higher than the 95th percentile of precipitation in wet days. The percentile-based thresholds used to identify heat waves and heavy rainfall events have been proved reasonable and consistent with previous studies (Casanueva et al., 2016; Perkins & Alexander, 2013; Perkins-Kirkpatrick & Lewis, 2020; Sun et al., 2017; Zhai et al., 2005).

The CHWHR events are characterized by two indices: (1) heat wave duration (HWD), which is defined as the length of longest heat wave events; and (2) heat wave magnitude (HWM), which is calculated based on the average temperature anomaly relative to the calendar day 90th percentile during heat wave events, following the work of Perkins-Kirkpatrick & Lewis (2020).

$$HWM_{gd} = \frac{\sum_{1}^{N_{gd}} \left(T_{max,gd} - T_{thre,gd}\right)}{N_{gd}} \qquad 2\text{-}14$$

where HWM_{gd} represents heat wave intensity (℃) at the grid gd; $T_{max,gd}$ is the daily maximum temperature; $T_{thre,gd}$ is the daily varying 90th percentile value (thresholds); N_{gd} is the number of heat wave days.

2.4.2 Event coincidence analysis

The probability of occurrence of CHWHR events and the associated significance test (at the significance level of 0.05) as well as sensitivity assessment has been conducted using the event coincidence analysis (ECA) framework which are widely adopted to quantify simultaneous or lagged coincidences between event time series (Donges et al., 2016; Siegmund et al., 2017; He & Sheffield, 2020). ECA identifies the statistically significant relationship of CHWHR events based on the Poisson process, with an assumption that the lagged occurrence between heat wave and heavy rainfall is randomly distributed (Donges et al., 2016; Siegmund et al., 2017). The probability of occurrence of CHWHR events can be calculated as follows:

$$P_g = 100 \times \frac{1}{N_{HW,gd}} \sum_{j=1}^{N_{HW,gd}} \Theta \times \left(\sum_{i=0}^{N_{HR,gd}} 1_{[0,\Delta T]}((t_i^{HW,gd} - 1), (t_i^{HR,gd})) \right) \quad 2\text{-}15$$

where P_g represents the probability of occurrence of CHWHR events (%), which represents the fraction of heat waves followed by heavy rainfall within the following days; N_{HW} is the total number of heat wave events at the grid gd; Θ is the Heaviside function, providing values between 0 (no heat wave events followed by heavy rainfall) and 1 (all heat wave events followed by heavy rainfall). $1_{[0,\Delta T]}$ is the indicator function of the interval $[0, \Delta T]$, representing the event timing (time windows). For ΔT=0, the inner term becomes the term "$\delta((t_i^{HW,gd} - 1), (t_i^{HR,gd}))$". δ represents the Kronecker delta, which will collapse to a value of 1 if both arguments are equal and zero otherwise. $t_i^{HW,gd}$ and $t_i^{HR,gd}$ are heat wave and heavy rainfall event series, respectively, with a value of 1 (0) corresponding to time sequences with (without) an event.

To carry out sensitivity analysis, different time lags (ΔT) have been applied to calculate the number of lagged coincidences between heat waves and heavy rainfall within a prescribed temporal interval. In addition to the occurrence of heat waves followed by heavy rainfall within 1-day, different settings of time windows (ΔT=3 and 7) were also taken into account to address the potential time lags between heat waves and heavy rainfall events within the following 3 and 7 days.

2.5 Detection and attribution of heat, pluvial and successive heat and pluvial events

2.5.1 Definitions of extreme events

In Chapter 5, I utilized measures of humid heat, which represent the combined effects of high temperatures and high humidity to indicate heat stress. In the following context, I will simply refer to this concept as 'heat'. Specifically, I adopted the wet-bulb temperature (TW) index as a proxy for humid heat events. As shown in Figure 2.3, daily TW is calculated using the well-accepted formula with the inputs of near-surface temperature, specific humidity and surface pressure (Buzan et al., 2015; Davies-Jones, 2008; Raymond, Matthews, et al., 2020). A heat event is defined when its daily TW exceeds the 90th percentile of daily TW for at least three consecutive days during the boreal summer season (May–September). This percentile is determined for each location and each calendar day with a moving window, which is based on ranking historical 15-day samples surrounding the calendar day (7-day before and after) during the entire research period (You & Wang, 2021).

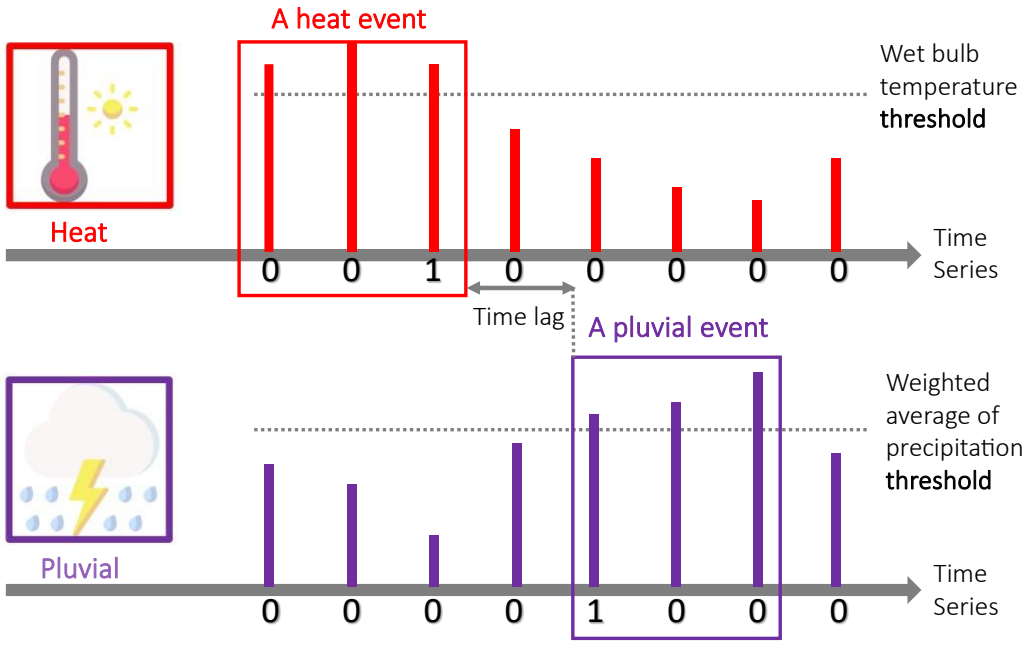

Figure 2.3 A schematic of identifying heat and pluvial event time series.

For the detection of the pluvial event, as shown in Figure 2.3, the weighted average of precipitation (WAP) index is adopted to identify pluvial events due to the lack of global

observation for pluvial flooding (Lu, 2009). The index considers both the immediate contribution of today's precipitation and the gradual attenuation contribution from the earlier days, through the weighted average of precipitation with the weight decreasing with the number of the days. WAP has been proved reasonable and commonly used in previous studies (Chen et al., 2021; Liao et al., 2021). In this analysis, similar to the identification of heat events, a pluvial event is detected when daily WAP exceeds the threshold (the 90th percentile of the WAP during the reference period) for at least three consecutive days.

The weighted average of precipitation (WAP) is defined as:

$$WAP = \sum_{n=0}^{N} w_n P_n \quad \text{2-16}$$

$$w_n = (1 - a)a^n \quad \text{2-17}$$

where N is the number of the day prior to the present day; P is daily precipitation; w_n is the weight of the days; a is the contribution parameter (between 0 and 1). Following the previous studies, I defined a=0.9, and using alternative choices does not affect the main results of the study (Lu, 2009; Chen et al., 2021; Liao et al., 2021).

Successive heat and pluvial events are characterized by frequency, defined as the average number of annual successive events and the total number of successive events during the study period. Successive heat-pluvial and pluvial-heat events are heat events followed by pluvial events within a 7-day interval, and likewise for pluvial-heat events (Figure 2.3). A 7-day temporal interval (time lag between heat and pluvial events) is adopted in the main section for analysis considering the trade-off between sample numbers and related social impacts, which can represent a relatively short time span for disasters recovery and preparedness. Furthermore, to test the sensitivity of different choices of prescribed settings, I also considered the other potential impact-related temporal intervals and plausible definitions of successive events by employing more extreme percentiles and thresholds. To handle the occurrence of multiple heat events and pluvial events within a week, two successive heat or pluvial events should be clustered into a single event if they are separated by two days or less.

2.5.2 Moving-blocks bootstrap-resampling-based significance test

As the sequential occurrence of heat and pluvial events at a given location can be relatively rare and largely a matter of chance, traditional methods that estimate compound-event frequency based on event coincidence may struggle to identify causal relationships leading to successive extremes (Chen et al., 2021). To address this issue, I used a bootstrap resampling-based significance test to investigate the dependence of two time series, which can test whether the observations are significantly different from what would be expected due to chance alone. In practice, to consider autocorrelation when randomly sampling time series, the moving-blocks bootstrapping is utilized to perform the significance test (Vogel & Shallcross, 1996; Wilks, 1997) using a block size of three days. A sensitivity test using alternative block sizes (such as 5 or 10) did not change the significance of my findings. I implemented the moving-blocks bootstrap-resampling-based significance test for each grid cell in the following steps: (1) Identify the heat and pluvial event series from 1956 to 2015. The event series are constructed by assigning a label of '1' (indicating occurrence) to the end day of each event in one series and to the start day of each event in another series; (2) Generate 1,000 resampled event series using the moving-blocks bootstrap, where each resampled series has the same length as the original series. By randomly permuting the event series, rather than the original daily time series, all relevant statistical attributes can be preserved; (3) Compute the occurrence frequencies of heat-pluvial and pluvial-heat events for each pair of resampled series using a pre-determined method; (4) Compute the empirical distribution of consecutive occurrence frequencies using the 1,000 resampled series; (5) Compute the 95% confidence intervals of the empirical distribution of consecutive occurrence frequencies. (6) Compute the occurrence frequency of heat-pluvial and pluvial-heat events for the original series based on ERA5 and NCEP datasets. (7) Determine whether the occurrence frequency of heat-pluvial and pluvial-heat events for the original series falls within the 95% confidence interval of the empirical distribution of consecutive occurrence frequencies; (8) If the occurrence frequency of heat-pluvial and pluvial-heat events for the original series is outside the 95% confidence interval, then it is statistically significant at the 0.05 level.

2.5.3 Decomposition of warming/moistening effects

To investigate the specific impacts of warming and moistening on the changes observed in temporally compounding heat and pluvial events between the recent (1989–2023) and past (1956–1989) 34-year periods, I conducted a decomposition analysis. The goal is to assess the relative significance of warming and moistening effects in shaping the trends of consecutive heat and pluvial events. The methodology involves constructing four distinct time series realizations: (1) with warming and moistening (based on original observational data); (2) without warming and moistening (by removing trends of wet-bulb temperature and weighted average of precipitation); (3) warming alone (by removing the trend of weighted average of precipitation) and (4) moistening alone (by removing the trend of wet-bulb temperature).

2.5.4 Investigation of VPD anomalies and field significance test

I investigated the potential impact of atmospheric humidity, measured by vapor pressure deficit (VPD) (Massmann et al., 2019; Yuan et al., 2019), on the abrupt alternation between heat and pluvial events. High VPD values are indicative of dry conditions and can exacerbate heat events, while low VPD values are associated with high humidity and may signal a transition from a heat event to a pluvial event. Therefore, VPD anomalies may serve as a key link between heat and pluvial events, making it a relevant diagnostic for my study. For successive pluvial-heat events, I analyzed the differences in VPD anomalies between heat events followed by pluvial events (i.e., heat-pluvial) and those not followed by pluvial events (i.e., heat-without-pluvial), specifically focusing on VPD conditions one day after the end of heat events. Similarly, for pluvial-heat events, I examined the differences in 1-day VPD anomalies between pluvial events followed by heat events (i.e., pluvial-heat) and those not followed by heat events (i.e., pluvial-without-heat).

To determine whether the observed differences in VPD are statistically significant and not solely due to chance, I conducted field significance tests to address the issue of multiple hypotheses (Wilks, 2006, 2016). Three different types of field significance test to resolve the multiple testing issue are considered in the study, including the Walker's test, false discovery rate (FDR) and moving block bootstrapping-based multivariate test.

(1) Walker's test

In the analysis, the global null hypothesis (H_0) refers to there is no statistically significant differences in VPD exist between heat-pluvial and heat-without-pluvial events. According to the Walker's criterion which adopts a higher standard for statistical significance, only individual local tests (i.e., grid points) with p-values no larger than α_{Walker} should be regarded as significant.

$$\alpha_{\text{Walker}} = 1 - (1 - \alpha_0)^{1/K} \quad \text{2-18}$$

where α_{Walker} is p-value by Walker's criterion, α_0 is the local significance level which is defined as 0.05 in the study. K is the total number of individual local tests (i.e., grid points).

(2) False discovery rate (FDR)

I also used a relatively recent approach—control of the false discovery rate (FDR) to carry out the field significance test. FDR represents the expected proportion of rejected local null hypotheses that are actually true. Specifically, the false discovery rate (FDR) was controlled during these tests to minimize the likelihood of identifying false positive results (type I errors) when multiple tests are performed simultaneously. The FDR represents the proportion of rejected null hypotheses that are true. By controlling the FDR, I can increase confidence in the significance of the findings (Benjamini & Hochberg, 1995; Ventura et al., 2004; Wilks, 2006).

Practically, the analysis involves testing the global null hypothesis (H_0), which assumes no statistically significant differences in VPD between heat-pluvial and heat-without-pluvial events. To address the multi-hypothesis issue, I performed field significance tests by controlling FDR rates at a certain level q. This involves rejecting local null hypotheses whose p-values are no greater than a threshold p_{FDR}.

$$p_{\text{FDR}} = \max_{j=1,\ldots,\text{K}} [p_{(j)} : p_{(j)} \leq \alpha_0 \left(\frac{j}{N}\right)] \quad \text{2-19}$$

where N is the total number of local tests (i.e., grid points) and α_0 is the desired level of significance (0.05). To determine the largest K satisfying the equation, the p-values be arranged in ascending order; any local tests with p-values smaller than or equal to the largest p-value are deemed to be field-significant (Wilks, 2006).

(3) Moving block bootstrapping-based multivariate test

To address the autocorrelation effects in the data, I also have conducted field significance test using the procedure of moving blocks bootstrap resampling. For a two-tailed test, for the upper tail, global hypothesis H_0 should be rejected if

$$\frac{\sum_{i=1}^{n_B} I(d_i^* \geq d)}{n_B + 1} \leq \frac{\alpha_0}{2} \qquad 2\text{-}20$$

For the lower tail, H_0 can be rejected if

$$\frac{\sum_{i=1}^{n_B} I(d_i^* \leq d)}{n_B + 1} \leq \frac{\alpha_0}{2} \qquad 2\text{-}21$$

where $I(\cdot)$is the indicator function, which takes a value of 1 if the statement inside the parentheses is true, and 0 otherwise. n_B is bootstrap realizations of d*. α_0 is the desired level of significance (0.05).

Chapter 3. Compound flood risk assessment

In this chapter, storm surges and compound flood events in coastal areas are discussed, with the aim of presenting extensive spatial-temporal maps and a comprehensive compound flood risk assessment. The first is to improve compound flood risk assessment by overcoming the limitations of spare tide gauge stations. In this section, a new method for predicting storm surges is proposed. By employing vine conjugate ensemble machine learning and Bayesian hierarchical modelling, probabilistic prediction of spatially-temporally-continuous storm surges along China's coastline is achieved. An extended framework is then introduced, incorporating storm surge sea level rise, and heavy rainfall for compound flood risk assessment in coastal areas of Hong Kong. These findings can assist urban planning and the development of adaptation strategies to enhance the protection of coastal infrastructure against compound flood hazards.

3.1 Spatiotemporal prediction of continuous storm surge extremes along China's coastline

Coastal flooding induced by storm surges poses a serious threat to coastal communities, causing significant damage to buildings and endangering lives. Due to limited data from tide gauge stations, however, there is a lack of understanding of the severity and behavior of these storm surges over time and space. To address this knowledge gap, I develop a novel framework to achieve a spatially and temporally continuous estimation of storm surges in China.

3.1.1 Temporally-continuous storm surge extremes reconstruction

3.1.1.1 Validation of daily maxima prediction

I first validate the daily maxima of storm surge predicted by four data-driven models, including Random Forest (RF), Convolutional Neural Network (CNN), Long Short-Term Memory (LSTM), and vine copula ensemble, using a 10-fold cross-validation approach. The performance of these models was evaluated using Pearson's correlation and RMSE values between predicted and observed values across 16 gauges in China from 1979 to 2020. It is important to note that I initially conducted 1000 simulations of vine copula, but for comparison purposes, I focus solely on the mean predicted values as a representation of the overall performance of the vine copula ensemble model. The 10-fold validation results, as shown in Figure 3.1, demonstrate that the vine

copula ensemble model slightly outperforms the other models in predicting storm surge extremes (SSE). Specifically, the vine copula ensemble model has the highest mean Pearson's correlation value (0.62), followed by the LSTM (0.61) and RF (0.60) models, while the CNN model has the lowest mean correlation value (0.59). Similarly, the vine copula ensemble model has the lowest mean RMSE value (11.42 cm), followed by the LSTM (11.55 cm) and RF (11.68 cm) models, while the CNN model has the highest mean RMSE value (11.94 cm). The vine copula model, despite only marginal improvements in mean Pearson's correlation and RMSE, compensates by offering superior probabilistic estimation. This is evident in its exceptional performance in high reliability and sharpness metrics, as shown in Figure 3.3. The advantages of the vine copula method, including flexibility, capturing variability and quantifying uncertainty, underscore its value as a tool for storm surge predictions, surpassing the limitations associated with relying on a single model.

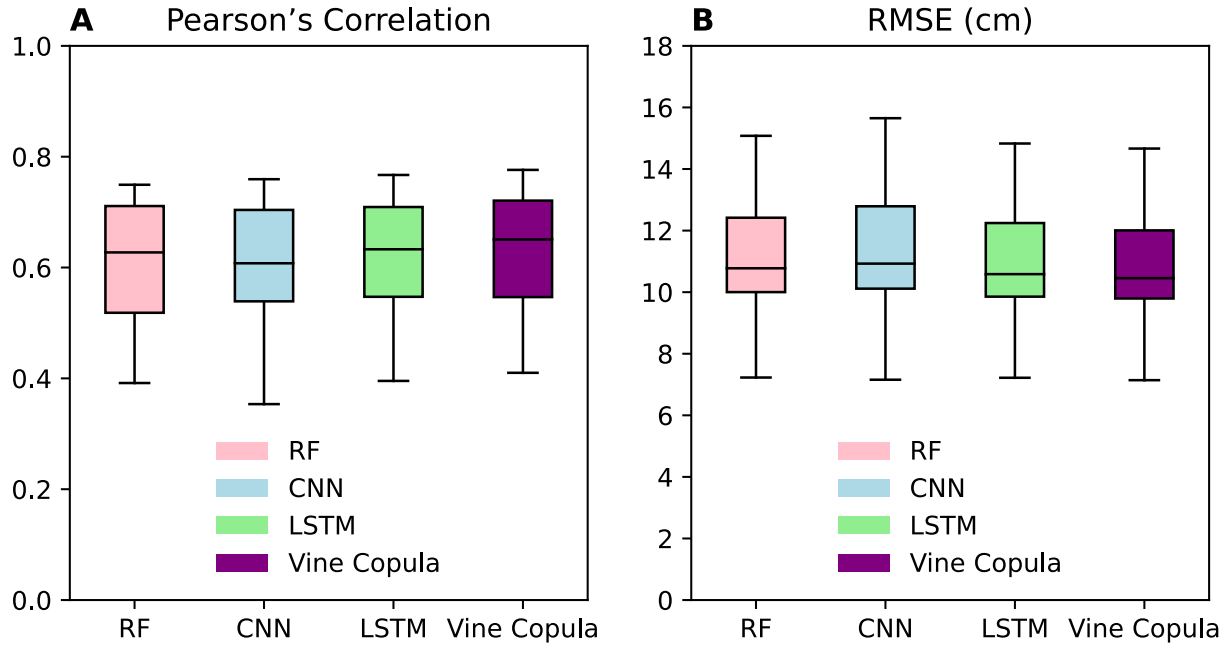

Figure 3.1 Validation of four data-driven models used to predict daily maximum storm surges across 16 gauges in China from 1979 to 2020, based on a 10-fold cross-validation approach. The data-driven models include Random Forest (RF), Convolutional Neural Network (CNN), Long

Short-Term Memory (LSTM), and vine copula ensemble. A: Pearson's correlation. B: root mean squared error (RMSE).

Figure 3.2 presents the varying performance of the vine copula ensemble model in predicting daily maxima of storm surges across tide gauge stations. In general, the vine copula ensemble model performs better in the northern part of the study area, with higher mean correlations and lower RMSE values compared to the southern part. The highest performance is observed for Xiamen, with a mean Pearson's correlation coefficient of 0.78 and an RMSE of 11.99 cm. The correlations for tide gauge stations range from 0.41 (Dongfang) to 0.78 (Xiamen), indicating that the vine copula ensemble model generally performs well in predicting daily maxima of storm surges. Higher correlations are observed at the stations of Xiamen (0.78), Shanwei (0.73), Macau (0.72), and Hong Kong (0.71). On the other hand, the RMSE values derived for tide gauge stations range from 7.14 cm (Kaohsiung) to 21.79 cm (Lusi), reflecting varying levels of predictive accuracy. Stations with the lowest RMSE values, including Kaohsiung (7.14 cm), Keelung (7.41 cm), and Haikou (9.72 cm), indicate that the vine copula ensemble model is able to provide more accurate predictions for these locations.

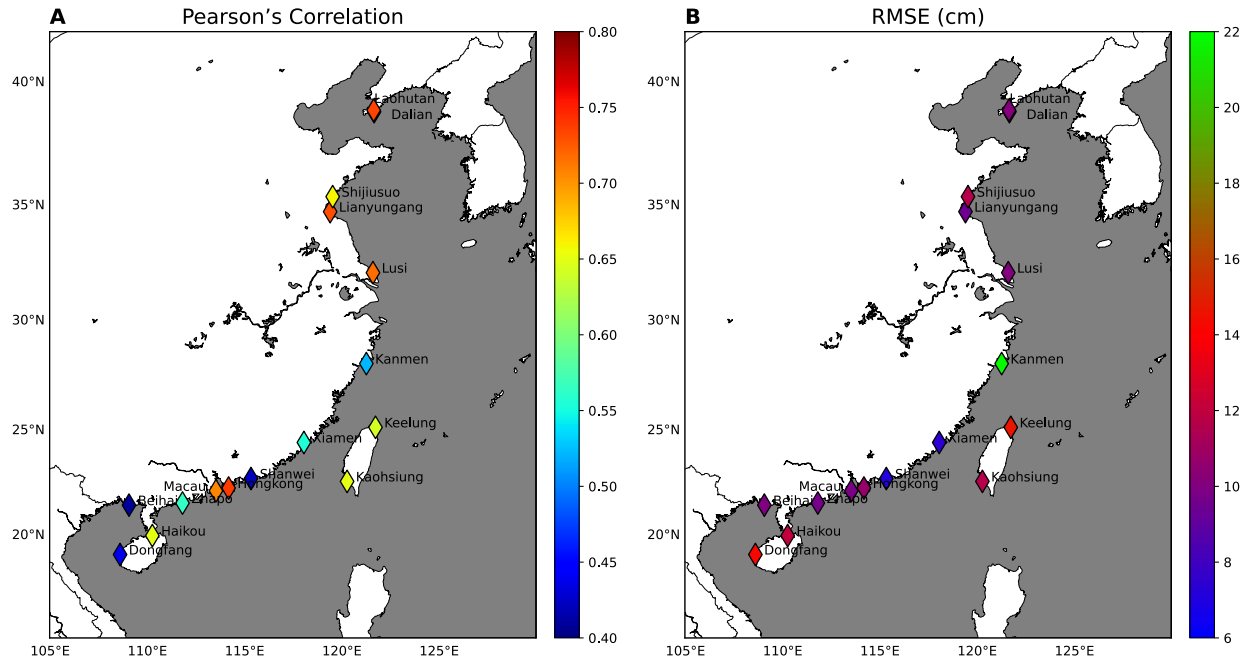

Figure 3.2 Validation of the vine copula ensemble model used to predict daily maximum storm surge across 16 gauges in China, based on a 10-fold cross-validation approach. A: Pearson's correlation. B: root mean squared error (RMSE).

To further assess the performance of the vine copula ensemble model in predicting daily maximum storm surges, I compare observed and predicted time series for 16 tide gauge stations along China's coastline. I choose the tide gauge in Hong Kong as an illustrative example, considering the availability of a long-term record of quality-assurance tide gauge data. As shown in Figure 3.3, the vine copula ensemble model demonstrated a good performance at the tide gauge in Hong Kong, with a mean Pearson's correlation coefficient of 0.71 and an RMSE of 9.82 cm. The vine copula ensemble model enables a probabilistic estimation, effectively capturing extremely high storm surges. Figure 3.3c shows the reliability and sharpness metrics of the vine copula ensemble model for 16 gauges. The reliability metric, which represents the percentage of observations falling within the predicted confidence intervals, was found to be high for all sites (about 95%). In terms of sharpness that measures the average width of predicted confidence intervals, the range varied from 27 cm to 73 cm, with a mean of 44 cm, demonstrating the flexibility of the vine copula ensemble model.

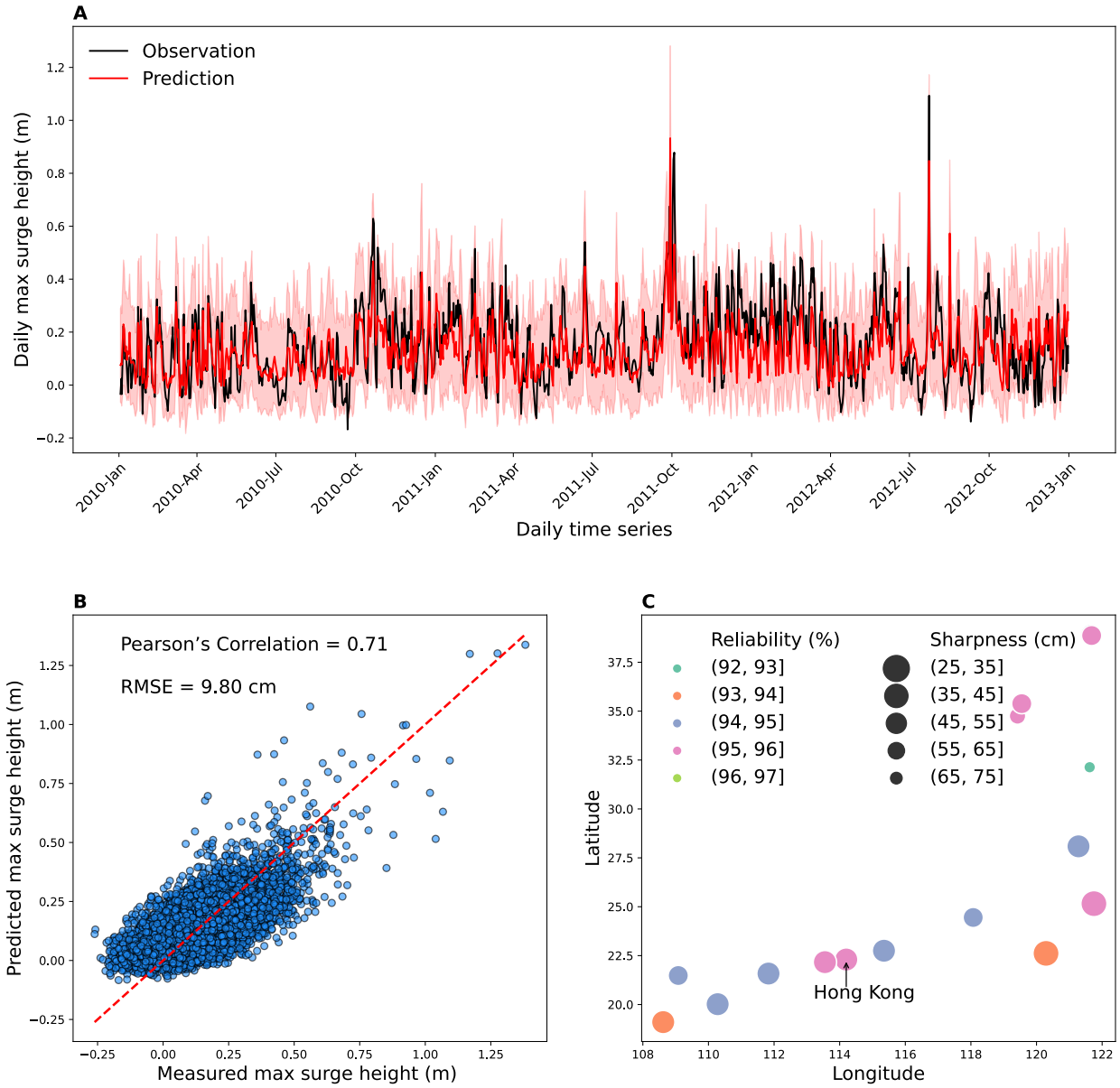

Figure 3.3 Comparison of the observed and predicted daily maximum storm surge extremes (SSE) using the vine copula ensemble model. A: Time series plot of the observed SSE and predicted SSE at the tide gauge in Hong Kong. The time series are cut to the last three years for better illustration. B: Scatter plot of the observed SSE and predicted SSE at the tide gauge in Hong Kong. C: Reliability and sharpness metrics used to measure the performance of probabilistic predictions. The scatter plot shows the tide gauges colored by reliability percentage and sized by the sharpness in centimeters, with one specific point labeled as "Hong Kong". The reliability metric indicates

the percentage of observations that fall within the confidence intervals predicted by the vine copula ensemble model, while the sharpness metric measures the average width of these intervals.

3.1.1.2 Comparison with existing storm surge reconstruction and reanalysis products

I evaluate the performance of the proposed vine copula ensemble model and compared its accuracy with two widely used storm surge datasets: Global Storm Surge Reconstruction (GSSR) and Global Tide and Surge Reanalysis (GTSR). The GSSR database was derived from data-driven models using random forest with the optimal results (Tadesse & Wahl, 2021), while the GTSR dataset was produced through hydrodynamic modeling with the Delft3D Flexible Mesh Suite (Muis et al., 2016). The GSSR database included five different atmospheric reanalysis products, and I select the dataset with the best validation performance, marked as "best reconstruction," for comparison with the proposed vine copula ensemble model across 16 tide gauges. To compare the GTSR dataset, I identify the grid points nearest to each tide gauge in China and then extracted the daily maximum surge values at those specific grid points. I select a common period from 1979 to 2014 for 16 tide gauges, which allowed for a comparable evaluation of daily SSE predicted by the vine copula ensemble model against observations.

As shown in Figure 3.4, the vine copula ensemble model demonstrates superior performance in temporally-continuous storm surge reconstruction compared to both GSSR and GTSR. The mean Pearson's correlation coefficients are 0.62, 0.48, and 0.56 for the vine copula ensemble model, GSSR, and GTSR, respectively. The vine copula ensemble model outperforms the GSSR by 29.09% and the GTSR by 19.35%. For each tide gauge, the vine copula ensemble model achieves higher Pearson's correlation coefficients for all 16 tide gauges compared to GSSR. This advantage is particularly noticeable at locations of Zhapo and Xiamen, where the vine copula ensemble model attains correlation coefficients of 0.74 (Zhapo) and 0.78 (Xiamen), as opposed to 0.60 (Zhapo) and 0.65 (Xiamen) derived by GSSR. Compared to GTSR, the vine copula ensemble model has a slightly better performance, with higher Pearson's correlation coefficients for 10 out of 16 locations.

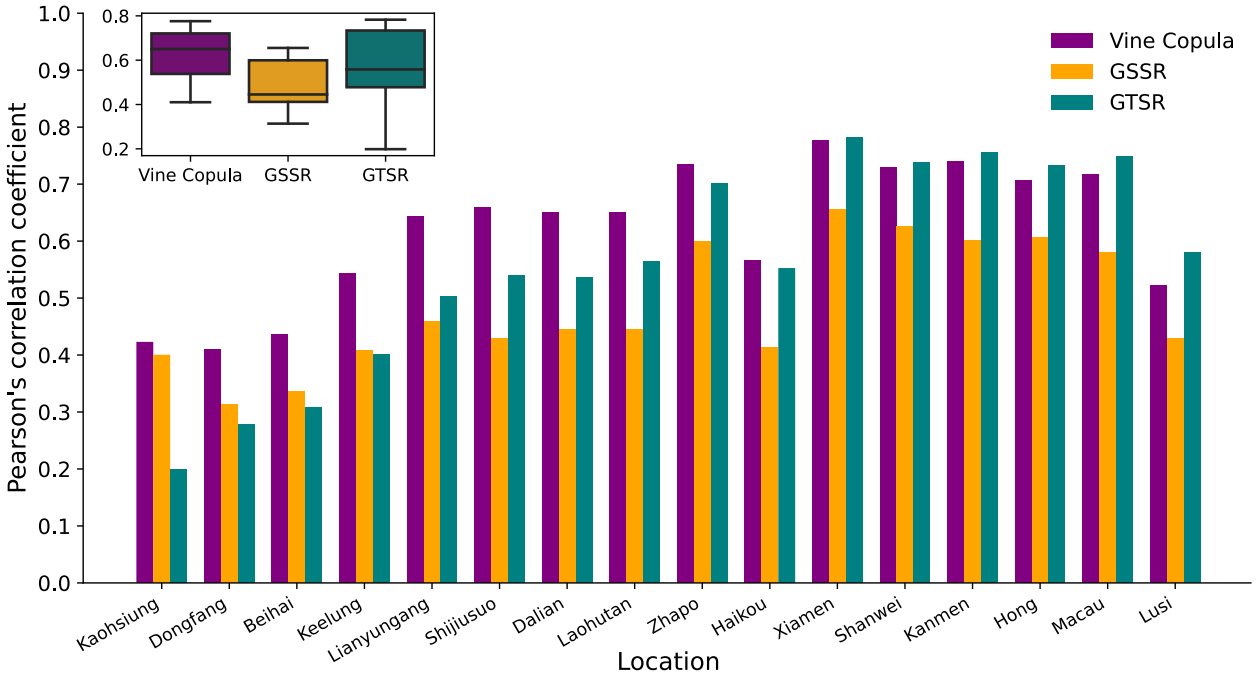

Figure 3.4 Comparison of Pearson's correlation coefficients between observed and predicted daily maximum storm surges. The validation performance of the vine copula ensemble model is compared against Global Storm Surge Reconstruction (GSSR) and Global Tide and Surge Reanalysis (GTSR) products for the period of 1979–2014.

Regarding RMSE (Figure 3.5), the mean values for the vine copula ensemble model, GSSR, and GTSR are 11.43 cm, 14.29 cm, and 15.76 cm, respectively, indicating a percentage improvement of approximately 19.98% compared to GSSR and 27.52% compared to GTSR. The vine copula ensemble model surpasses both GSSR and GTSR methods for most of the locations. Specifically, the vine copula ensemble model yields lower RMSE values for 12 out of the 16 locations when compared to GSSR, and for 11 out of the 16 locations when compared to GTSR. This indicates that the vine copula ensemble model leverages the strengths of RF, CNN, and LSTM models, which can provide more accurate reconstruction of temporally-continuous storm surges along China's coastline.

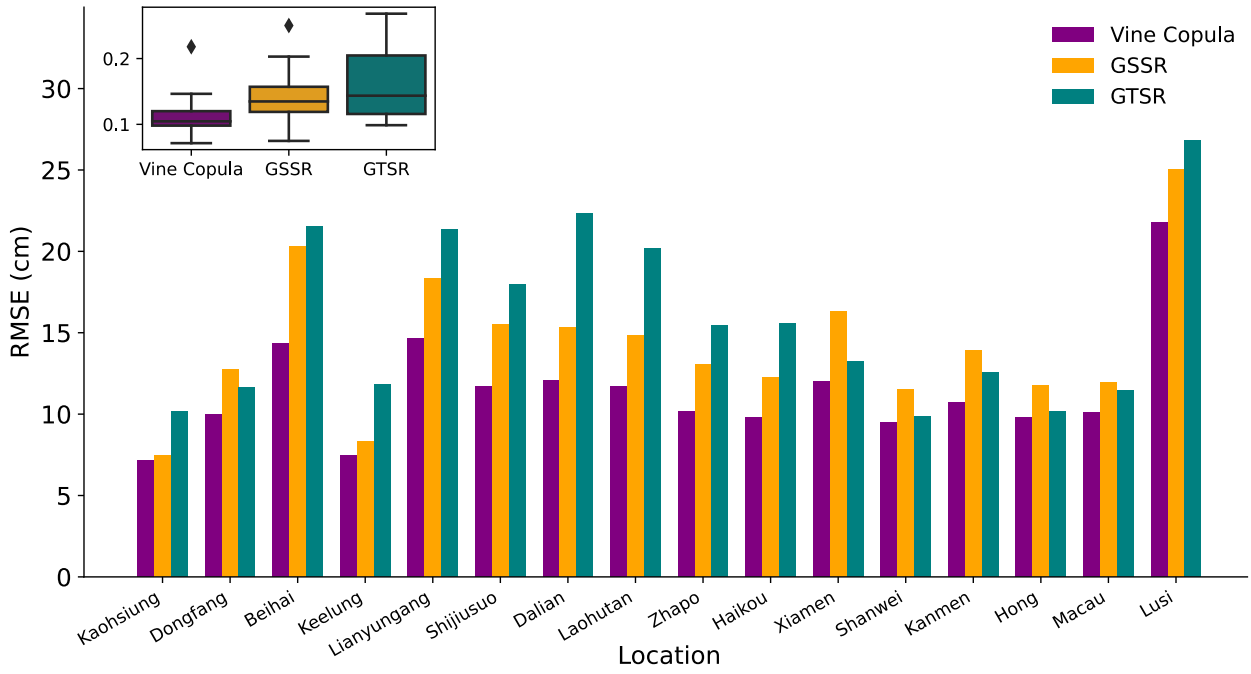

Figure 3.5 Comparison of RMSEs (cm) between observed and predicted daily maximum storm surges derived from the vine copula ensemble model as well as the Global Storm Surge Reconstruction (GSSR) and Global Tide and Surge Reanalysis (GTSR) datasets for the period of 1979–2014.

3.1.2 Validation of spatially-continuous storm surge extremes mapping

I validate the performance of the BHM for estimating GEV parameters at each tide gauge. Given the challenge of unknown true values for GEV parameters, I use a systematic approach involving two key steps. First, I use a full tide gauge dataset to derive probabilistic estimates for GEV parameters based on the BHM (reference values). Second, I successively exclude one tide gauge at a time and utilized the remaining tide gauges to estimate GEV parameters based on the BHM (predicted values). Lastly, I compare two predictions for each tide gauge using the relative error (%) metric. This metric calculates the percentage difference between the reference and predicted values. As shown in Figure 3.6, the average relative error for the location, scale and shape parameters across tide gauges is approximately 14.25%, 8.75% and 4.4%, respectively, suggesting that the GEV parameters estimated by the BHM is relatively accurate. The location

parameter represents the center or mean of the GEV distribution. The results indicate that the estimated location values deviate from the "true" values by approximately 14.25% on average, which can be considered acceptable estimates. The scale parameter governs the spread or variability of the GEV distribution. The lower average relative error for this parameter implies that the estimation of scale values is generally more accurate. The shape parameter is crucial in determining the tail behavior of the GEV distribution, and the lowest relative error for this parameter indicates that the estimation of the shape parameter is most precise among the three types of GEV parameters.

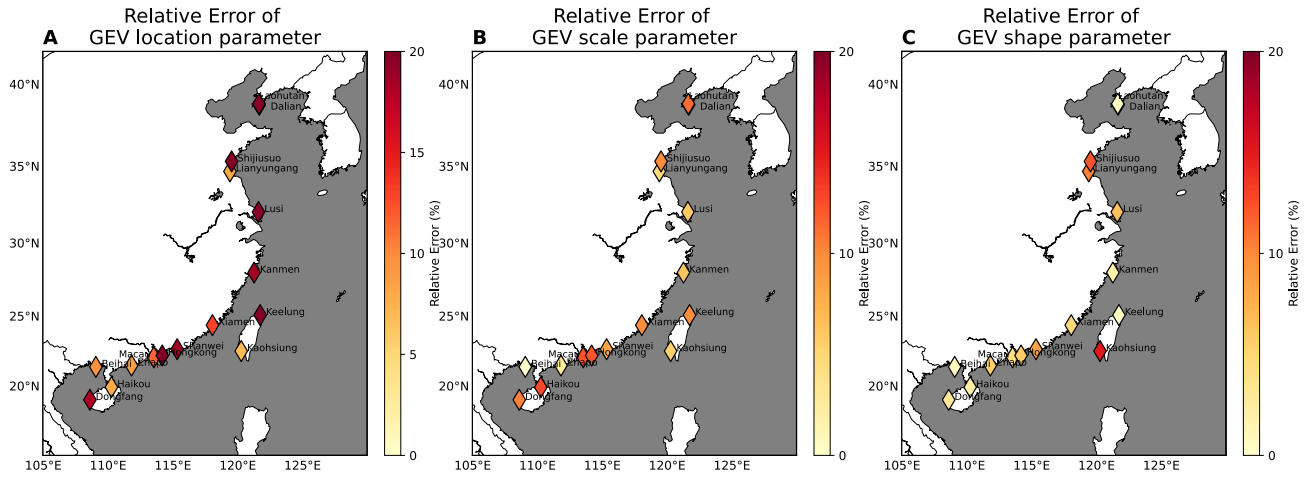

Figure 3.6 Validation of GEV parameters estimated using Bayesian hierarchical model (BHM) across tide gauges. Relative error (%) represents a measure of the quality of parameter estimation, indicating how closely the reference values derived from the full tide gauge dataset align with predicted values using the leave-one cross-validation method.

I further examine the BHM's predictive skill for annual maximum storm surge heights using the leave-one cross-validation method. I calculate the relative errors to assess the accuracy of storm surge height estimates compared to observations. As shown in Figure 3.7a, the storm surge height estimates exhibit relative errors spanning from 3% to 19%, with an average value of 12%. This indicates that, on average, the accuracy of estimating annual maximum storm surge heights at ungauged locations is within 12% of observed values. To address the model uncertainty in interpolating annual maxima at ungauged locations, I calculate the fraction of observed annual maximum storm surge heights that fall within one standard deviation of predicted annual

maximum storm surge heights. The fraction, representing the percentage of observed values captured by one standard deviation of predicted annual maximum storm surge heights, ranges from 59.6% to 82% across the 16 tide gauges (Figure 3.7b). From these 16 tide gauges, I have determined that, on average, about 68.8% of the annual maximum values fall within one standard deviation. This suggests that the estimates of model uncertainty are reasonably accurate and consistent with the theoretical expectation of capturing around 68.3% of the values within one standard deviation. This further demonstrates that the predicted intervals effectively capture the observed values of annual maxima at most tide gauges.

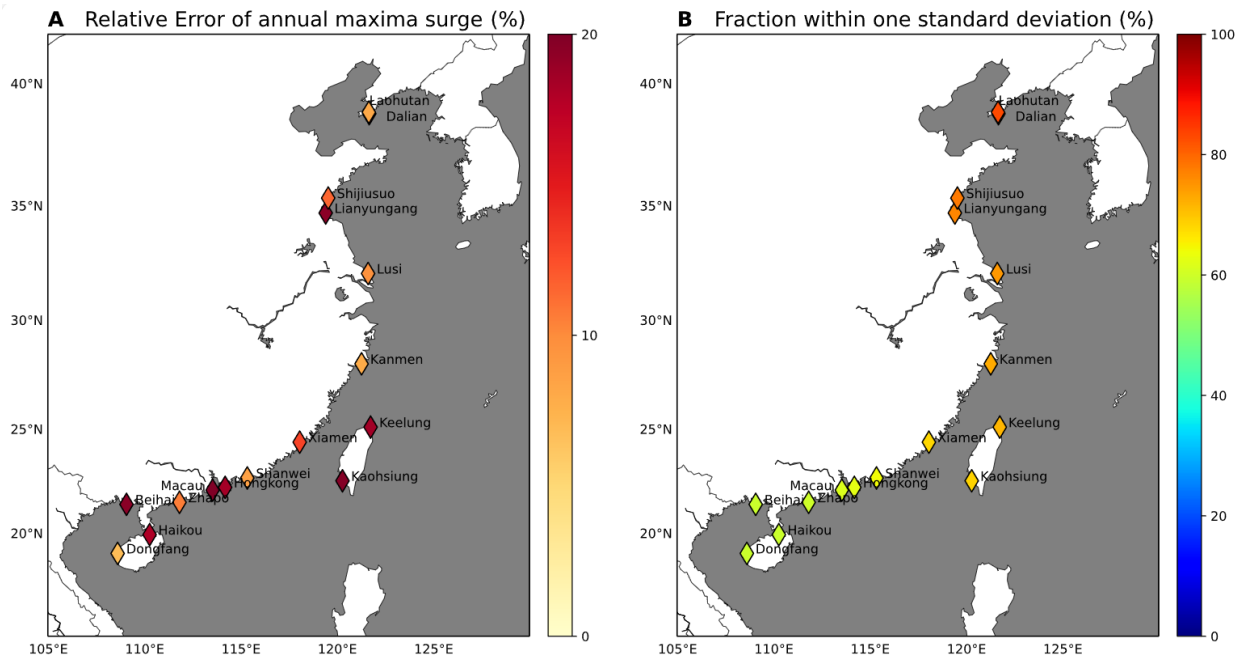

Figure 3.7 Assessment of predictive skill and uncertainty of Bayesian hierarchical model (BHM) for annual maximum storm surge heights. A: Relative error (%) between observed extreme values and BHM estimates. B: Fraction of true values of annual maximum storm surge heights that lie within one standard deviation of BHM estimates (%).

3.1.3 Probabilistic prediction of spatially-temporally-continuous storm surge extremes

I use the vine copula ensemble model to implement the temporally-continuous storm surge extremes (SSE) reconstruction throughout the entire study period (1979–2020) for all tide gauges,

irrespective of observation limitations. Coupled with the spatially-continuous estimation method using the BHM, I can predict the spatially-temporally-continuous extreme storm surges without any spatial or temporal gaps at a 0.25-degree resolution.

The vine copula ensemble model is able to produce a posterior distribution of SSE at ungauged locations, with the mean, lower and upper bounds of the predicted storm surge heights. The lower bound is the value at the 2.5^{th} percentile of the distribution and the upper bound is the value at the 97.5^{th} percentile of the distribution. As depicted in Figure 3.8, the posterior mean of predicted SSE provides an estimation of the most likely or anticipated extreme storm surge height. Throughout various geographical locations, storm surge heights were estimated with a range from 0.54 to 1.29 m, with a mean of about 0.73 m during the 1979–2020 period.

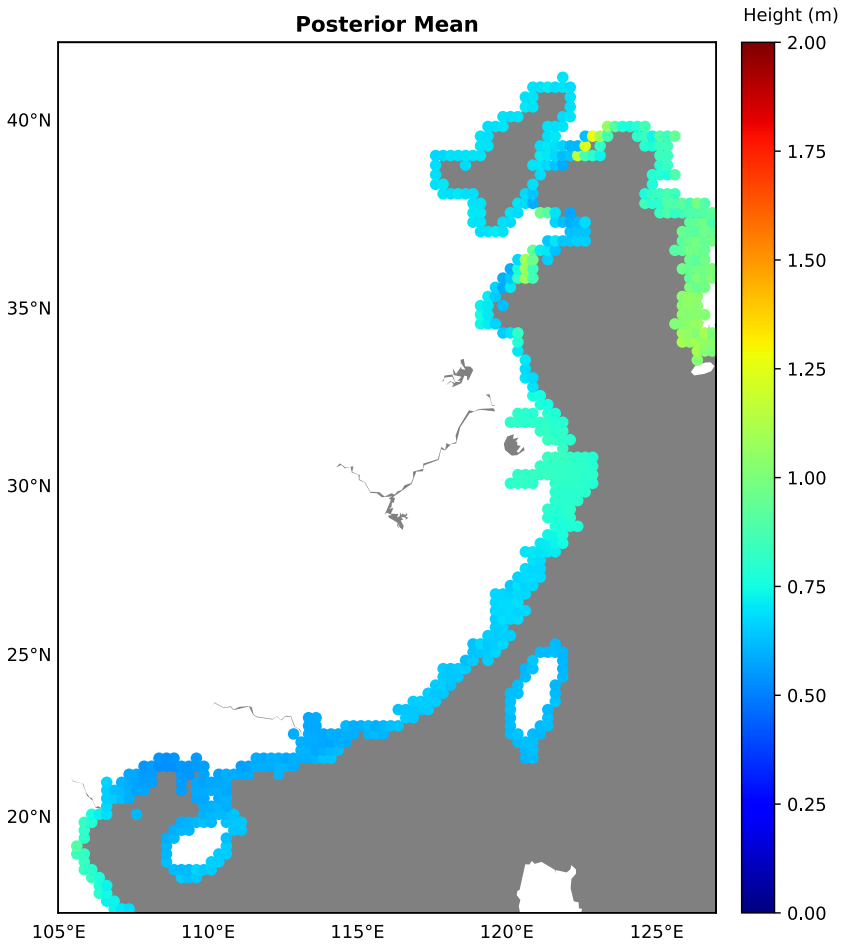

Figure 3.8 Annual maxima of storm surge heights at ungauged locations based on the mean of posterior distribution. The map represents the multi-year mean of posterior distributions for annual maxima of storm surge height, covering the period from 1979 to 2020.

To address the uncertainty inherent in SSE predictions, I also estimate the lower and upper bounds of the predicted storm surge heights. The lower bound, estimated as the value at the 2.5th percentile of the distribution, indicates a 2.5% likelihood that the actual storm surge height might fall below this value (Figure 3.9a). For multiple years during 1979–2020, the average SSE value exhibits a lower bound of extreme storm surge heights ranging from approximately 0.07 to 0.59 m, with a mean of about 0.23 m. Conversely, the upper bound, estimated as the value at the 97.5th percentile of the distribution, represents the worst-case scenario (Figure 3.9b). The predicted storm surge heights, ranging from approximately 1.04 to 3.48 m (with a mean of about 1.49 m), signify a severe situation for coastal regions, with the potential of high-impact consequences.

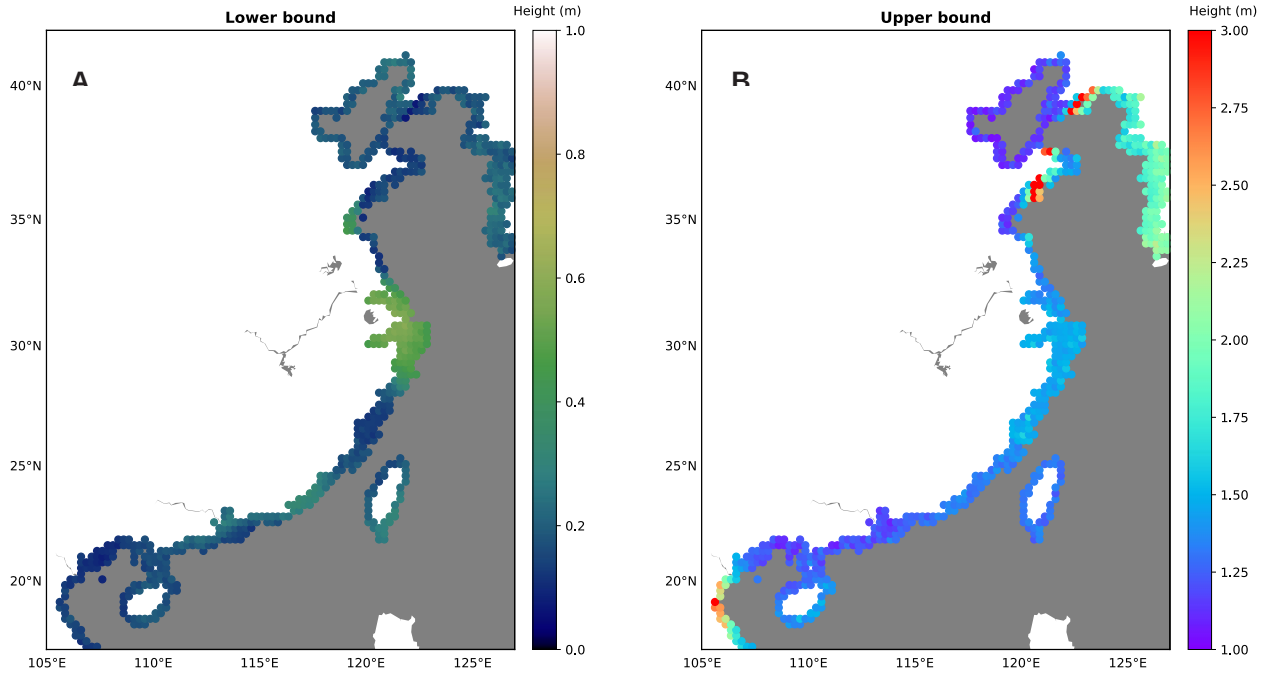

Figure 3.9 Annual maxima of storm surge heights estimated at ungauged locations based on the lower bound (A) and upper bound (B) of posterior distributions. The lower bound is the value at the 2.5th percentile of the distribution and the upper bound is the value at the 97.5th percentile of the distribution. The map represents the multi-year mean during 1979–2020.

The findings reveal a significant spatial variability of the SSE (Figure 3.8 and Figure 3.9). Specifically, I identify two hotspots with higher storm surge heights, including the central part (~30°N, including most areas in Shanghai) and the Northeast part of the study area (~35°N, encompassing most areas in Liaoning province). The increased vulnerability of hotspots to higher storm surge heights can be attributed to the coastal orientation, exposing them to prevailing winds and storm systems originating from distant locations (Liang & Julius, 2017). Furthermore, the bathymetry of the region, characterized by gradually sloping seabeds, plays a crucial role in amplifying storm surge as it approaches the coast (Weaver & Slinn, 2010). Geographical features like bays and river mouths may also act as funneling mechanisms, thereby resulting in amplified storm surge heights along the coastline (Talke et al., 2021).

To better understand the occurrence and intensity of these extreme events, the distribution and return periods of extreme storm surge heights were further estimated. The Generalized

Extreme Value (GEV) distribution was chosen for its accommodation to different types of tail behavior through shape parameters. Compared to alternative distributions like the Generalized Pareto Distribution (GPD) and the Log-Normal distribution, the GEV distribution offers greater flexibility in modeling the tails of extreme data, which is crucial for accurately capturing the potential range of storm surge events. Specifically, I evaluate the return periods of 20, 50, and 100 years for storm surge heights, as depicted in Figure 3.10. For the 20-year recurrence interval (Figure 3.10a), the storm surge heights range from a low of 0.8 m to a high of 2.28 m, with an estimated average value of 1.09 m). While considering the 50-year recurrence interval (Figure 3.10b), there is a slight increase to 1.11 m in the minimum storm surge height and the maximum storm surge height increases to 2.92 m. The mean of storm surge heights significantly rises as high as 1.44 m. As I examine the 100-year recurrence interval (Figure 3.10c), the minimum storm surge height escalates further to 1.62 m and the maximum surge reaches a height of 4.87 m. The average storm surge height also shows a marked increase of up to 1.97 m. While comparing the maximum values of storm surges, the anticipated intensity for the 100-year recurrence interval significantly exceeds those of the 20- and 50-year intervals.

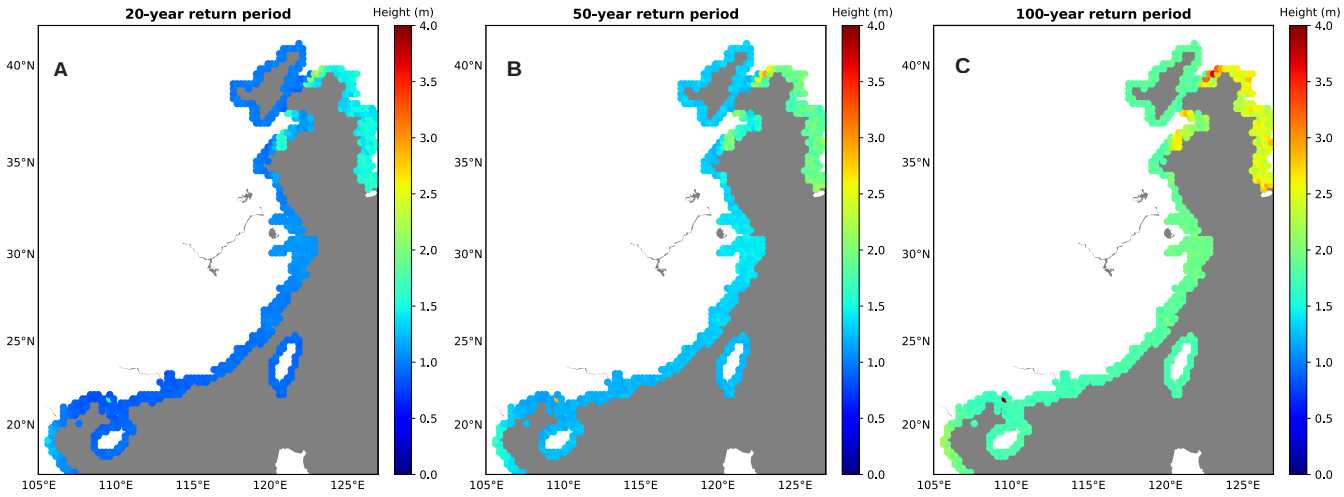

Figure 3.10 Annual maxima of storm surge heights with different return periods: 20-year (A), 50-year (B), and 100-year (C). Return periods are estimated by the Generalized Extreme Value (GEV) approach.

3.2 Spatially seamless and temporally continuous assessment on compound flood risk in Hong Kong

As depicted in Figure 3.11, in Hong Kong, there are only six tidal gauge stations with records spanning 25 to 69 years up to 2022, albeit with some missing values. This sparse and incomplete data complicates the analysis of sea level rise and storm surge patterns at sites without gauges. To address this, this study used the developed modeling framework that combines ensemble machine learning with Bayesian hierarchical models to examine compound coastal flood risk in Hong Kong (Chapter 2.2). First, I achieve the spatial-temporal continuity (10 km, daily) of extreme storm surges and sea level rise data at ungauged sites along the coastline of Hong Kong during 1970–2022. This was accomplished by using the same modeling framework as in the previous section, and more information can be found in Chapter 2.2. Afterwards, these spatial-temporal continuous extreme storm surges and sea level rise data are combined with the widely used precipitation data for a comprehensive analysis of compound coastal flood risk, resulting from the combined effect of extreme storm surges, sea level rise, and heavy rainfall. Finally, I provide a spatially coherent and temporally continuous assessment of compound coastal flood risk, enhancing the understanding of Hong Kong's compound coastal flood hazards.

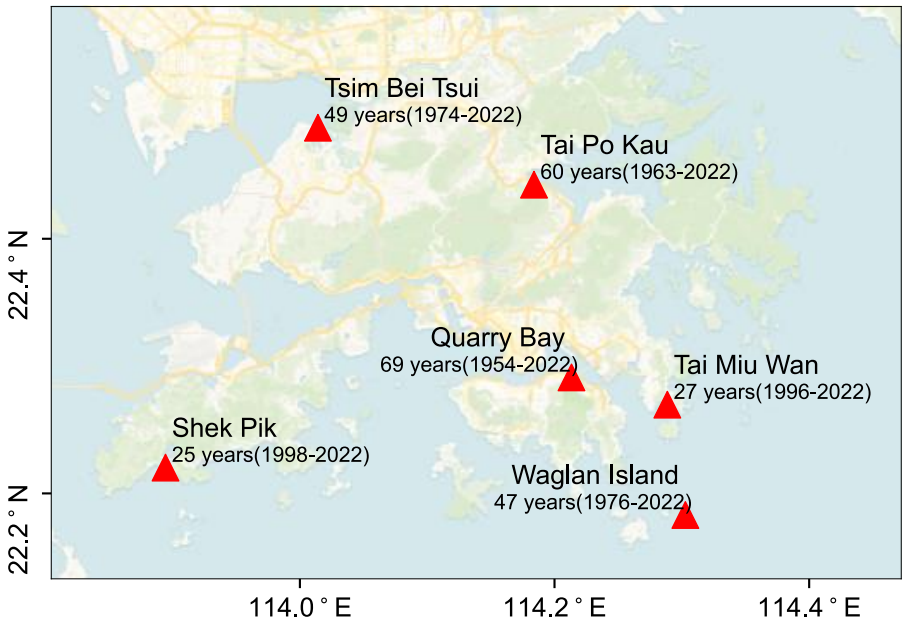

Figure 3.11 Tidal gauge stations in Hong Kong.

Hong Kong, located on China's southeast coast, is a densely populated city with 7.4 million residents spread over 1,110 km² and features a coastline that extends beyond 1,000 km. This coastal city, facing an average of 6 typhoons annually (Hong Kong Observatory, 2012), is particularly vulnerable to compound flooding caused by storm surges, sea level rise, and intense rainfall under a warming climate (He et al., 2016; Wong et al., 2011). This vulnerability is heightened by Hong Kong's geographical features and urbanization. Hong Kong's susceptibility to weather-related threats stems from its low-lying coastal areas and rising sea levels, which have increased by 31 mm per decade since 1954 (Hong Kong Observatory, 2023). Key areas like Victoria Harbour, with an average depth under 12 meters, are especially prone to storm surges. Urbanization further exacerbates coastal flood risks. As one of the world's most densely populated cities, Hong Kong's urban landscape, typified by areas like Kowloon with over 90% urbanization, significantly impedes natural water absorption, increasing runoff. The city's existing infrastructure, particularly its antiquated drainage systems, struggles to cope with the changing patterns and intensities of floods (Qiang et al., 2021). The record-breaking rainfall of 158 mm in an hour in 2023 challenged the systems' capabilities in managing extreme weather events. Therefore, Hong Kong's unique combination of rising sea levels, dense urban layout, and intense rainfall, rooted in its distinct geographical location, makes it an ideal case study for compound flood risk assessment.

3.2.1 Validation and prediction of storm surge heights

Figure 3.12 shows the scatterplot of predicted and observed daily maximum storm surges in six gauges across Hong Kong using the Random Forest (RF), Convolutional Neural Network (CNN), Long Short-Term Memory (LSTM), respectively. Overall, these results indicate that the prediction models perform well in estimating daily maximum storm surge. Among the stations, Shek Pik demonstrated the highest correlation coefficients across all three models, with values of 0.84, 0.80, and 0.80 for RF, CNN, and LSTM, respectively. Quarry Bay also exhibited significant correlations, with coefficients of 0.82, 0.74, and 0.74 for RF, CNN, and LSTM, respectively. Tsim Bei Tsui, Tai Miu Wan, Tai Po Kau, and Waglan Island displayed correlations ranging from 0.80 to 0.82 for RF, 0.71 to 0.80 for CNN, and 0.67 to 0.74 for LSTM.

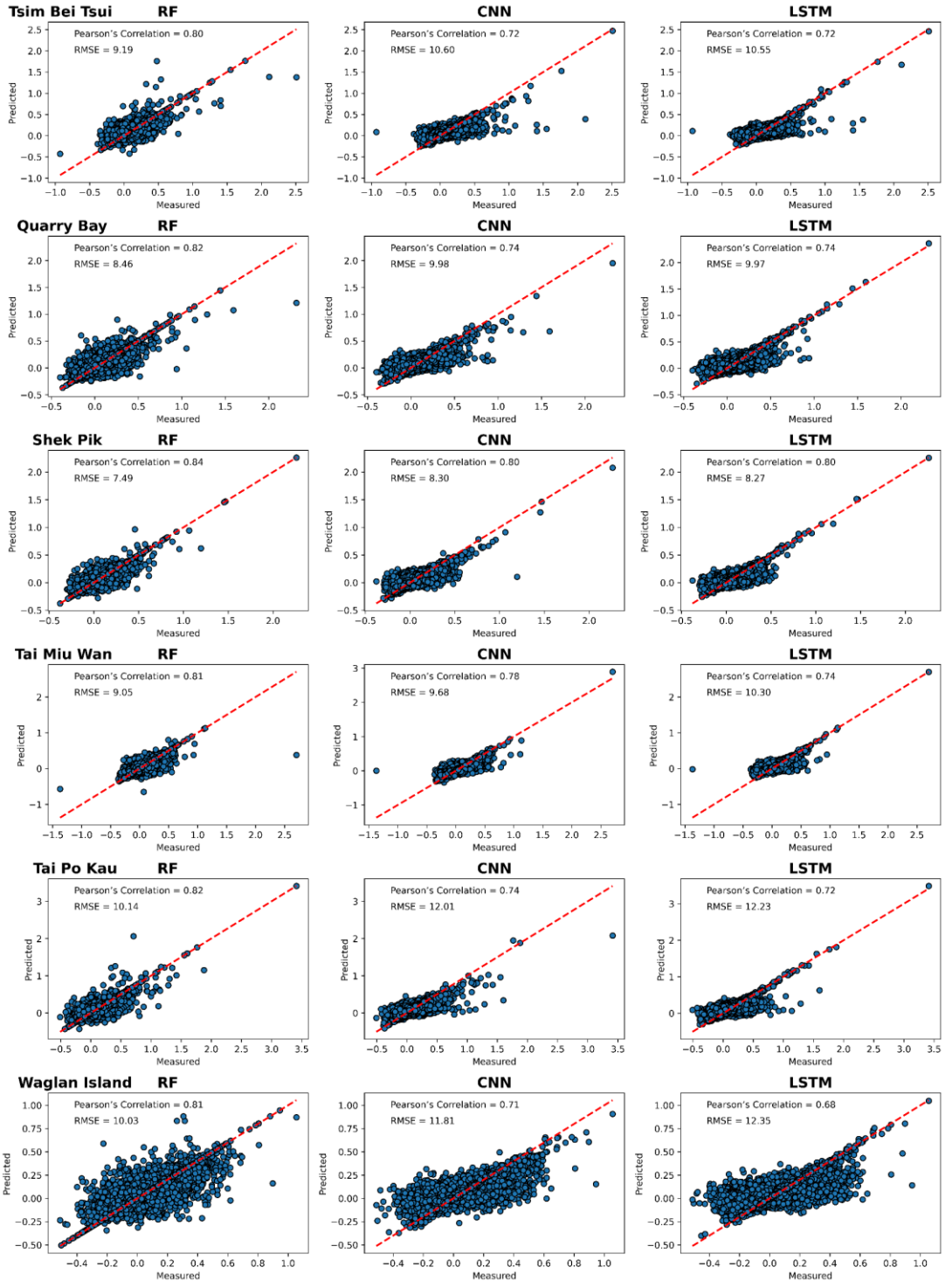

Figure 3.12 Scatterplot of predicted and observed daily maximum storm surges in six gauges. The models include Random Forest (RF), Convolutional Neural Network (CNN) and Long Short-Term Memory (LSTM).

Among the models, the vine copula ensemble method demonstrates the strongest correlation coefficients for all sites, with values ranging from 0.82 to 0.86, as shown in

Figure 3.13. In terms of RMSE values, the vine copula ensemble method achieved the lowest errors for all sites, with values ranging from 7.08 cm to 9.64 cm. The results suggest that the vine copula ensemble method merges the advantages of the RF, CNN, and LSTM models to achieve the highest accuracy in predicting storm surge extremes. Overall, the use of vine copula ensemble method in combination with other individual methods can help to address the limitations of individual models and provide a more accurate and robust prediction of complex events, such as storm surge extremes.

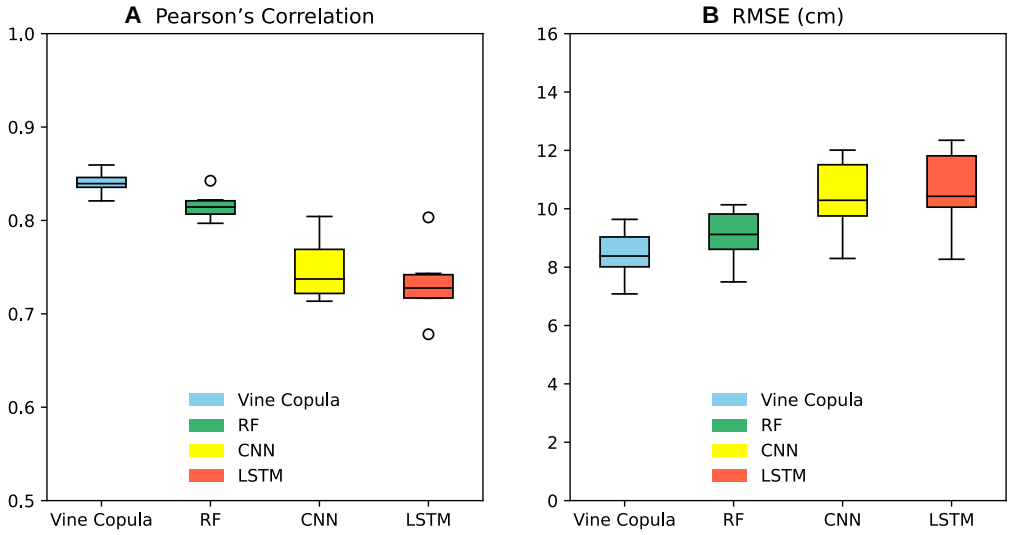

Figure 3.13 Comparison of model performance for four models across six gauges. The models include Random Forest (RF), Convolutional Neural Network (CNN), Long Short-Term Memory (LSTM), and vine copula ensemble. A: Pearson's correlation. B: Root Mean Squared Error (RMSE). C and D are the maps of Pearson's correlation and RMSE between predicted and observed daily maximum storm surges across six gauges using the vine copula ensemble method, respectively.

Figure 3.14 presents the average results of a Bayesian Hierarchical Model (BHM) used to predict storm surge heights over a multiyear period, from 1979 to 2022. The model generates a posterior distribution, which represents the probabilities of different outcomes for the storm surge height given the available data. The results are aggregated in terms of the mean, lower bound (2.5^{th}

percentile), and upper bound (97.5th percentile) of the predicted storm surge heights. As shown in Figure 3.14a, the mean storm surge height provides an estimate of the most probable or expected storm surge. Across the geographical locations included in the dataset, storm surge heights ranged from approximately 0.64 to 1.06 m, with an overall average of about 0.87 m during 1979-2022. This mean storm surge height represents the most probable or expected storm surge height based on the model. Higher storm surge heights are observed in the northern parts of Hong Kong.

The northern parts of Hong Kong were estimated to be more exposed to higher storm surge heights based on predictions from ungauged stations. This is likely due to the coastal orientation, facing the prevailing winds and storm systems that come from the south or southeast. Additionally, the bathymetry of the area, including gradually sloping seabeds, can contribute to the build-up of storm surges as they approach the coast. Geographical features such as bays or river mouths may also act as funneling mechanisms, concentrating storm surges and leading to increased heights along the northern coastline.

To account for the uncertainty inherent in such predictions, I also calculate the lower and upper bounds of the predicted storm surge heights (Figure 3.14, panels B and C),). The lower bound is the value at the 2.5th percentile of the distribution, suggesting a 2.5% chance that the actual storm surge height could be below this value. These values ranged from approximately 0.20 to 0.51 m, with an overall average of about 0.42 m. Similarly, the upper bound is the value at the 97.5th percentile of the distribution, indicating a 2.5% chance that the actual storm surge height could be above this value. The predicted storm surge height values ranging from approximately 1.11 to 1.93 m, with an overall average of about 1.60 m, indicate a significant and potentially dangerous situation for coastal areas.

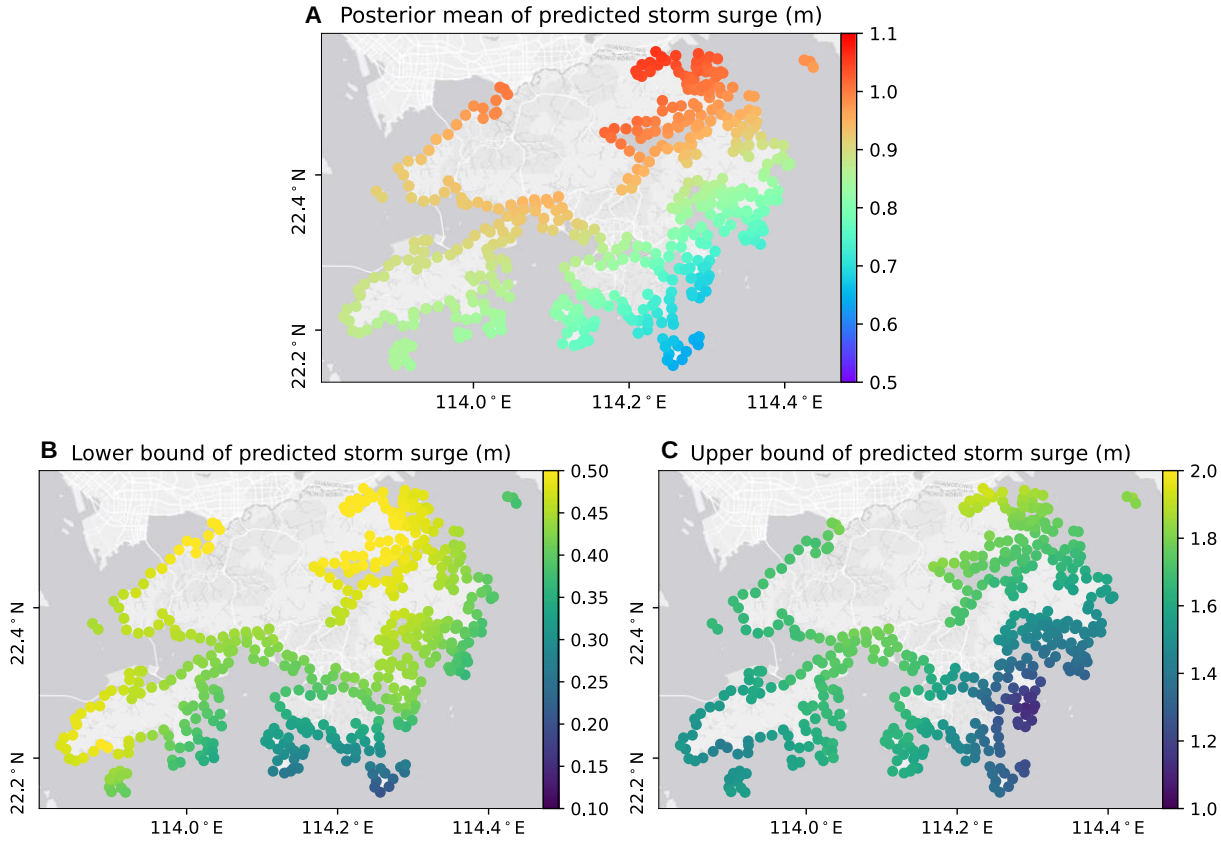

Figure 3.14 The seamless mappings of storm surge heights in Hong Kong. Panel A displays the posterior mean distribution of extreme storm surge heights, spanning the years 1979 to 2022. Panel B and C depict the range of uncertainty in storm surge forecasts, with the lower limit represented by the 2.5th percentile and the upper limit by the 97.5th percentile of the distribution.

Building on the above foundation, I have successfully produced and compiled an extensive dataset of daily and spatially-continuous storm surge information along the entire Hong Kong coastline, covering a period from 1979 to 2022 (Figure 3.15). After applying the Mann-Kendall test to analyze the data, I find that there is a statistically significant increase in the average annual maximum storm surge levels in Hong Kong, quantified as a rise of 3 mm per year at a significance level of 0.05. The Mann-Kendall test confirms a consistent and significant upward trend in extreme storm surges over the years. This finding underscores the growing impact of extreme storm surges on the region.

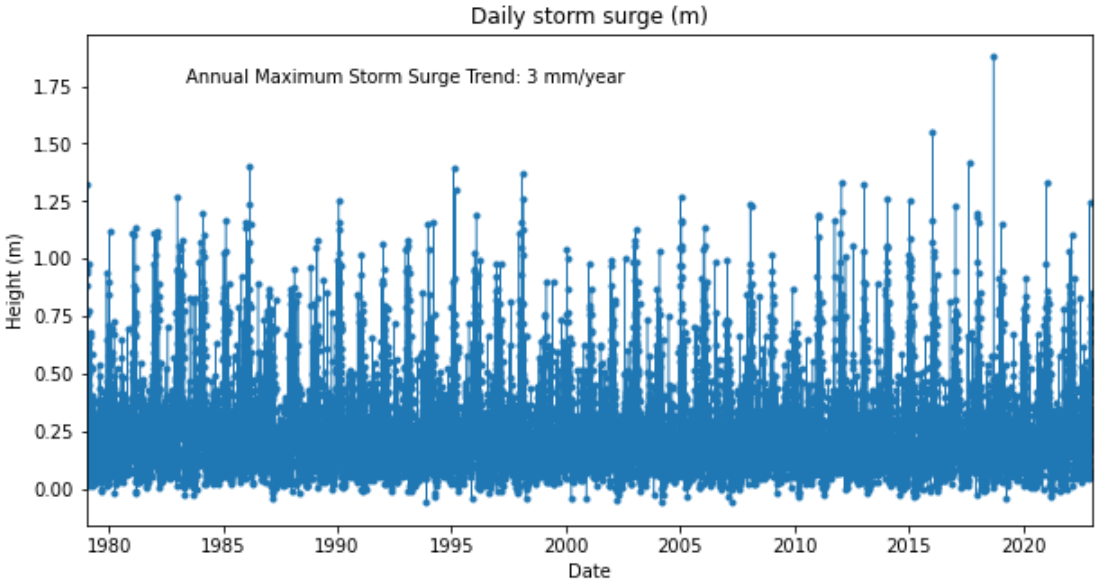

Figure 3.15 Daily time series of storm surge from 1979 to 2022.

3.2.2 Validation and prediction of mean sea level heights

Similar to the methodology for storm surge prediction, I implement an ensemble machine learning framework. This framework was specifically designed for the probabilistic prediction of spatially and temporally continuous mean sea levels in coastal regions of Hong Kong. Through this advanced modeling approach, I am able to capture both the spatial variability along the coastline and temporal changes of sea level rise over the years. With this robust framework, I compiled an extensive dataset of daily, spatially-continuous mean sea level readings along the entire coastline. This dataset spans a significant period, from 1979 to 2022, providing a comprehensive view of sea level trends in the region. The resulting insights contribute significantly to the understanding of sea level dynamics and their implications for coastal management and future planning in Hong Kong.

Leveraging an ensemble machine learning framework enhances the accuracy and reliability of estimating or predicting the mean sea level at ungauged stations in the coastal regions. Figure 3.16presents the performance of models across different gauges. Quarry Bay stands out with a notably high correlation coefficient of 0.82, followed by Tsim Bei Tsui at 0.73. A closely clustered correlation is observed among Shek Pik, Tai Miu Wan, Tai Po Kau, and Waglan Island, with their

coefficients ranging narrowly from 0.79 to 0.81. Model accuracy through Root Mean Square Error (RMSE) values was evaluated, also shown in Figure 3.16. Shek Pik leads with the most precise mean sea level predictions, reflected in the lowest RMSE of 9.4 cm. Additionally, Quarry Bay, Tsim Bei Tsui, Tai Miu Wan, Tai Po Kau, and Waglan Island demonstrate RMSE values varying from 9.5 cm to 11.9 cm.

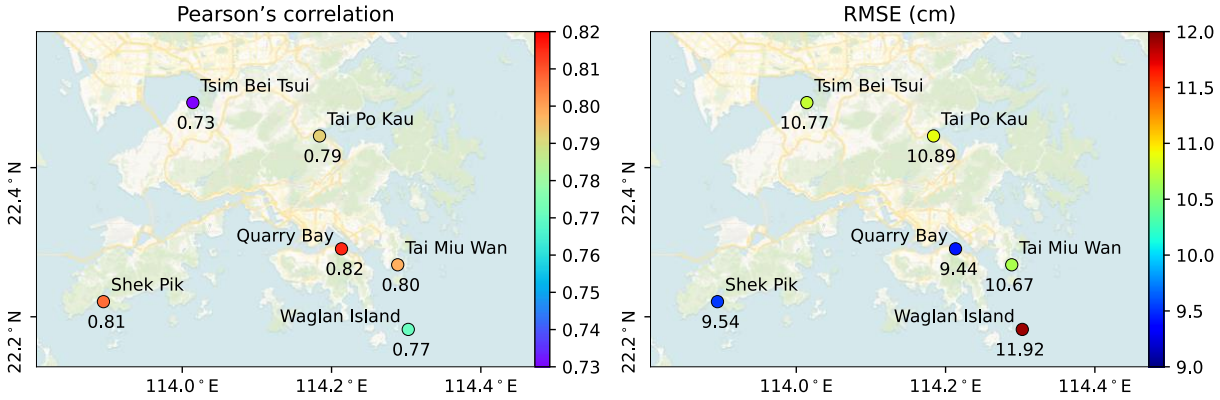

Figure 3.16 Pearson's correlation between predicted and observed daily mean sea level across six gauges using the vine ensemble machine learning framework.

Understanding sea level at ungauged sites is essential for assessing the potential impacts of climate change, particularly for low-lying areas that are vulnerable to sea level rise. The results can provide spatially-temporally continuous mean sea level mappings at coastal locations where no direct observational data (gauges) are available (Figure 3.17). Generally, the climatological mean sea level in Hong Kong, aggregated across all ungauged sites along the coastline, was recorded at 1.46 meters over the period from 1979 to 2022. This measurement reflects the average sea level height during this extensive time frame, encompassing various unmonitored coastal locations and offering a comprehensive overview of sea level in the region.

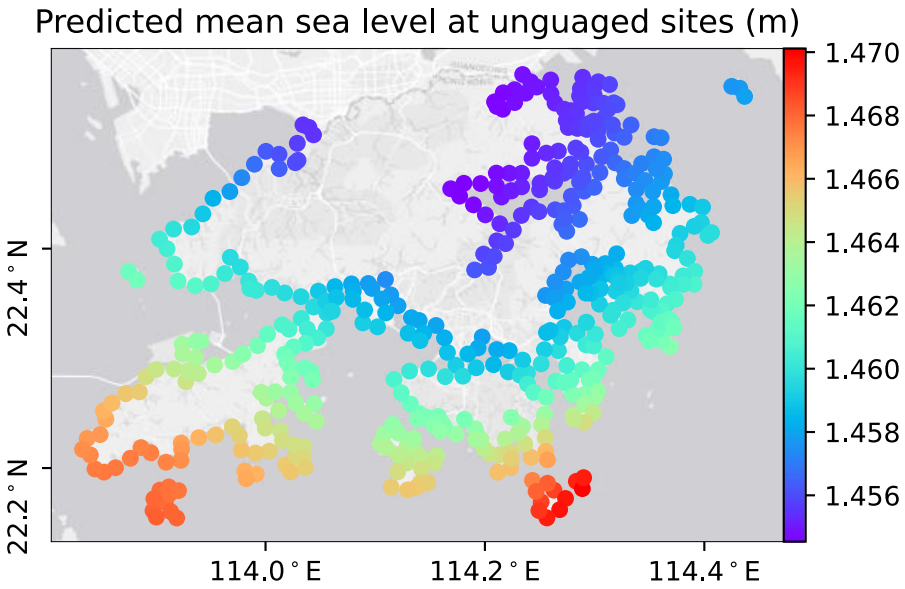

Figure 3.17 Continuous spatial-temporal mappings of mean sea level. This map showcases the multi-year mean spanning from 1979 to 2022.

Building upon the comprehensive daily time series data of mean sea level from 1979 to 2022 (Figure 3.18), the analysis provides a deeper understanding of sea level changes in Hong Kong. Utilizing the Mann-Kendall test, I have identified a consistent and significant upward trend in mean sea level. The findings reveal a statistically significant increase in the average mean sea level in Hong Kong, quantified as a rise of 25 mm per decade, at a significance level of 0.05. This pronounced increase, corroborated by the trend observed over the years, aligns with broader patterns of sea level rise in the region and reflects the ongoing impacts of climate change. The data not only underscores the reality of rising sea levels but also emphasizes the urgent need for adaptive and mitigation strategies to protect coastal communities and ecosystems in Hong Kong against the consequences of sea level rise.

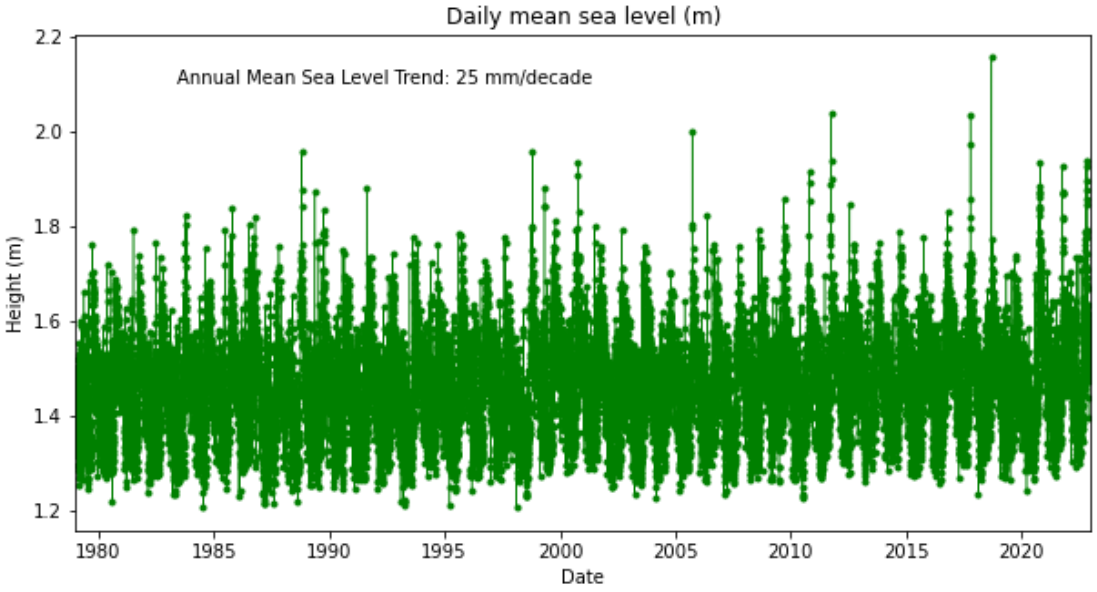

Figure 3.18 Daily time series of mean sea level from 1979 to 2022.

3.2.3 Extreme rainfall event analysis

I utilize the MSWEP dataset (Beck et al., 2019), a comprehensive 0.1° daily precipitation product spanning from 1979 to 2022. Recognized for its high accuracy and widespread use, this dataset was used to investigate precipitation patterns along the coastline of Hong Kong. I employ the Mann-Kendall test to evaluate the trend in annual maximum daily rainfall intensities. The analysis reveals a significant increase in the daily heavy rainfall intensities, particularly in the southwestern and northeastern coastline of Hong Kong (Figure 3.19). These findings are important because they indicate that these areas of Hong Kong are experiencing more intense rainfalls than ever before. This could have implications for managing flood risks and making preparations for days with intense rainfall in Hong Kong.

I also investigate the thresholds for heavy and extreme rainfall in Hong Kong. The heavy rainfall threshold, indicated by the 95th percentile, is a crucial indicator for defining heavy rainfall

events. The analysis shows that the average heavy rainfall threshold across the dataset was 37.68

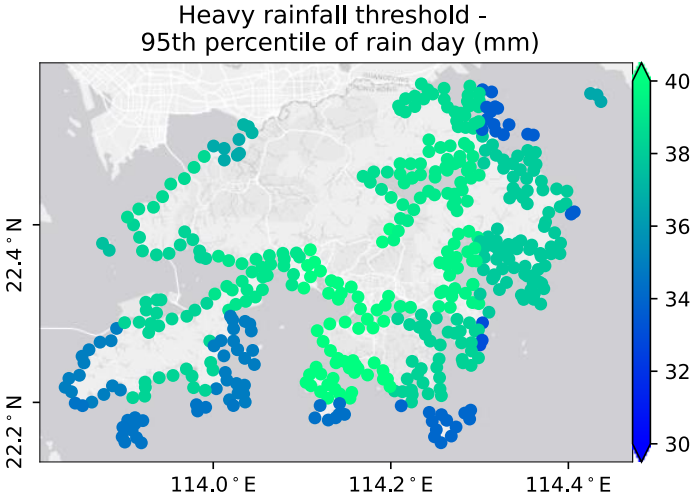

mm (

Figure 3.20a). The extreme rainfall threshold, marked by the 99th percentile, is significant for identifying exceptionally intense rainfall events. The average threshold for extreme rainfall was

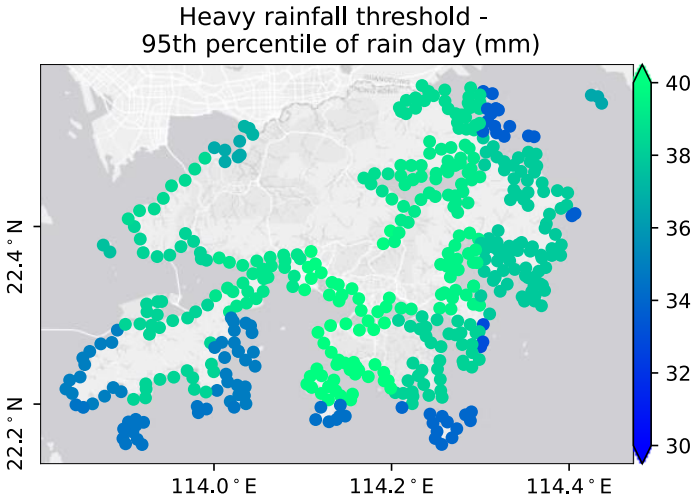

found to be 80.05 mm (

Figure 3.20b). The thresholds for heavy and extreme rainfall exhibit spatial variation, with the central coastal regions displaying higher thresholds. This indicates a higher precipitation in these areas. These findings provide an in-depth quantitative foundation for understanding the intensity and variability of heavy and extreme rainfall in Hong Kong. It also has significant implications for urban planning, especially in designing flood risk management and emergency response strategies in the face of increasingly volatile weather patterns.

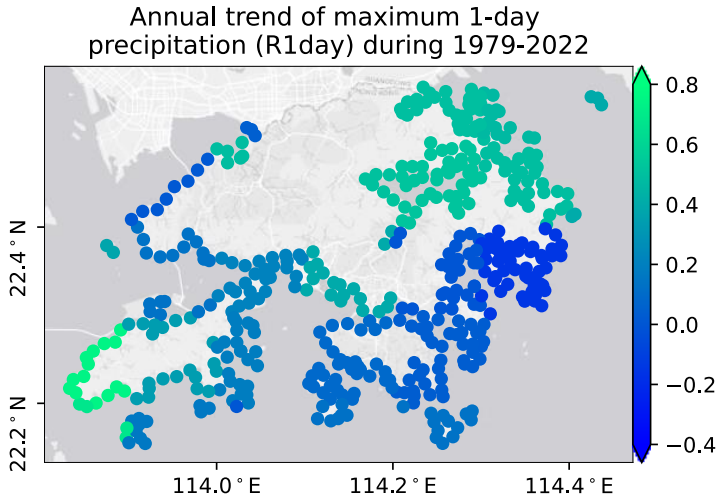

Figure 3.19 Extreme annual trend of maximum 1-day precipitation (R1day) during 1979-2022 using Mann-Kendall test.

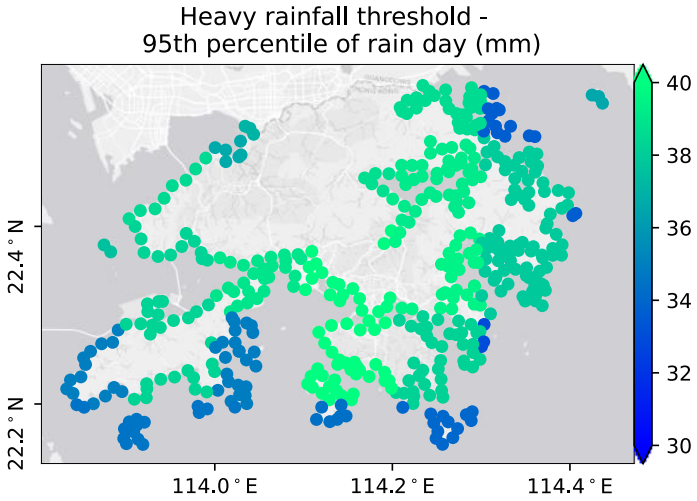

Figure 3.20 Heavy rainfall thresholds from 1979 to 2022.

3.2.4 Compound flood risk analysis

Upon achieving the comprehensive collection of daily spatially-continuous data on storm surge, sea level rise, and heavy rainfall in Hong Kong, I further explored the interactions among these drivers in the context of compound flooding. As shown in Figure 3.21, The interaction among storm surges, rising sea levels and heavy rainfall is of special important. Sea level rise can exacerbate the effects of storm surges, leading to higher and more damaging coastal floods. When coupled with heavy rainfall, especially during extreme weather events, the risk of severe flooding can be amplified. This is critical in Hong Kong, which is exceptionally prone to these challenges. The city's geographical characteristics, with a substantial portion of its densely populated urban areas and critical infrastructure situated in low-lying coastal zones, heightens its vulnerability.

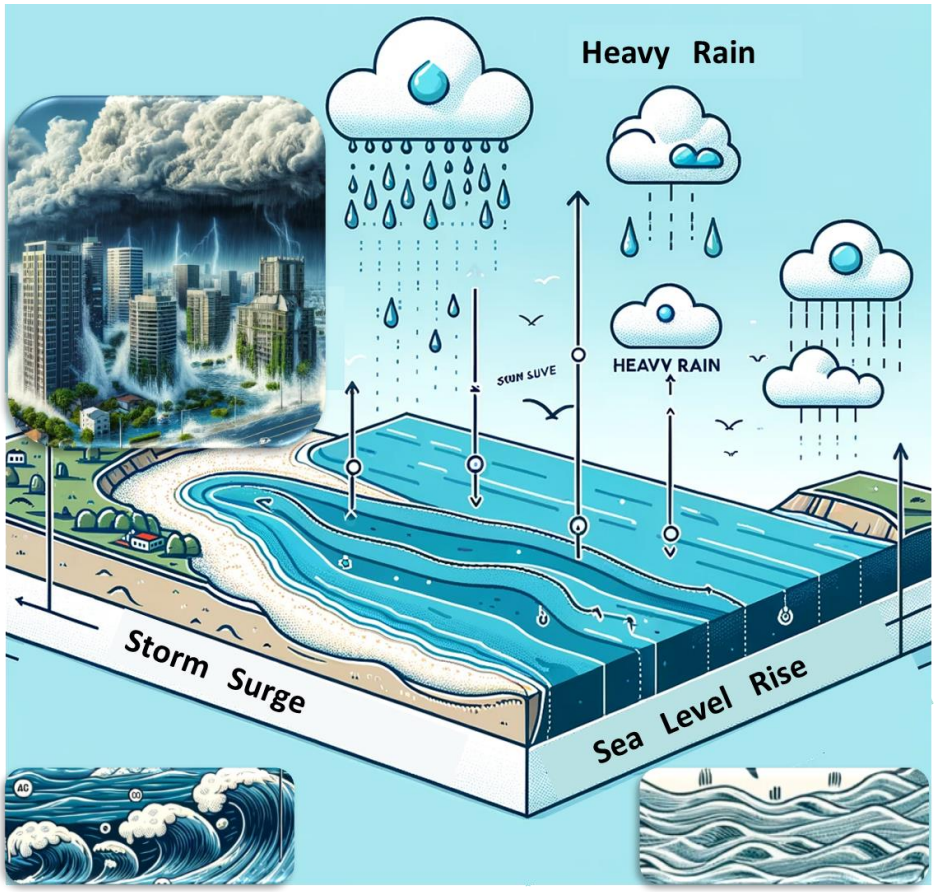

Figure 3.21 The schematic diagram for illustrating the interaction among storm surge, sea level rise, and heavy rain contributing to compound flooding.

To investigate compound flooding in Hong Kong, three primary drivers were identified: extreme storm surge, sea level rise, and heavy rainfall. These drivers are defined based on statistical thresholds. An extreme storm surge, termed "extreme_surge," is characterized by daily maximum storm surges surpassing the 95th percentile. Sea level rise, referred to as "extreme_msl," is defined by daily mean sea levels exceeding their 95th percentile. Heavy rainfall, denoted as "heavy_rain," is identified as daily rainfall amounts crossing the 95th percentile on wet days. As shown in Table 1, I reveal significant dependence between these flood drivers. During the time period from 1979 to 2022 in Hong Kong, I find the concurrence of heavy rainfall events with extreme storm surges. Results show that heavy rainfall events were accompanied by extreme storm surges in approximately 14.54% of occurrences, as indicated by the average conditional probability *P(extreme_surge | heavy_rain)* (Table 3-1, Figure 3.22a). In contrast, the inverse relationship, characterized by the presence of heavy rainfall during periods of extreme storm surges, manifested less frequently, with a mean probability of 9.58% (*P(heavy_rain | extreme_surge)*) (Figure 3.22b).Additionally, the likelihood of encountering sea level rise conditions concurrent with heavy rainfall was quantified at 13.69% (*P(extreme_msl | heavy_rain)*) (Figure 3.22). Conversely, the incidence of heavy rainfall during episodes of extreme mean sea level was calculated to be 9.00% (*P(heavy_rain | extreme_msl)*) (Figure 3.22d).

In the context of compound flooding involving all three identified drivers, the average probability of simultaneous extreme storm surge and extreme mean sea level conditions during heavy rainfall was estimated to be 10.66% (Table 3-1, Figure 3.22e). Similarly, the co-occurrence probabilities of heavy rainfall with extreme mean sea level during extreme storm surges, and of heavy rainfall with extreme storm surges during extreme mean sea level events, were both determined to be 7.03% (Figure 3.22f). These findings underscore the interdependencies among the different drivers of compound flooding in Hong Kong, which is essential for informing flood risk assessment and management strategies in the region.

Table 3-1 The average conditional probabilities for compound flooding involving two or three drivers: extreme storm surge, sea level rise, and heavy rainfall in Hong Kong.

Compound flooding by two or three drivers		Average conditional probability
Two drivers: extreme storm surge and heavy rainfall	*P(extreme_surge | heavy_rain)*	14.54%
	P(heavy_rain | extreme_surge)	9.58%
Two drivers: sea level rise and heavy rainfall	*P(extreme_msl | heavy_rain)*	13.69%
	P(heavy_rain | extreme_msl)	9.00%
Three drivers: extreme storm surge, sea level rise and heavy rainfall	*P([extreme_surge & extreme_msl] | heavy_rain)*	10.66%
	P([heavy_rain & extreme_msl] | extreme_surge)	7.03%
	P([heavy_rain & extreme_surge)]| extreme_ msl)	7.03%

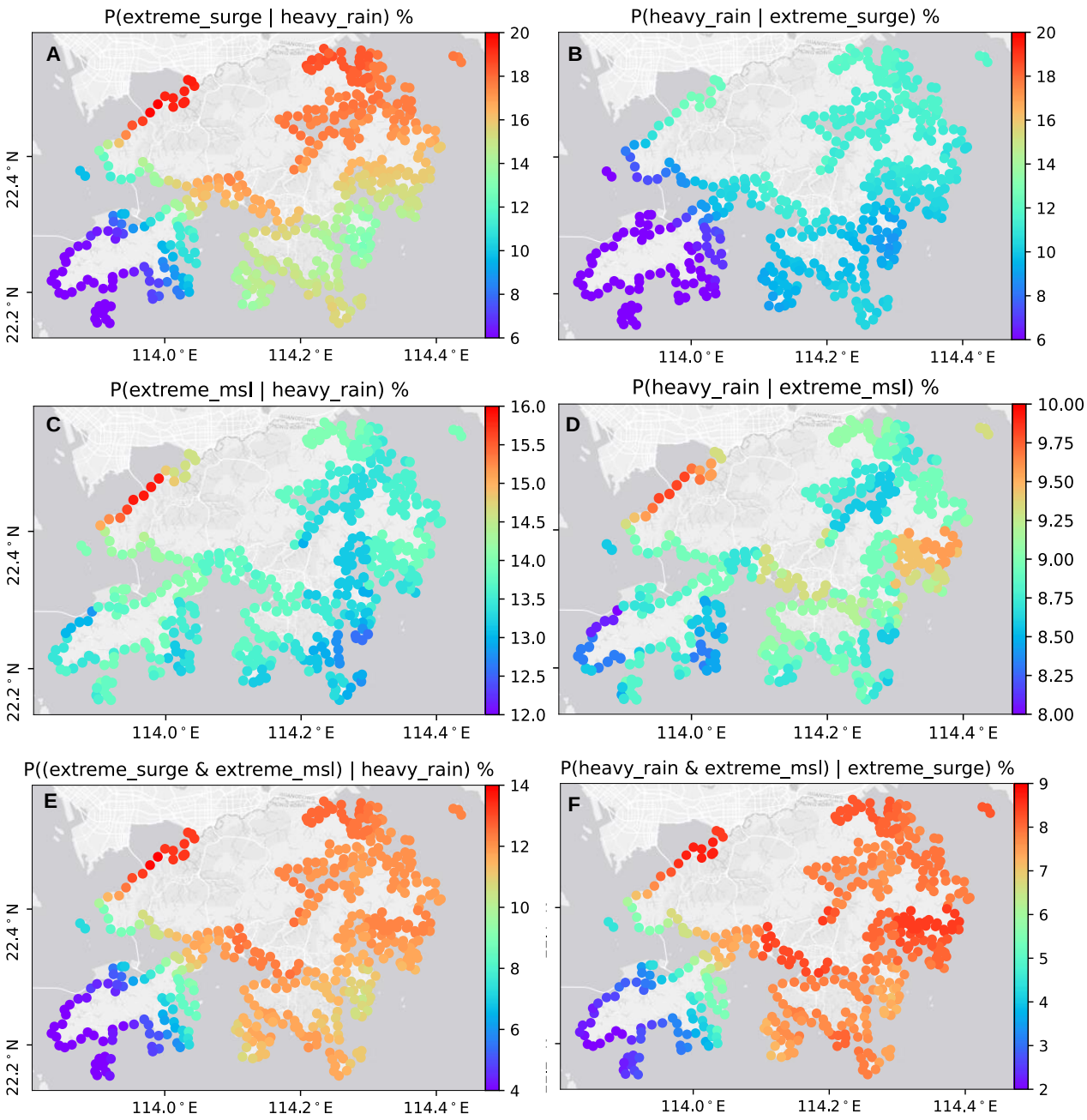

Figure 3.22 The conditional probability of compound flooding due to different combinations of extreme storm surge, sea level rise and heavy rainfall.

I use copulas to model and analyze the dependencies between multiple variables among storm surge, sea level rise, and heavy rainfall. This approach is particularly effective in understanding

the complex, non-linear relationships that exist among these factors. As shown in

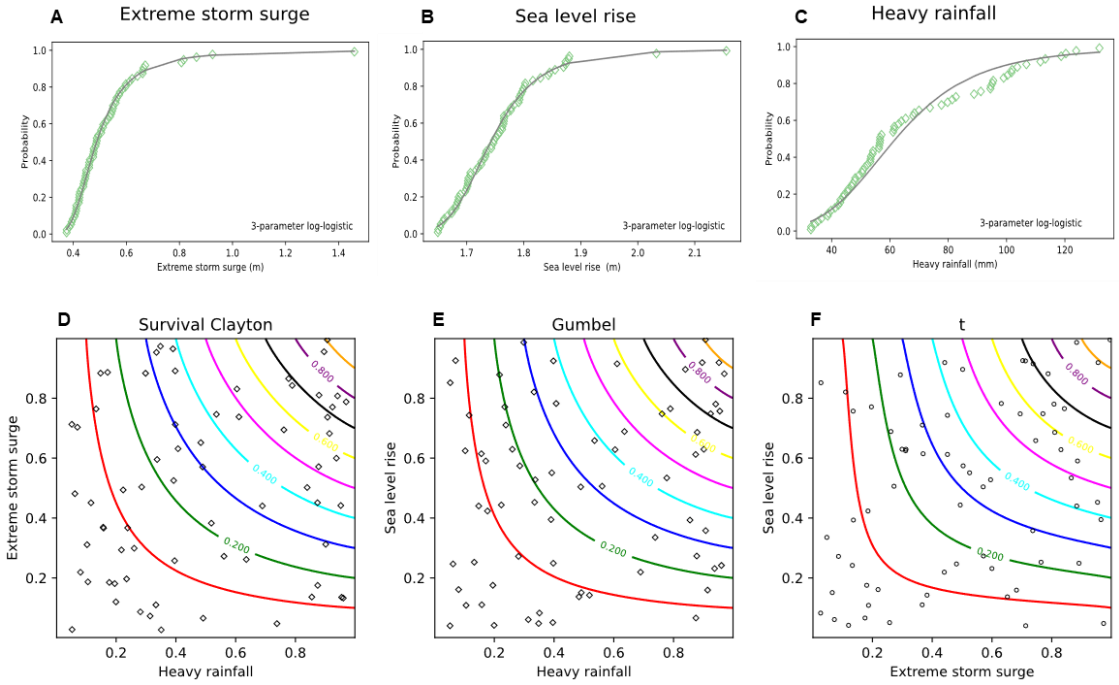

Figure 3.23 (panels A, B, and C), the three-parameter log-logistic distribution closely aligns the cumulative probabilities with the empirical probabilities observed in the cases of extreme storm surge, sea level rise, and heavy rainfall.

Subsequently, the cumulative probabilities were used to develop bivariate copulas for extreme storm surge, sea level rise, and heavy rainfall.

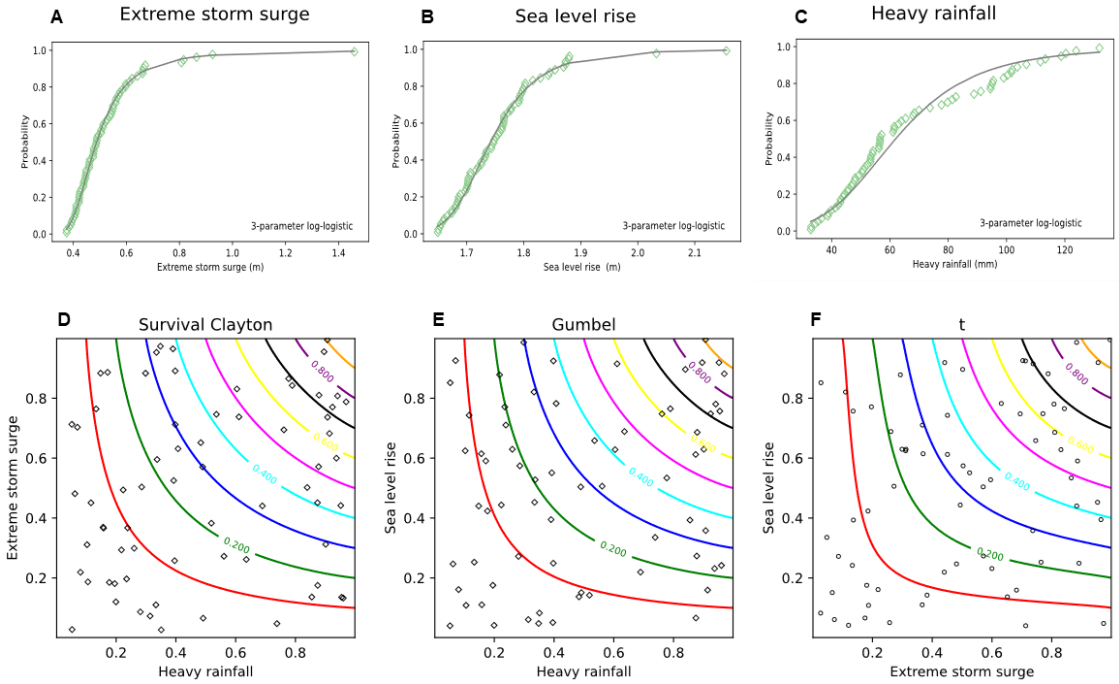

Figure 3.23 (panels D, E, and F) show the contours of bivariate CDFs derived from the chosen copulas. Positive dependencies observed in bivariate events suggest the likelihood of compound flooding in coastal areas of Hong Kong. Notably, the Survival Clayton copula emerged as the most fitting model to describe the interdependency between heavy rainfall and extreme storm surges. In contrast, the Gumbel copula was found to be suitable for capturing the relationship between heavy rainfall and sea level rise, whereas the Student-t copula represented the best dependence between extreme storm surges and sea level rise.

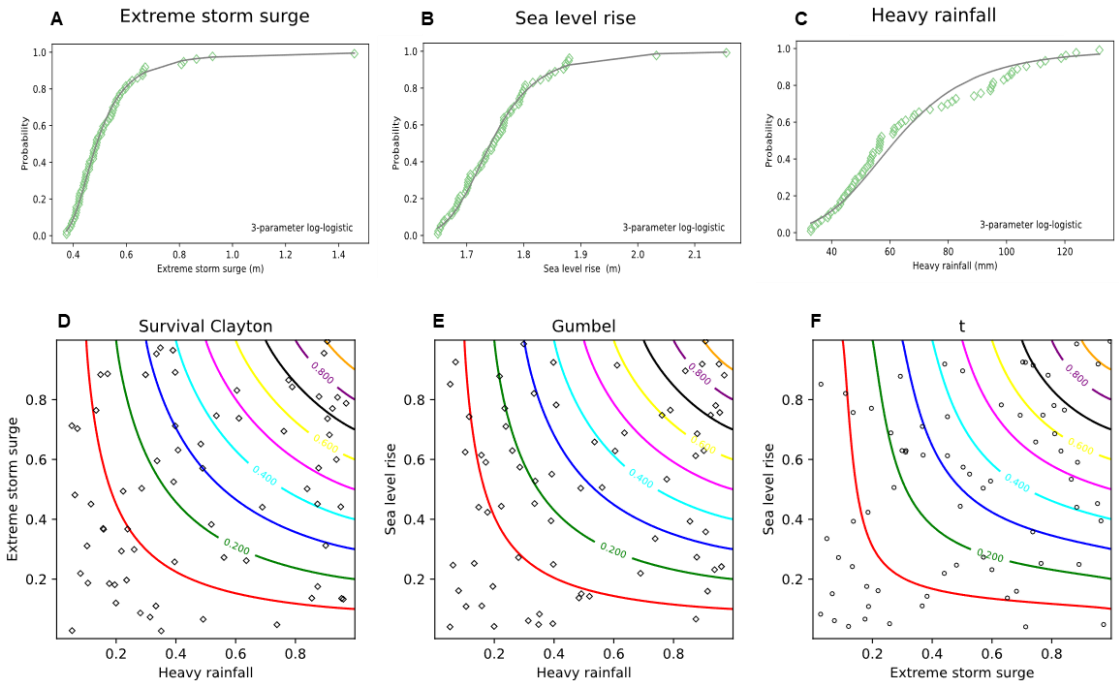

Figure 3.23 The use of copulas in examining the interrelationships among several factors including extreme storm surges, sea level rise, and heavy rainfall which collectively contribute to compound flooding in Hong Kong. Panels A, B, and C display the best-fitting marginal distributions for extreme storm surge, sea level rise, and heavy rainfall, respectively. Panels D, E, and F depict the bivariate copulas representing the interactions between these coastal flood drivers.

Using above the best-fitting marginal distributions, I conduct univariate analysis (only one flood driver exceeds its 95th percentile) and trivariate analysis (compound flood scenarios where storm surge, sea level rise, and heavy rainfall all surpass their respective 95th percentiles simultaneously). As shown in Figure 3.24, I compare return levels for heavy rainfall, extreme storm surges, and sea level rise across various return periods in both univariate and trivariate settings. In the case of heavy rainfall, under univariate conditions, return levels gradually increase from 49.25 mm for a 2-year period to 126.36 mm for a 100-year period. However, in trivariate scenarios, these levels escalate markedly, starting at 59.20 mm for 2 years and soaring to 261.16 mm for a 100-year return period, emphasizing the increased risk of extreme precipitation in compound flood situations. Similarly, for storm surges, the return levels in univariate analysis range from 0.41 m for a 2-year return period to 1.18 m for a 100-year return period. In trivariate scenarios, these figures rise, spanning from 0.49 m for a 2-year return period to 1.40 m for a 100-

year return period, showing a heightened risk of extreme storm surges during compound flood events. As for sea level rise, for univariate conditions, return levels vary from 1.68 m for a 2-year return period to 2.55 m for a 100-year return period. Conversely, trivariate analysis reveals slightly increased levels, from 1.74 m for a 2-year return period to 2.15 m for a 100-year return period, reflecting the intricate interactions in compound flood events.

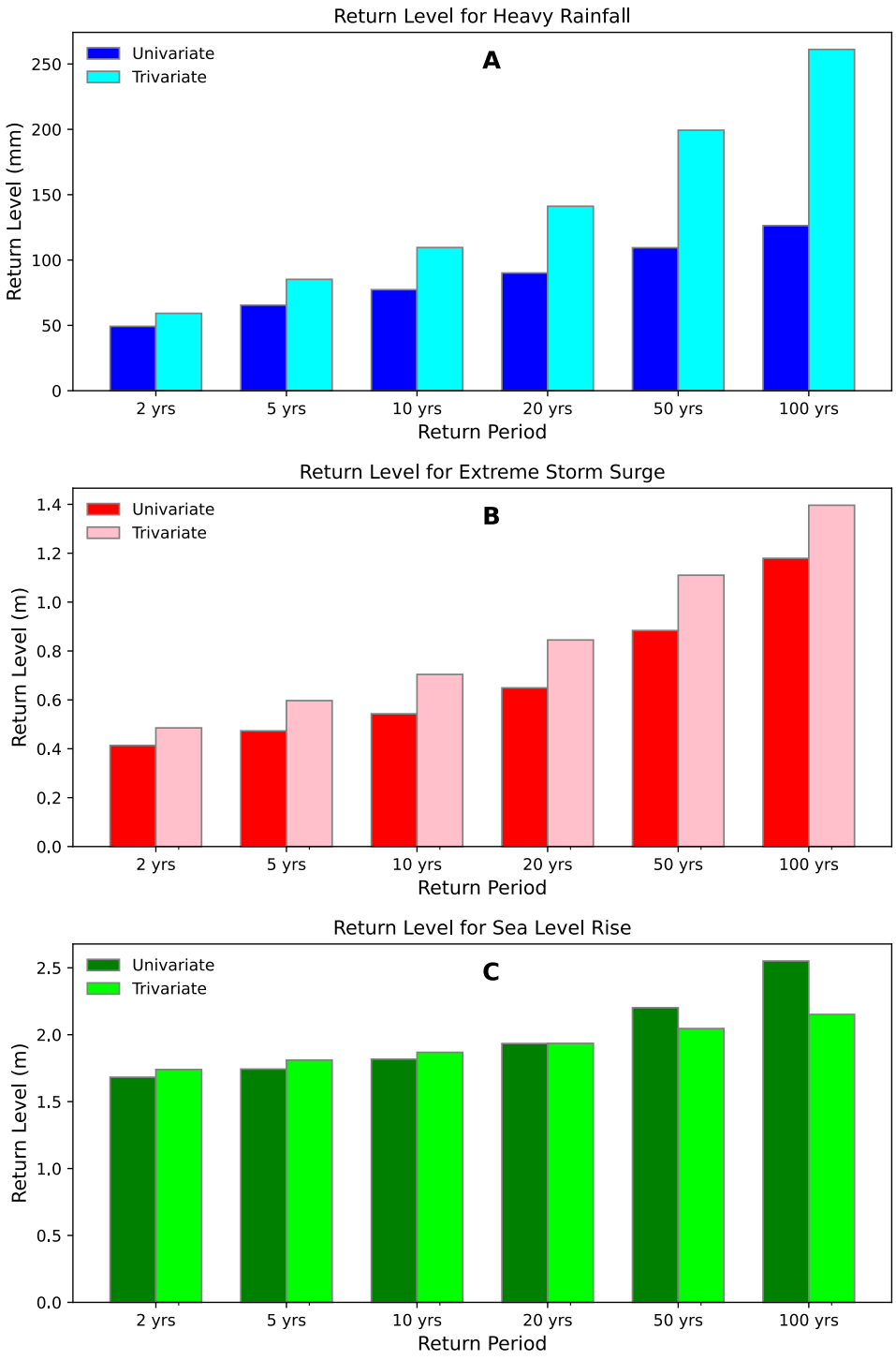

Figure 3.24 Comparison of return levels in univariate and trivariate flood scenarios. Panels A, B, and C display the return period of heavy rainfall, extreme storm surges and sea level rise, respectively.

3.3 Discussions and summary of the chapter

This chapter presented a novel approach to understanding and managing the escalating risks of coastal hazards, particularly storm surges and compound flooding, in China's coastal regions. Initially, the chapter focused on the development of a novel probabilistic framework for predicting storm surges. This part highlighted the validation of methodologies, specifically the vine copula ensemble approach and Bayesian Hierarchical Models, were employed to address the challenges of sparse data in estimating storm surge extremes. By leveraging data from adjacent tidal gauge stations, the BHM method surpasses the constraints of site-specific analyses, allowing for predictions in areas without direct data and thus expanding the understanding of flood risks in unmonitored coastal regions. This method provides a spatially consistent and time-continuous analysis, enhancing our understanding of compound flood hazards. The approaches developed here can be extended to other coastal areas for assessing compound flood risks, especially in regions with limited tidal gauge stations.

While the improvement in the vine copula ensemble model may be small in terms of mean correlation values of storm surge reconstruction, it offers several advantages over the RF, CNN, and LSTM models alone. The vine copula offers flexibility in selecting copula families, enhancing flexibility to diverse data distributions when evaluating the alignment of the RF, CNN, and LSTM models with observed data. The increased flexibility enhances the model's capability to capture the variability in storm surge reconstruction. Moreover, the comprehensive evaluation and integration of the RF, CNN, and LSTM models provides a more accurate quantification of uncertainty associated with storm surge predictions compared to relying on a single model. Addressing uncertainties is particularly critical for reliable predictions of storm surge due to the significant impact of moderate-to-large storm surge ranges on total water. Taking into consideration uncertainties helps to account for the potential variability in storm surge ranges and provide more reliable predictions of the actual water levels that coastal areas may experience. This capability allows decision-makers to accurately assess the risk associated with storm surges and make informed decisions on the implementation of sound mitigation measures.

The proposed BHM framework enables the spatially-continuous storm surge estimation, improving the traditional site-by-site analysis. One of its notable strengths lies in the ability to effectively address the limitation of data sparsity, which is the most common challenge to coastal storm surge hazard assessment and risk management. Unlike the traditional site-specific analysis that relies solely on data from individual tide gauges, the BHM effectively leverages information from nearby tide gauges, capturing the spatial dependencies inherent in storm surge events. This allows for storm surge predictions at ungauged locations, providing valuable insights even in the areas without direct observations. The BHM exhibits a remarkable accuracy in the estimation of GEV parameters and can reliably predict annual maximum storm surge heights at ungauged locations. Rigorous leave-one cross-validation method was used in this study to validate the predictive capability of BHM. This validation process systematically examines the BHM's ability to generalize to ungauged locations by excluding one gauge at a time and using the remaining data to estimate parameters and then predict storm surge heights. The consistent and accurate performance of the BHM across multiple cross-validation experiments reinforces confidence in its ability to make reliable predictions even in areas where observational data is sparse or unavailable. Moreover, the BHM can be used to provide a comprehensive and reliable assessment of uncertainties, enabling decision makers to have a deeper understanding of the variability and risk associated with storm surge events. For example, the BHM can generate the posterior distribution of estimated storm surge heights, including mean, lower- and upper-bound values, to capture the probabilities of different storm surge heights. The probabilistic prediction generated from the BHM approach offers valuable insights for establishing risk thresholds in decision-making processes, leading to better preparedness and protection against storm surge. Rather than relying solely on a single deterministic prediction, decision-makers can utilize the range of probabilistic predictions to determine risk thresholds with specific criteria. For example, by incorporating probabilistic prediction, decision-makers can use the 90^{th} percentile event as a reference point for making evacuation decisions, managing port operations, and determining the deployment of flood gates. By setting risk thresholds based on specific criteria and incorporating probabilistic prediction, the potential impacts of storm surge events can be more accurately assessed.

In addition to the BHM approach, there are several methods exist in previous studies for spatial interpolation and extreme value estimation, including Kriging (Krige, 1951), Inverse Distance Weighting (IDW) (Shepard, 1968), and Geographically Weighted Regression (GWR)

(Fotheringham et al., 2002). While Kriging is widely used for geostatistical interpolation, it often requires a large amount of data to accurately model the spatial correlation structure, therefore fall short in estimation accuracy in data-sparse regions than BHM. Similarly, IDW may have less reliable estimates in complex spatial patterns due to its lack of explicit spatial correlation representation. GWR extends traditional regression models by allowing the relationships between variables to vary over space. While GWR can capture local variations, it is deterministic and does not inherently provide probabilistic estimates, which are crucial for risk assessment and decision-making under uncertainty. In contrast, the BHM framework excels by offering a probabilistic approach that not only accounts for spatial correlations but also provides a comprehensive assessment of uncertainties. This probabilistic insight is particularly valuable for establishing risk thresholds and making informed decisions in coastal storm surge hazard management.

The chapter reveals the severity of storm surge along China's coastline throughout the period from 1979 to 2020. The estimated posterior mean of storm surge heights up to 1.29 m, which represents more severe and potentially hazardous surge conditions. Such heights can lead to more extensive flooding, damage to coastal structures, and pose risk to human life and property. The regions with higher vulnerability to storm surges, including Shanghai and Liaoning provinces, need to implement targeted risk mitigation strategies to enhance coastal resilience. The estimation of return periods further emphasizes the importance of planning for rare, yet extremely severe storm surge events. With a 100-year return period storm surge height reaching as high as 4.87 m, China’s coastal regions need to be prepared for such exceptionally intense events that could cause catastrophic damages and affect a large number of population. When high storm surge coincides with extreme precipitation and high tides under a warming climate, it can even lead to a compounded effect, causing deadly coastal flooding (Bevacqua et al., 2020; Fang et al., 2021; Jafarzadegan et al., 2023). To mitigate the risk associated with storm surges, urgent measures are needed for coastal communities and authorities. For example, implementing nature-based coastal protection solutions, such as preserving or restoring coastal vegetation like mangrove forests, can significantly reduce the height of storm surges by over 2 meters (De Dominicis et al., 2023).

The chapter on the analysis of compound flooding also reveals a statistically significant increase in extreme storm surge levels and mean sea levels, highlighting the growing impact of climate change on Hong Kong's coastal areas. The use of copulas demonstrated key

interdependencies among extreme weather phenomena, providing critical insights for managing the increasing risks of compound flooding in coastal urban environments. Moreover, the findings emphasize the significant threat posed by the simultaneous occurrence of extreme storm surges, sea level rise, and heavy rainfall. Notably, the trivariate analysis underscores the increased severity and risk in scenarios where all three flood drivers exceed their 95^{th} percentiles simultaneously. The rise in return levels for heavy rainfall and storm surges in these compound flood scenarios, compared to the univariate cases, points to a heightened risk of extreme weather events and their catastrophic impact on coastal urban areas.

Throughout the chapter, the importance of continuous and spatially detailed data for accurate hazard prediction and risk assessment was emphasized. The findings from both studies were not only academically significant but also vital for practical applications, providing essential insights for urban planners and policymakers in developing effective mitigation and adaptation strategies for coastal cities. These can serve as a vital resource for policymakers and urban planners, particularly in designing and implementing effective flood defense mechanisms and urban infrastructure resilient to compound flood events. The elevated return levels for rainfall and storm surges under trivariate conditions suggest the need for more robust flood defense systems that can withstand the compounded effects of these extreme events. This is crucial in preventing the catastrophic consequences that can result from such compound flood events.

Chapter 4. Identification and mechanisms of consecutive heat wave and heavy rainfall events

In addition to compound flood risk in coastal areas, this chapter then considers the threats posed by compound heat and flood hazards in inland areas. In this chapter, the consecutive heat wave and heavy rainfall (CHWHR) events are systematically assessed and analyzed. This type of temporally compound heat and flood events is newly identified, and the lagged connections between heatwaves and heavy rainfall in a changing climate have been further discussed, thereby adding to the evidence base for compound extreme events. Coincidence detection, attribution analysis, as well as climate projection methods are employed to investigate the probability of occurrence, underlying mechanisms, and future changes of CHWHR events in China. These findings provide insights for policymakers and stakeholders to better implement adaptation and mitigation solutions that can help reduce the negative impacts of these back-to-back extremes.

4.1 Probability of occurrence of historical CHWHR events

Figure 4.1 presents the probability of occurrence of historical CHWHR events within a prescribed temporal interval in China during 1981−2005, which represents the fraction of heat waves followed by heavy rainfall within 1 day, 3 days and 7 days. In general, 14% of land areas experience the CHWHR events (at the significance level of 0.05) within 1 day over China, which represents the worst-case scenario in which heavy rainfall occurs immediately 1 day after the end of heat waves, with an average 9% probability of occurrence of CHWHR events detected among all heat wave events (Figure 4.1a and b). When increasing the time interval to 3 days, the probability of occurrence is two times higher than those with a time interval of 1 day, with the probability of approximately 20% (Figure 4.1 c and d). In terms of the frequency of CHWHR events within 7 days (Figure 4.1e and f), the probability of occurrence increases to 26%, indicating that for every four heat wave events, there is one heavy rainfall event that occurs within 7 days after the end of a heat wave. Furthermore, I highlight that the observed high probability of occurrence of CHWHR events cannot be a pure coincidence by an additional random experiment, which is manifested in the cumulative distribution function subplots in Figure 4.1b, d and f.

In order to further check the significance and robustness of the detected probability of occurrence, I assess whether the CHWHR events occur more often than expected by chance by a random coincidence experiment simulated by 1,000 times of bootstrap iteration. Specifically, the grid-level frequencies of heat wave and heavy rainfall events were pooled and randomly sampled respectively over 1981−2005 using observational data. The probability of occurrence of CHWHR events was then calculated using the event coincidence analysis (ECA) framework. This random coincidence experiment was performed 1,000 times to model the probability of occurrence expected by chance. I then compare the observed probability of occurrence and that expected from the random coincidence experiment alone. As shown in Figure 4.1f, the probability of occurrence of CHWHR events in observation (red line) is much higher than that expected due to random coincidence (i.e., expected by chance) (grey line and hatched curve). For heat wave events being followed by heavy rainfall events within 7 days, the averaged probability of occurrence is 26% (in observation) vs 10% (expected by chance, 95% confidence interval: 5% ~ 16%), indicating that the above detected signals are much higher than those expected due to random coincidence.

The probability of occurrence of CHWHR events shows spatial hotspots and regional variability across different climate regions in China (Figure 4.1). There is a relatively high probability of occurrence of CHWHR events within 1 day during 1981−2005 (approximately 31%) located in Central and Southwest China, indicating that for every three heat wave events, one of which is followed by heavy rainfall (CHWHR events) with a 1-day lag. When longer time intervals are considered, there are significantly increasing trends in the probability of occurrence of CHWHR events within 3 days and 7 days.

The findings are consistent with observational evidence from previous studies of heat waves and heavy rainfall patterns (Deng et al., 2020; Sun et al., 2017; Tao & Ding, 1981; Chang et al., 2012). For instance, the hotspots detected over Central and Southwest China (around the Qinghai-Tibet Plateau) are related to the relatively high summer temperature and an abrupt increase in precipitation may be due to the sudden change of summer rain-bearing synoptic systems and orographic effects. These patterns are consistent with previous findings of the increasing magnitude and frequency of heat waves (Deng et al., 2020; Sun et al., 2017) as well as heavy rainfall and severe storms over the plateau and its surroundings in Central and Southwest China (Tao & Ding, 1981). The frequent occurrence of CHWHR events in Southwest China, especially

in mountainous areas, can be explained by a combination of climatic and geographical factors (Houze, 2012; Li et al., 2012; Wang et al., 2013). The orographic effects prominent in these regions significantly influence atmospheric convection and moisture convergence. Mountains aid in the elevation of moist air masses, which can result in increased precipitation. This process often leads to heavy rainfall following heat waves. The scattered patterns found in part of Northeast China may be associated with the combined effects of mid-latitude anticyclones and the western Pacific subtropical high (WPSH). The former relates to blocking weather patterns and typically leads to the occurrence of heat waves (Li et al., 2019; Petoukhov et al., 2013). The WPSH could cause the northward jump of subtropical high in summer, during which the monsoon may reach the northeast (Chang et al., 2012), transporting a great amount of moisture and thus setting a prerequisite for the occurrence of heavy rainfall after the end of heat waves.

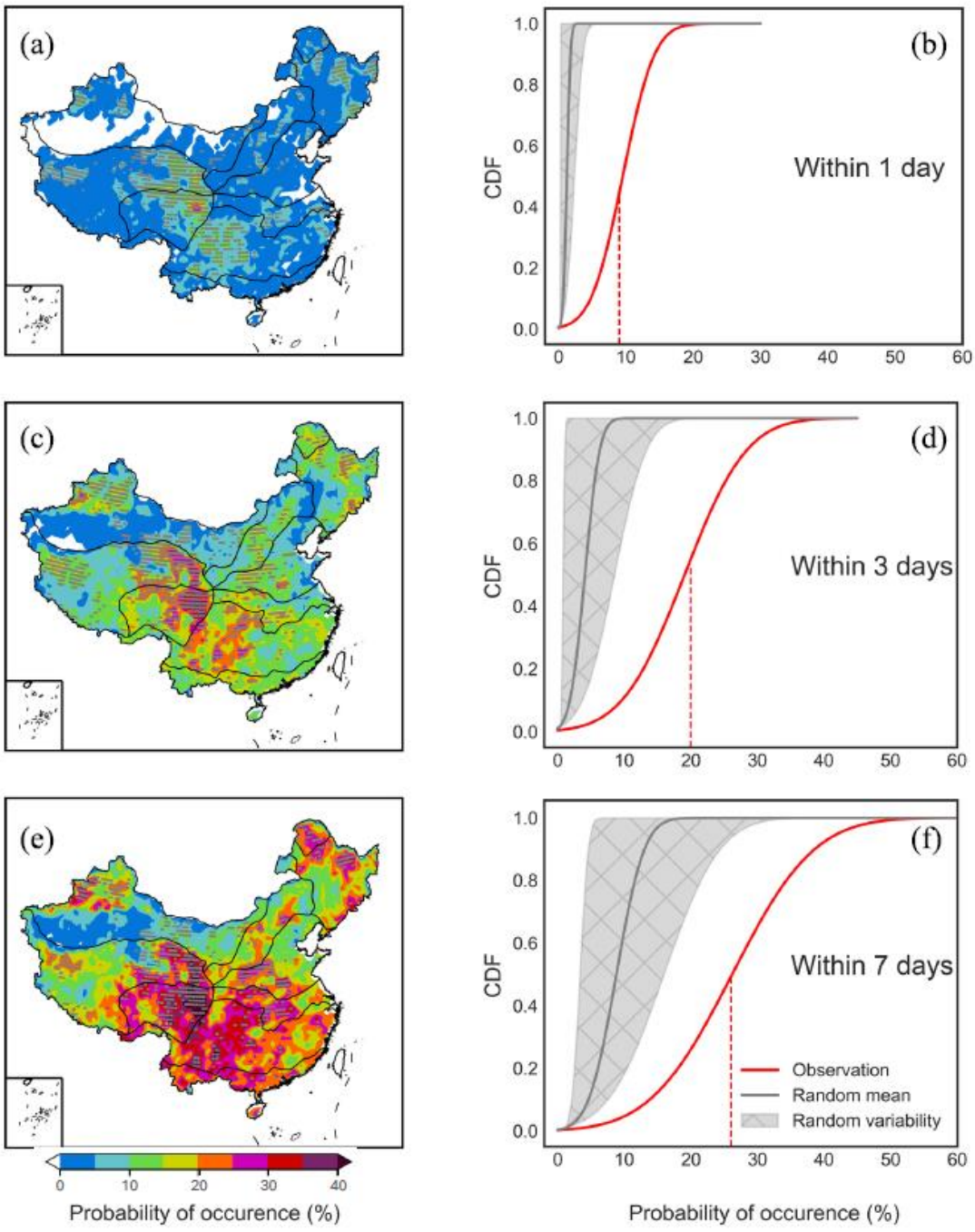

Figure 4.1 The spatial distribution (left column) and corresponding cumulative distribution function (CDF) (right column) of the probability of occurrence of consecutive heat wave and heavy rainfall (CHWHR) events within the prescribed temporal intervals (1 day, 3 days and 7 days), indicating the fraction of heat wave events being followed by heavy rainfall within 1 day (a, b), 3 days (c, d) and 7 days (e, f). The CDF plots in the right column show observed probability of

occurrence CHWHR events (red) versus those expected by chance (grey), and its 95% confidence interval of random variability simulated by 1,000 times of bootstrap iteration (grey and hatched). Only statistically significant areas at the 0.05 level are hatched on maps and are considered in the CDF. The datasets used here are observational data for the period 1981−2005.

4.2 Comparison between heat waves followed by and not followed by heavy rainfall

I examine the differences between characteristics of heat waves followed by heavy rainfall (i.e., CHWHR events) and those not followed by heavy rainfall within 1 day. There is a statistically significant difference in heat wave duration (HWD) and heat wave magnitude (HWM) between the abovementioned two types of events. In general, the shorter and hotter heat waves are more likely to be followed by heavy rainfall compared with those not followed by heavy rainfall (Figure 4.2). For the regions where the CHWHR events occurred during 1981−2005, a great proportion of regions (approximately 95% of total land areas) experienced the longest heat waves lasting less than 10 days (Figure 4.2a). For the areas without the occurrence of CHWHR events, however, heat waves tend to last for a relatively long time. Specifically, approximately 70% of land areas experienced longer heat waves for non-CHWHR events, with the duration of more than 10 days (Figure 4.2c). These findings are also manifested in the CDF of HWD (Figure 4.2e), as a clear shift to the left of the distribution of CHWHR events (red line) compared to those of heat waves not followed by heavy rainfall (green line). On the other hand, the HWM of CHWHR events, representing heat wave intensity, is generally higher than those heat waves not followed by heavy rainfall, with the largest anomalies located in northern China (Figure 4.2b and d). Unlike the HWD of CHWHR events which becomes shorter significantly, the HWM of CHWHR events is not always higher than those not followed by heavy rainfall over China, especially for mild heat waves. In this study, I focus on the statistically significant areas with relatively high intensity (exceed average anomalies of 3 °C) in Figure 4.2b and f, which indicate increased excess heat accumulated during the CHWHR events. In other words, the higher HWM of CHWHR events is observed with the upper tail of the CDF shifted to the right, which demonstrates that the hotter heat waves are more likely to be followed by heavy rainfall (CHWHR events) compared with those not followed by heavy rainfall.

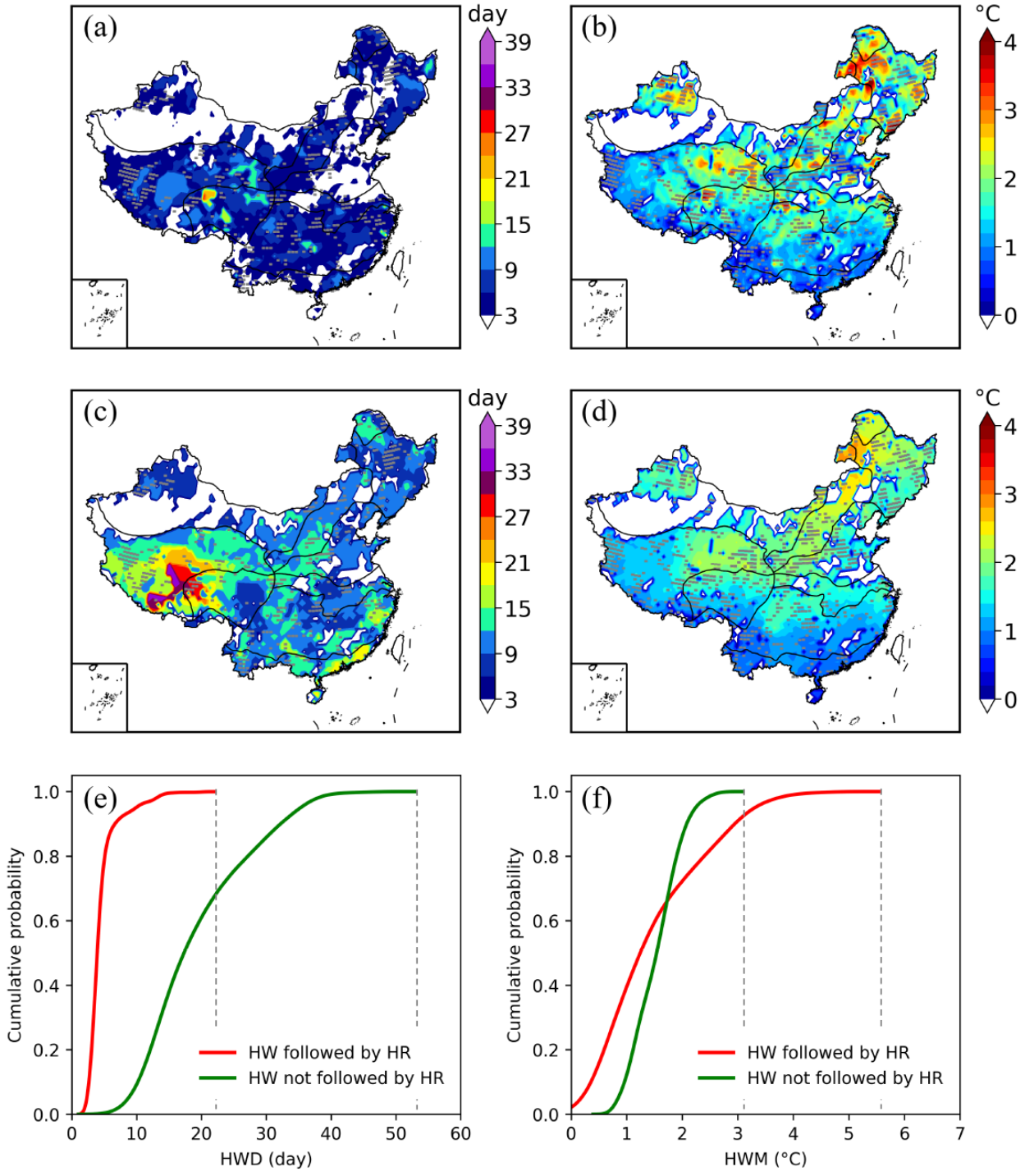

Figure 4.2 Comparison of heat wave duration (HWD, day) (left column) and heat wave magnitude (HWM, degree Celsius) (right column) between heat waves followed by and not followed by heavy rainfall: (a) HWD for those followed by heavy rainfall (i.e., CHWHR events); (b) HWM for those followed by heavy rainfall; (c) HWD for those not followed by heavy rainfall; (d) HWM for those

not followed by heavy rainfall; (e) CDF of the HWD for heat waves followed by (red) and not followed by heavy rainfall (green); (f) CDF of HWM for heat waves followed by (red) and not followed by heavy rainfall (green). Hatched areas are statistically significant at the 0.05 level, representing the regions where the differences of HWD or HWM between heat waves followed by and not followed by heavy rainfall are significant.

4.3 Physical mechanisms behind CHWHR events

To further investigate synoptic preconditions when heavy precipitation occurs after heat waves in close succession, I evaluate atmospheric variables of convective available potential energy (CAPE), the convective inhibition (CIN) and vertically integrated moisture divergence (VIMD) anomalies between heat waves followed by and not followed by heavy rainfall, with a focus on the conditions 1 day prior to the date of the occurrence of heavy rainfall following heat waves (Figure 4.3). As a crucial indicator of atmospheric instability, the CAPE appears to be relatively high in the northern and western parts of China (Figure 4.3a), which could potentially promote the development of convection and stormy weather (Wallace, 1975; Brooks et al., 1994; Seeley & Romps, 2015). CIN is another measurement of the amount of energy required for stormy weather and if CIN is too high, moist convection is unlikely to occur even though CAPE is high (Chen et al., 2020b). This is manifested in the red box located in central China (Figure 4.3b and 3d) where heavy rainfall does not occur after heat waves since the higher CAPE is witnessed but the CIN is larger. The high CAPE combined with the low CIN provides favorable conditions for stormy weather, and thus can lead to the sequential occurrence of heavy rainfall after the end of heat waves. I find that statistically significant differences (with the significance level of 0.05, as shown by hatched areas in Figure 4.3) in both CAPE and CIN exist between heat waves followed by heavy rainfall (CHWHR events) and those not followed by heavy rainfall, indicating that CAPE and CIN play an important role in the sequential occurrence of heavy rainfall within 1 day after the end of heat waves in China. With regard to the VIMD, the negative value of VIMD derived from ERA5 indicates that moisture is converging, and for better visualization, I transform the VIMD value from negative to positive. The larger values, as shown in the color bars of Figure 4.3 e and f, suggest that more moisture is converging, which is conducive to the occurrence of heavy rainfall when the rainfall is preceded by a heat wave event. As shown in Figure 4.3e and f, there is a statistically significant difference in the VIMD anomalies between heat waves followed by

and not followed by heavy rainfall, with increasing VIMD-derived water vapor convergence during the CHWHR events over China (Zhou & Yu, 2005). Based on previous studies assessing the importance of CAPE, CIN and VIMD on heavy precipitation, the findings highlight that the large-scale climate drivers of CAPE, CIN and VIMD anomalies play an important role in the successive occurrence of heat waves and heavy rainfall in China (CHWHR events).

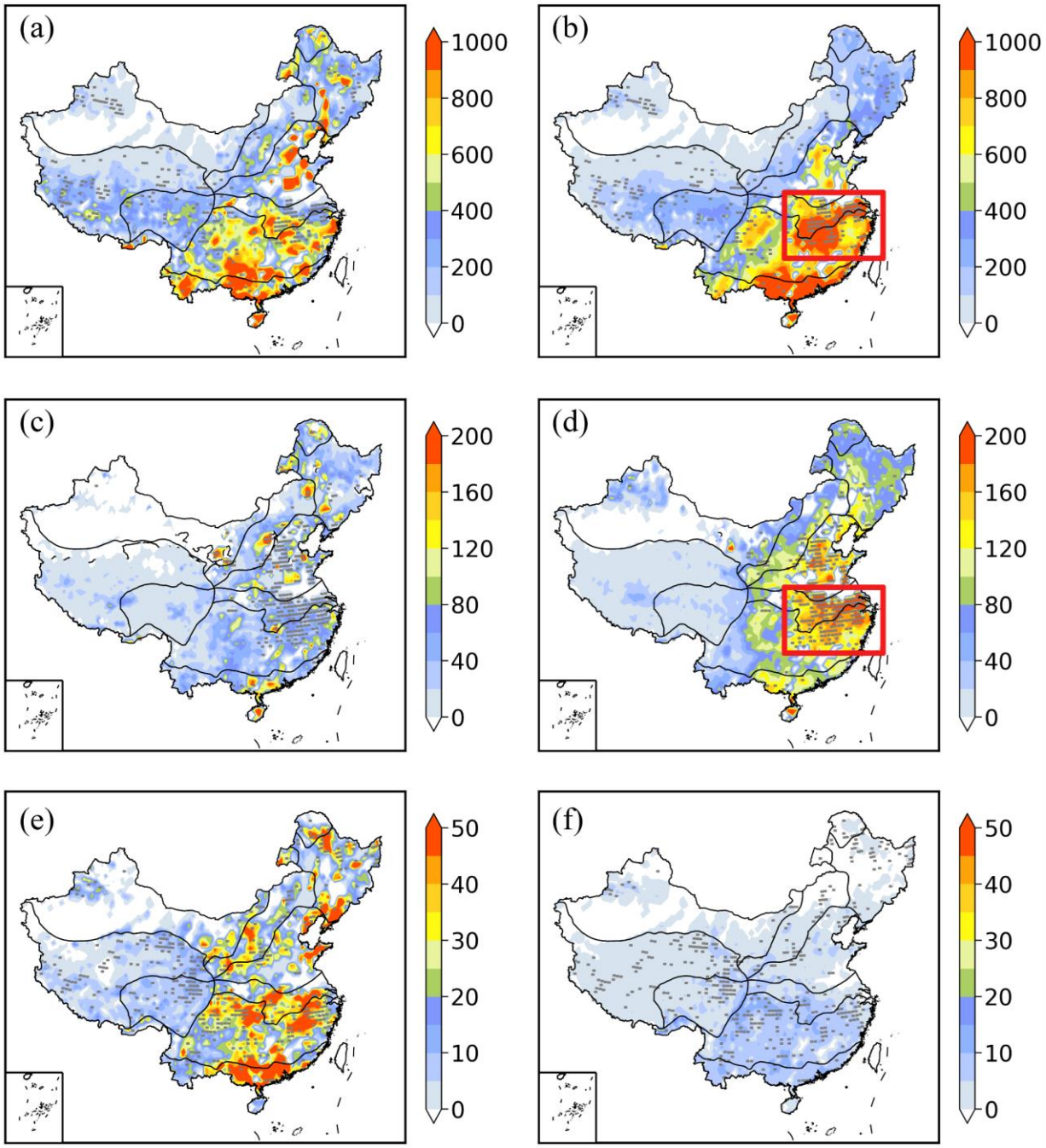

Figure 4.3 Distributions of three convection-related atmospheric variables: the convective available potential energy (CAPE, J/kg) (top row), convective inhibition (CIN, J/kg) (middle row), and the vertically integrated moisture divergence (VIMD, kg/m^2) (bottom row). (a, c, e) represent heat waves followed by heavy rainfall and (b, d, f) represent heat waves not followed by heavy rainfall. Hatched areas are statistically significant at the 0.05 level.

4.4 Projection of future changes of CHWHR events

Figure 4.4 presents the distributions of the risk ratios of CHWHR events relative to the historical period within the prescribed time intervals of 1 day, 3 days and 7 days using CORDEX-CORE models . The risk ratio is defined as the ratio of frequencies of CHWHR events over a future 25-year period (2075–2099) to those in the historical 25-year period (1981–2005). In general, there is an increasing trend in the frequency of occurrence of CHWHR events by the end of the 21st century, with the risk ratio increasing significantly by a factor of 1–5 over most regions of China. Figure 4.4a, b and c indicate that the land areas of increased CHWHR frequencies (i.e., risk ratios higher than 1) decrease when the time intervals extend from 1 day to 3 days and then to 7 days, with a decreasing land proportion of 15%, 37% and 31%, respectively (growing blue areas in Figure 4.4). This indicates that in the future, more CHWHR events will occur with the most rapid transition (from heat wave to heavy rainfall within only 1 day), which is largely attributed to a warming climate under the high-emission scenario. This projected trend is also observed by the corresponding cumulative probability of risk ratios of CHWHR events, as shown in Figure 4.4d, indicating that more heat waves are expected to be followed by heavy rainfall for the future period 2075–2099 relative to 1981–2005, especially for the worst-case scenario when heavy rainfall occurs abruptly one day after the end of heat waves.

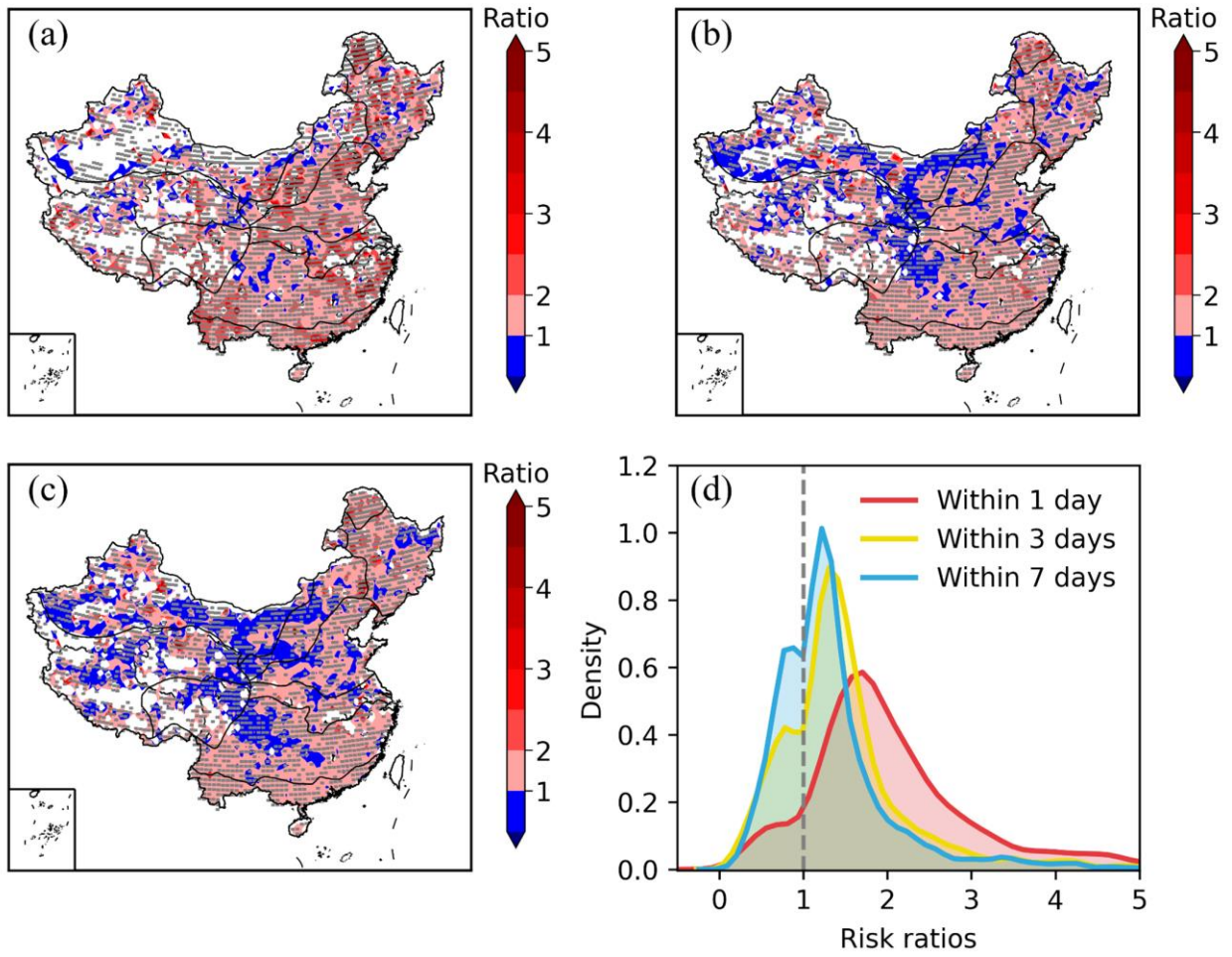

Figure 4.4 Projected future changes in the risk ratios of CHWHR events relative to the historical period: (a) heat wave events being followed by heavy rainfall within 1 day; (b) within 3 days; (c) within 7 days; (d) density plot of grid cell distributions in the risk ratios of CHWHR events within 1, 3 and 7 days. Hatched areas are statistically significant for all three models.

4.5 Verification, sensitivity analysis and discussions of CHWHR events

4.5.1 Historical reproduction of CHWHR events

To project future changes in the risk ratios of CHWHR events relative to the historical period based on the CORDEX-CORE models, historical CHWHR events were reproduced using three CORDEX-CORE models including MOHC-HadGEM2-ES, MPI-M-MPI-ESM-LR and NCC-NorESM1-M. Those three available CORDEX CORE models were also used to address model structural uncertainty and then were validated by comparing model outputs against observations.

Only the results of all three models that show good agreement were chosen for calculating the ensemble mean of the future changes in the risk ratios of CHWHR events. I use the same predefined thresholds for both the past and future periods to make it comparable when projecting the future changes of the frequency of CHWHR events. Generally, there is good agreement between model simulation and observation in terms of the probability of occurrence of CHWHR events (Figure 4.5), indicating the skill of CORDEX-CORE models for capturing the characteristics of CHWHR events.

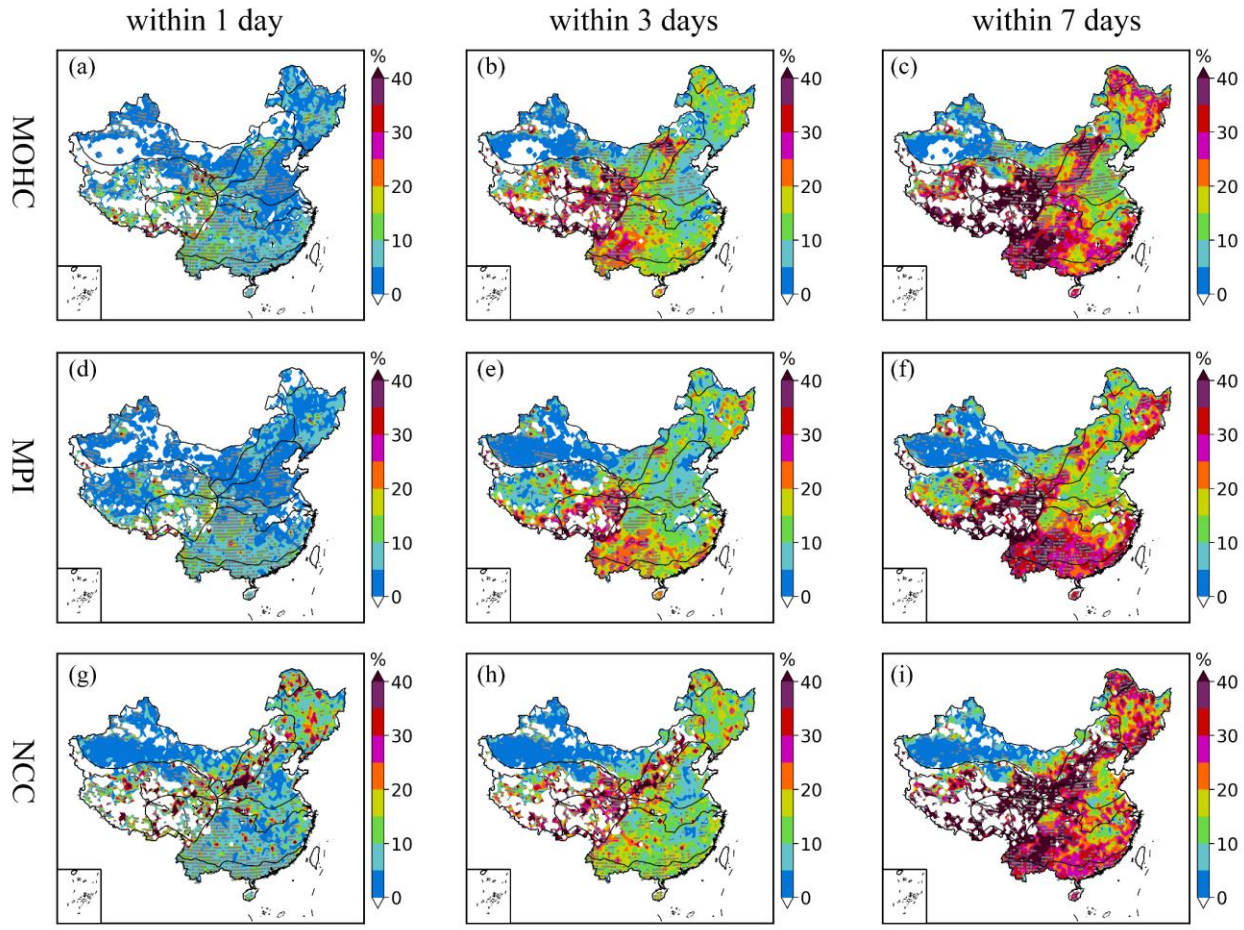

Figure 4.5 The probability of occurrence of consecutive heat wave and heavy rainfall (CHWHR) events within 1 day (left column), 3 days (middle column), and 7 days (right column) for the period 1981−2005, using three CORDEX-CORE models: MOHC-HadGEM2-ES model (top row), MPI-M-MPI-ESM-LR model (middle row), and NCC-NorESM1-M model (bottom row). Hatched areas are statistically significant at the 0.05 level.

4.5.2 Verification of findings using different datasets and thresholds

I verify the probability of occurrence of CHWHR events during the historical period based on the integration of daily maximum temperature and precipitation using different datasets from the ERA5 reanalysis product and three CORDEX-CORE models including MOHC-HadGEM2-ES, MPI-M-MPI-ESM-LR and NCC-NorESM1-M. As shown in Figure 4.5 and Figure 4.6, the spatial patterns are similar among observations, the reanalysis product, and models for the historical period 1981−2005, indicating that the findings are robust and consistent regardless of data sources. It should be noted that the small hotspots in central China are underestimated in ERA5, and regional models compared to observations. In addition, the probability of occurrence and the associated significance level of CHWHR events are sensitive to the definition of extreme events by percentile-based thresholds (He & Sheffield, 2020).

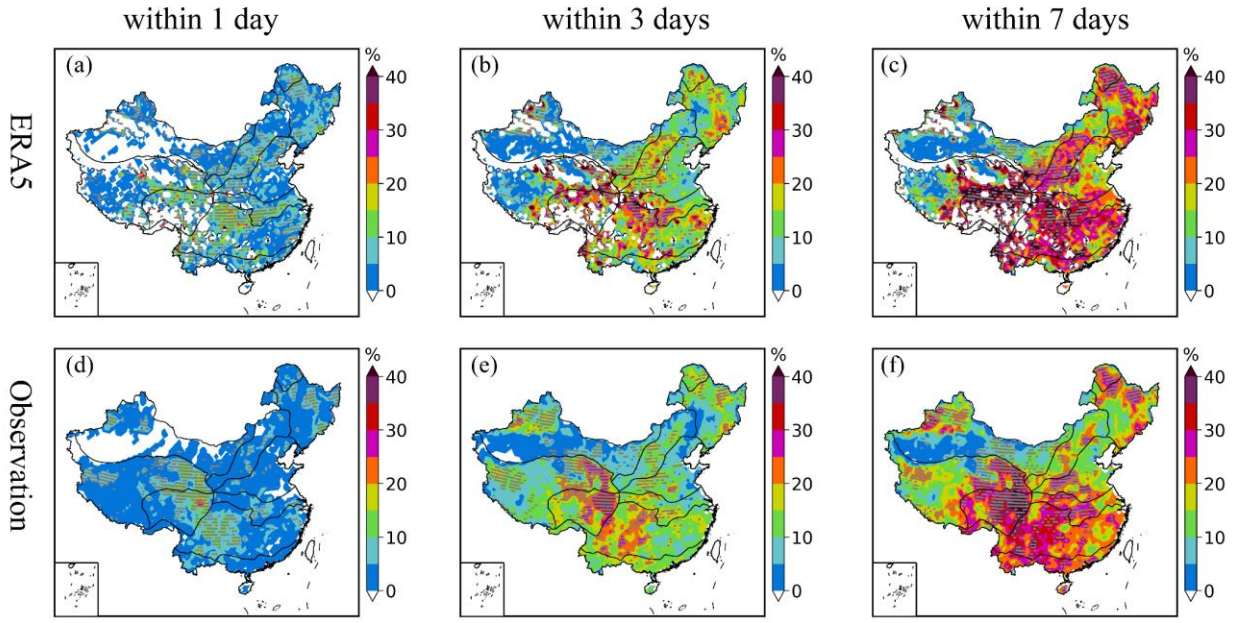

Figure 4.6 The probability of occurrence of consecutive heat wave and heavy rainfall (CHWHR) events within 1 day (left column), 3 days (middle column), and 7 days (right column) for the period 1981−2005, derived from the ERA5 reanalysis product (top row) and observational data (bottom row). Hatched areas are statistically significant at the 0.05 level.

To perform sensitivity analysis of percentile-based thresholds, I also define the extreme rainfall events as the top 1% of all rainfall events (above the 99th percentile threshold). As expected,

the higher threshold can largely reduce the number of CHWHR events, and thus the average probability of occurrence of CHWHR events decreases to only 4%, 8% and 10% within 1, 3 and 7 days, respectively (Figure 4.7).

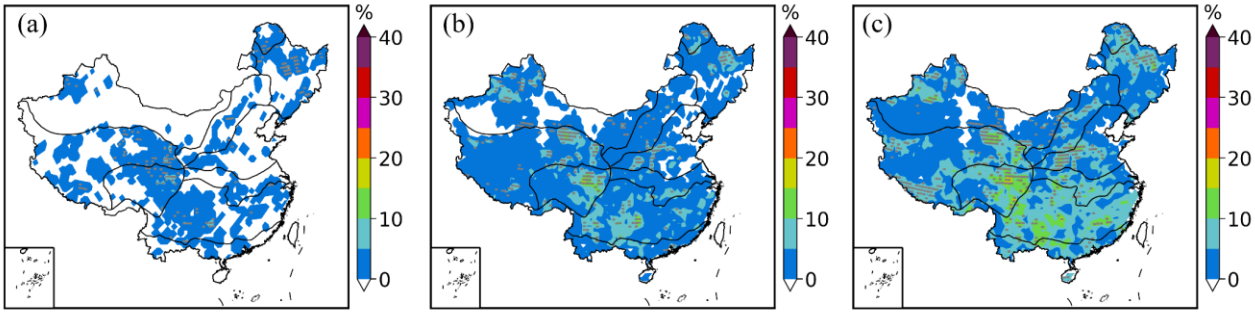

Figure 4.7 The probability of occurrence of consecutive heat wave and extreme rainfall (higher than the 99th percentile of precipitation) within 1 day (left column), 3 days (middle column), and 7 days (right column) using observational data for the period 1981–2005. Hatched areas are statistically significant at the 0.05 level.

4.5.3 Sensitivity analysis of HW-HR-HW events

It may be possible that the identification of CHWHR events is affected by the consecutive occurrence of heat wave, heavy rainfall and another heat wave event (HW-HR-HW). Specifically, the CHWHR event may not be essentially the same as the long-duration heat waves but interrupted by a day or two of rain that briefly drops the temperatures. In this case, I have investigated the possibility of these sequential events and as shown in Figure 4.8, the frequency of HW-HR-HW events is extremely low and it is most likely to be a random coincidence, indicating that a day of heavy rain occurs during two successive heat waves makes a negligible difference. To further address the interference effect of heavy rain on the key findings, I have categorized the abovementioned consecutive two heat wave events separated by 1 day (HW-HW) into one and have re-examined the differences between characteristics of heat waves followed by heavy rainfall and those not followed by heavy rainfall. As shown in Figure 4.9, the patterns are very similar to Figure 4.2 in the paper, although the duration of heat wave is slightly higher than those in Figure 4.2e due to the clustering of two successive and connected heat wave events. This indicates that the findings that shorter and hotter heat waves are more likely to be followed by heavy rainfall are

robust and are not sensitive to the occurrence of a day or two of heavy rain that briefly drops the temperatures.

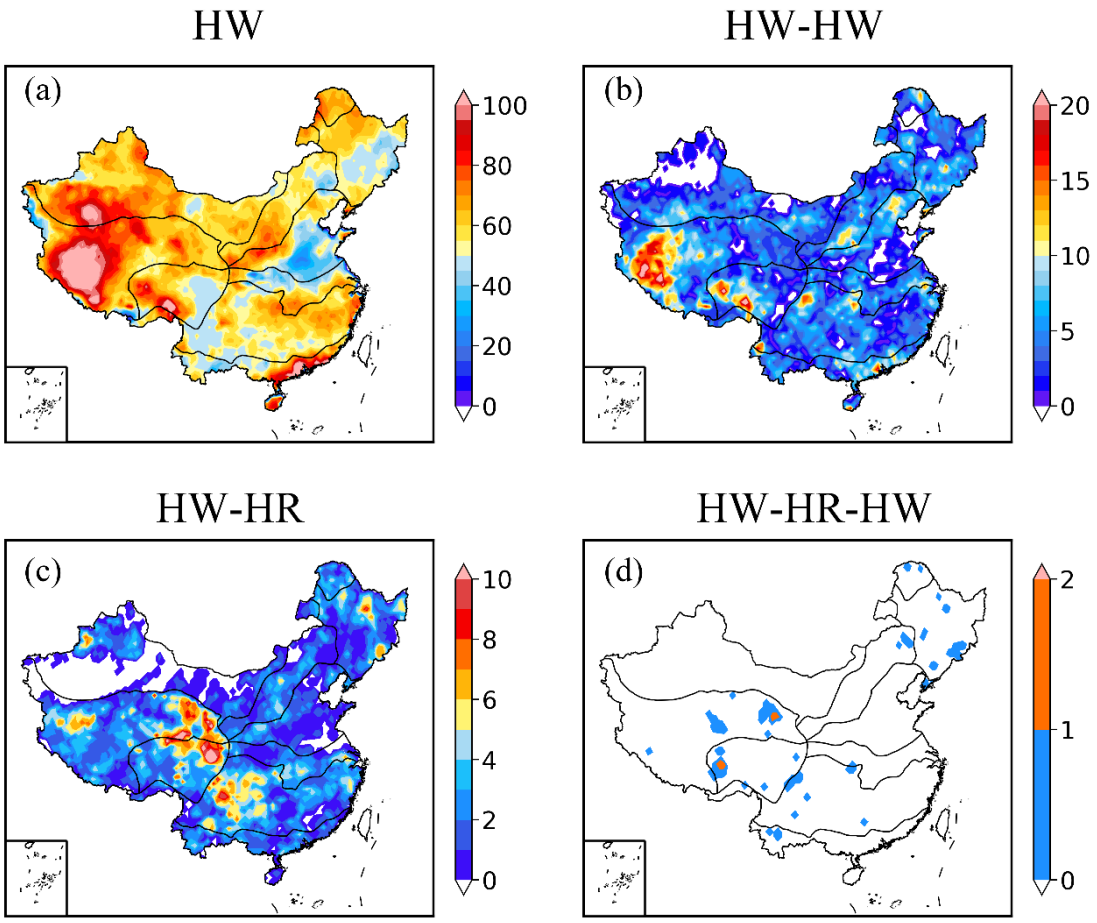

Figure 4.8 The frequencies (event numbers) among all heat waves (HW) (a), consecutive two heat wave events separated by 1 day (HW-HW) (b), consecutive heat wave and heavy rainfall (HW-HR) (c) and consecutive heat wave, heavy rainfall and another heat wave (HW-HR-HW) (d) within 1 day using observational data in China during 1981−2005.

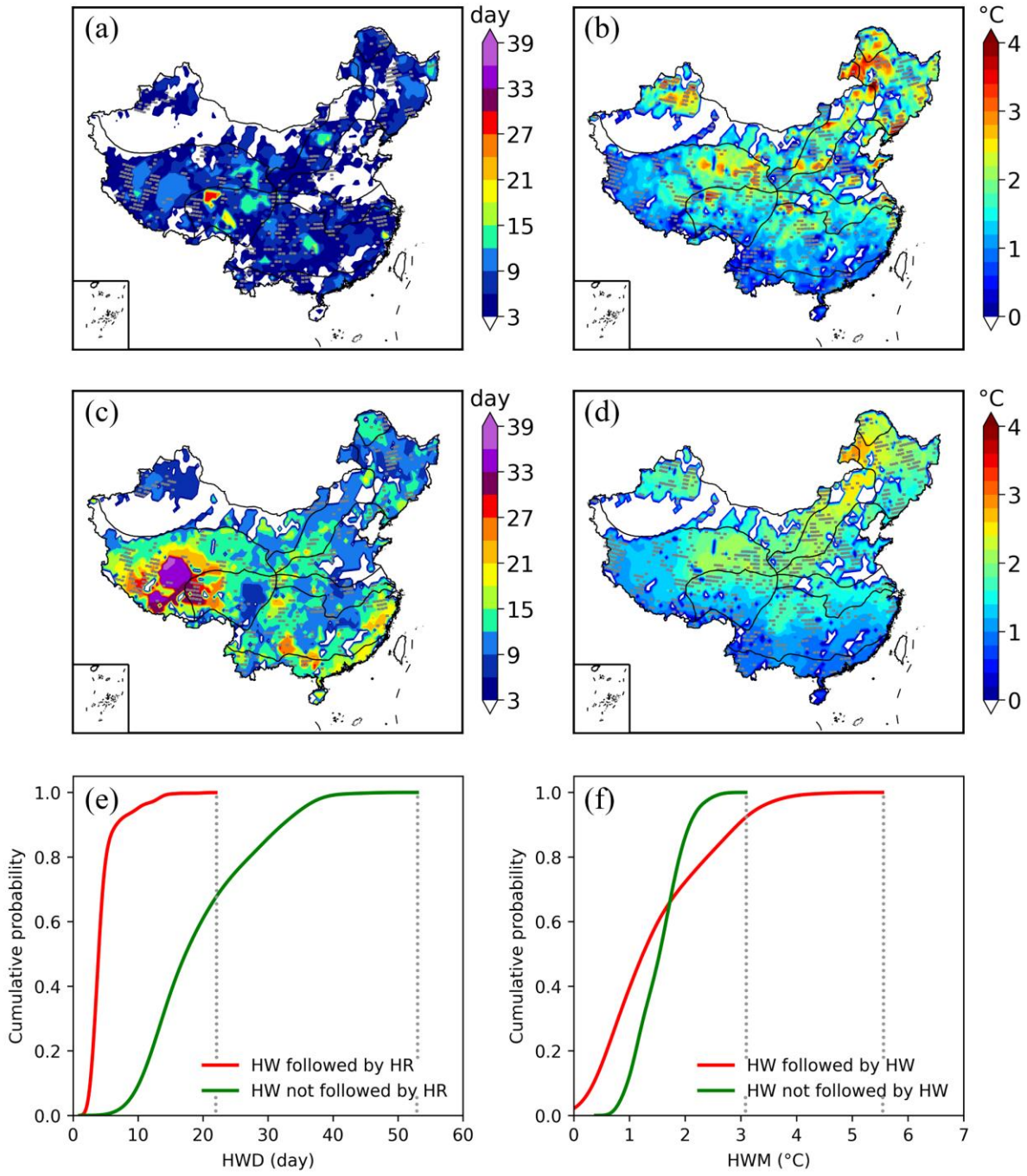

Figure 4.9 Sensitivity analysis results. Comparison of heat wave duration (HWD, day) (left column) and heat wave magnitude (HWM, degree Celsius) (right column) between heat waves followed by and not followed by heavy rainfall: (a) HWD for those followed by heavy rainfall (i.e., CHWHR events); (b) HWM for those followed by heavy rainfall; (c) HWD for those not followed by heavy rainfall; (d) HWM for those not followed by heavy rainfall; (e) cumulative distribution function

(CDF) of the HWD for heat waves followed by (red) and not followed by heavy rainfall (green); (f) CDF of HWM for heat waves followed by (red) and not followed by heavy rainfall (green).

4.5.4 Verification of latent correlation between HWD and HWM

Considering the possibility that the shorter heat waves could tend to be hotter simply because of accumulation over fewer days, I conduct correlation analysis to examine whether there is a latent correlation between heat wave duration (HWD) and heat wave magnitude (HWM). As shown in Figure 4.10, I find the R^2 value is 0.01, indicating no latent relationship between HWD and HWM, which further confirms the robustness of the findings. Hotter heat waves are associated with larger sensible heat flux, while the shorter-duration heat wave may be tied to abrupt water vapor convergence that can stop the persistence of oppressive heat waves. The larger heat forcing combined with abrupt moist accumulation, caused by the shorter and hotter heat waves, may contribute to atmospheric instability and trigger convection for precipitable water. These may help explain why the shorter and hotter heat waves are more likely to be followed by heavy rainfall compared with those not followed by heavy rainfall.

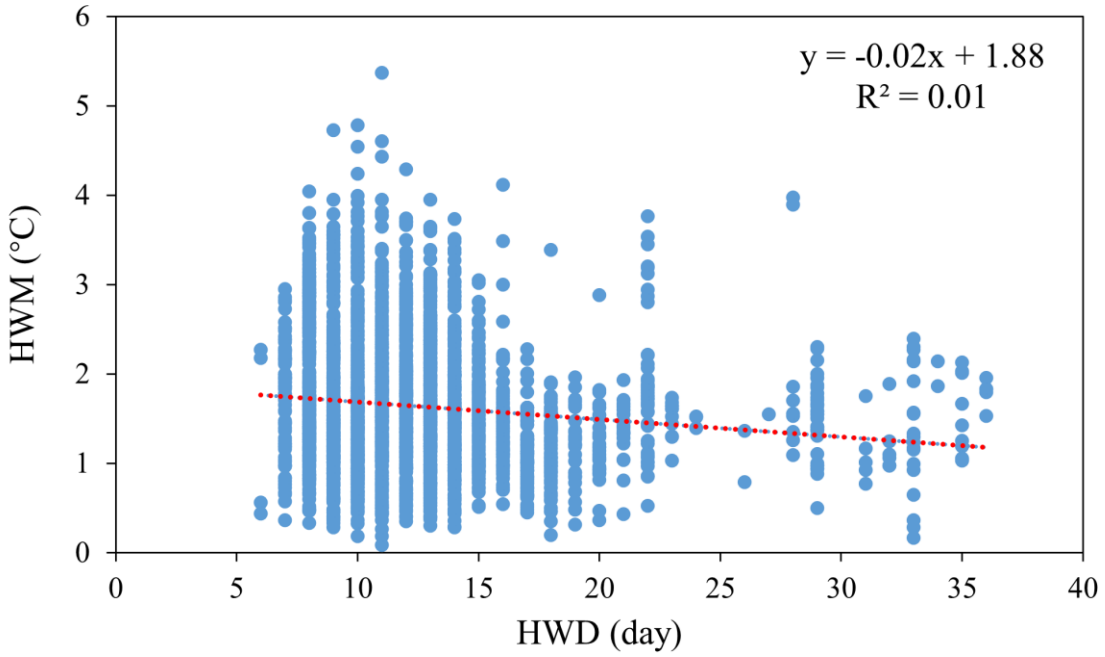

Figure 4.10 Scatter plot of heat wave duration (HWD) and heat wave magnitude (HWM).

4.5.5 Analysis of trends of CHWHR events in recent decades

In the section mentioned above, my research encompasses an analysis spanning from 1981 to 2005 to study historical climate patterns, and from 2075 to 2099 to predict future scenarios under high-emission conditions. This comparison is aimed at understanding the impacts of climate change. Additionally, I have broadened the scope to include an investigation into the recent trends regarding the probability of occurrence of CHWHR events from 1981 to 2022. As shown in Figure 4.11, there has been a statistically significant rise in the probability of these events CHWHR occurring, as demonstrated by a linear trend with a slope of 5.04% per decade during 1981–2022. This trend indicates a significant and ongoing increase in the frequency of CHWHR events within the study period.

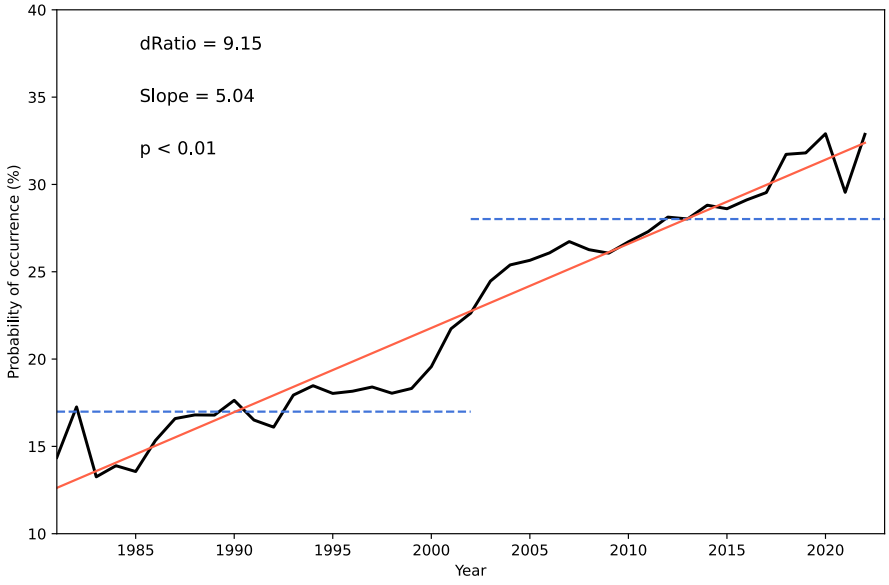

Figure 4.11 Annual time series of the probability of occurrence of CHWHR events. Black line is the probability of occurrence (%) based on observation data. A 10-year moving window was used to smooth the data. Blue dashed line is the 21-year average. dRatio is the difference between the averages during 1981–2001 and 2002–2022. Red line represents the linear trend. Slope is the linear trend using the Sen-slope method (unit, decade).

4.6 Discussions and summary of the chapter

Previous studies have examined heat waves and heavy rainfall events separately, yet their compound characteristics and future projections have not been investigated systematically. This chapter presents new evidence on a temporally compounding extreme in China, namely the consecutive heat wave and heavy rainfall (CHWHR). By coincidence detection and attribution analysis as well as climate projection, I reveal the probability of occurrence, underlying mechanisms, and future changes of CHWHR events. Although this chapter is focused on China, the proposed framework can also be applied to examine the occurrence of CHWHR events elsewhere around the world where reliable datasets with long-term records of temperature and precipitation are available.

The findings indicate that approximately for every four heat wave events, there is one subsequent heavy rainfall (CHWHR event) within 7 days during 1981–2005. Furthermore, I find that the shorter and hotter heat waves are more likely to be followed by heavy rainfall compared with those not followed by. Such a new phenomenon is associated with three potential factors including CAPE, CIN, and VIMD that play vital roles in providing the favorable prerequisite for heavy rains and severe storms after heat waves, thereby resulting in the abrupt transition from heat waves to heavy downpours (or floods). In addition, CHWHR events are projected to occur more frequently and abruptly in China by the end of this century, increasing the risk of consecutive heat waves and floods as the climate warms.

I verify that the findings are robust and consistent regardless of data sources, through the use of different datasets from the ERA5 reanalysis product and three CORDEX-CORE models including MOHC-HadGEM2-ES, MPI-M-MPI-ESM-LR and NCC-NorESM1-M. The spatial patterns of the probability of occurrence of CHWHR events are generally consistent for the historical period 1981−2005, despite some small hotspots in observations are not well captured by ERA5 and regional models. I have also investigated the possibility that a heat wave event may be temporally interrupted by a day or two of heavy rain and subsequently followed by another heat wave, which may interfere with the identification and significance of CHWHR events. Sensitivity analysis shows that the frequency of consecutive heat wave, heavy rainfall and another heat wave events turns out to be extremely low and the findings that shorter and hotter heat waves are more

likely to be followed by heavy rainfall are not sensitive to the occurrence of a day or two of heavy rain that briefly drops the temperatures.

This chapter offers practical implications for policymakers and stakeholders adopting to mitigate the double threat of the abrupt transition from lethal heat waves to catastrophic downpours. This is especially important for the early warning and forecasting of compound extremes and flash floods (Boschat et al., 2015; Lau & Kim, 2012; Wasko, 2021), so that the society will be able to quickly respond to and prepare for the potential risk of a subsequent heavy rainfall hazard when a short-duration but high-intensity heat wave is witnessed.

Chapter 5. Identification and mechanisms of successive heat-pluvial and pluvial-heat events

Compared with the previous section on nationwide CHWHR events, this part of the research extends the scope to the global scale, refining methodologies and further discussing the compound heat and flood hazards. To better characterize compound events, a more comprehensive indicator, humid heat, is used instead of traditional methods of measuring heat waves, allowing for an accurate assessment of human discomfort and health risks. A pluvial flood index is employed for a more complete description of the flood potential than heavy rainfall alone. To develop an in-depth understanding of the abrupt shift from humid heat and pluvial flood events and vice versa, this chapter presents a comprehensive global analysis of changes in the frequency of temporally compounding humid heat and pluvial flood events and underlying factors that may affect these events. In this chapter, the successive heat-pluvial events refer to temporally compounding humid heat extremes followed by pluvial flooding, and extreme flooding followed by humid heat are termed successive pluvial-heat events. The findings of this chapter highlight the importance of addressing overlapping vulnerabilities due to compound humid heat and pluvial flooding extremes.

5.1 Global climatology of heat-pluvial and pluvial-heat events

Using two independent reanalysis datasets (ERA5 and NCEP), I quantify the global frequency of successive heat-pluvial and pluvial-heat events during 1956–2023. As shown in Figure 5.1, successive heat-pluvial events have occurred for almost all global land (with desert and polar regions excluded). The total number of successive heat-pluvial events observed in the two datasets is about 13 on average during 1956–2023 for each grid cell. Successive pluvial-heat events occur slightly less frequently, with an average of approximately 12 over the whole study period. Furthermore, I confirm the significance of the probability of successive events being greater than that expected by chance through the utilization of a moving-blocks bootstrap resampling-based significance test. (Figure 5.1c and Figure 5.1d). The test shows that the number of detected events based on both ERA5 and NCEP datasets exceed the 95% confidence interval estimates from moving-blocks bootstrap resampling that occur by chance, corresponding to the frequency of heat-pluvial and pluvial-heat of 11.80 and 9.73, respectively. This indicates that, on average globally,

successive heat-pluvial events occur about 11-23% more often than would be expected by chance, likely a signature of correlated heat and precipitation via local thermodynamics (i.e. convection) or colliding contrasting air masses (i.e. weather fronts) (Liao et al., 2021; Shang et al., 2020).

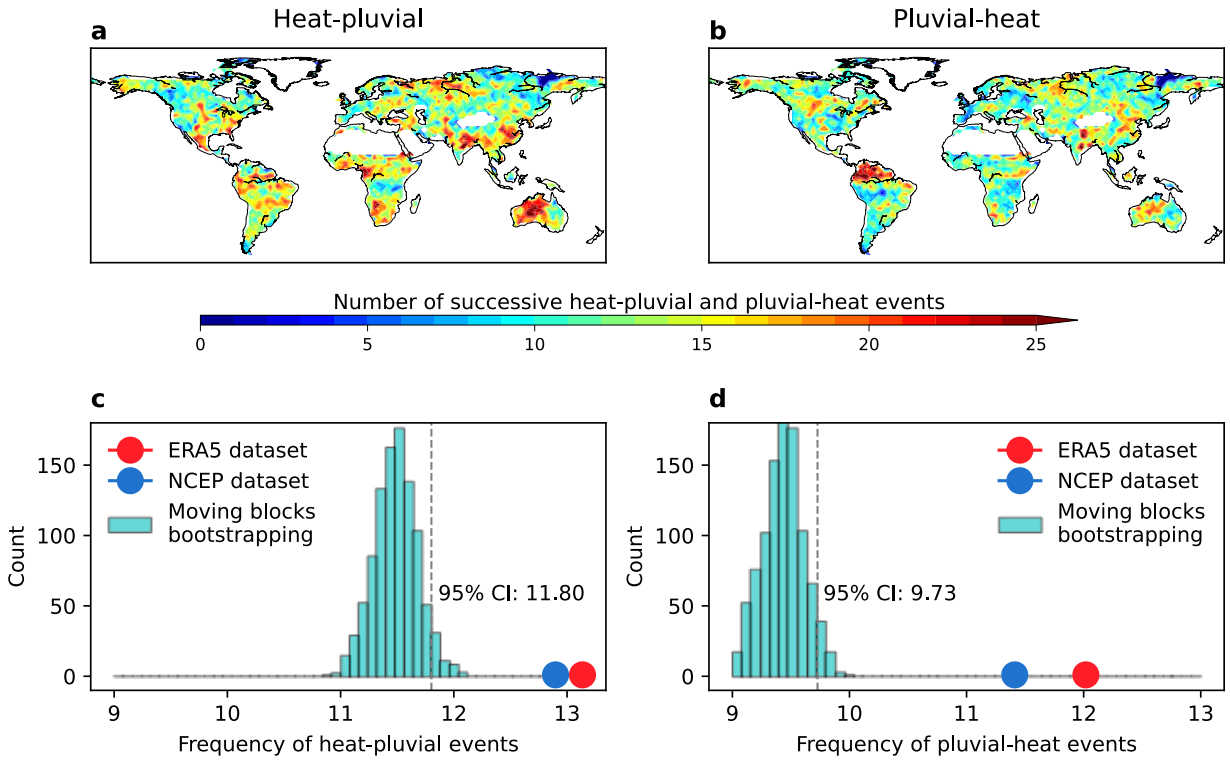

Figure 5.1 Frequency of successive heat-pluvial and pluvial-heat events within 7 days during 1956–2023. a, b Spatial maps showing the total number of successive heat-pluvial and pluvial-heat events, respectively. Grid cells that are statistically significant at the 0.05 level according to the moving-blocks bootstrap-resampling-based test are depicted as grey circles. The dataset used here is ERA5. c, d Significance test of the global-mean consecutive occurrence frequencies using moving-blocks bootstrap resampling based on ERA5 dataset for the heat-pluvial events (c) and pluvial heat events (d), respectively. The histogram represents the empirical distribution of global-mean successive events frequency using the 1,000 resampled series based on the moving-blocks bootstrap resampling. The 95% confidence interval is indicated by a vertical dashed line. The red dot and blue dot represent the number of successive events detected based on ERA5 and NCEP datasets, respectively. Looking at the spatial distribution of the number of events, both successive heat-pluvial and pluvial-heat exhibit clear regional differences globally, as illustrated in Figure 5.1a-b. To better identify the hotspots, I apply a 5×5 degree rolling average to smoothly plot the

maps. I find such temporally compounding extremes occur most often in West Australia, East North America, Sub-Saharan Africa, and North Asia (Figure 5.2), where they are statistically significant at the 0.05 level according to the moving-blocks bootstrap-resampling-based test (Figure 5.1a). Compared to the successive heat-pluvial events, the pluvial-heat events occur less frequently, but some hotspots maintain consistency — such as West Australia (Figure 5.1b). The spatial patterns remain similar even when events are defined using a more extreme percentile, despite having reduced peaks (Figure 5.3).

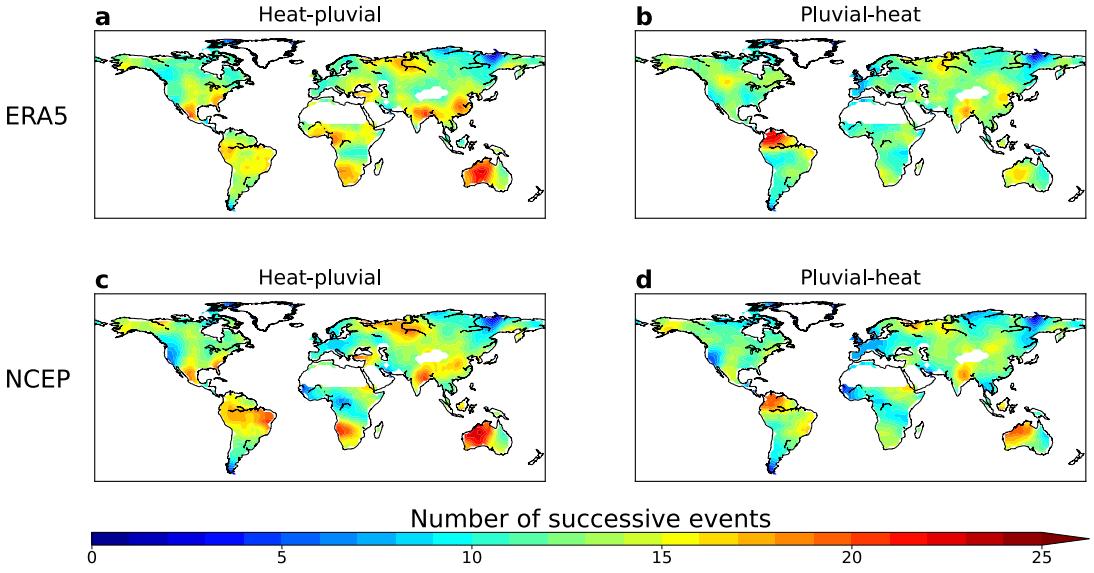

Figure 5.2 Rolling average of frequency of successive heat-pluvial and pluvial-heat events within 7 days during 1956–2023. A 5×5 degree rolling average was applied to smoothly plot the maps to better identify the hotspots.

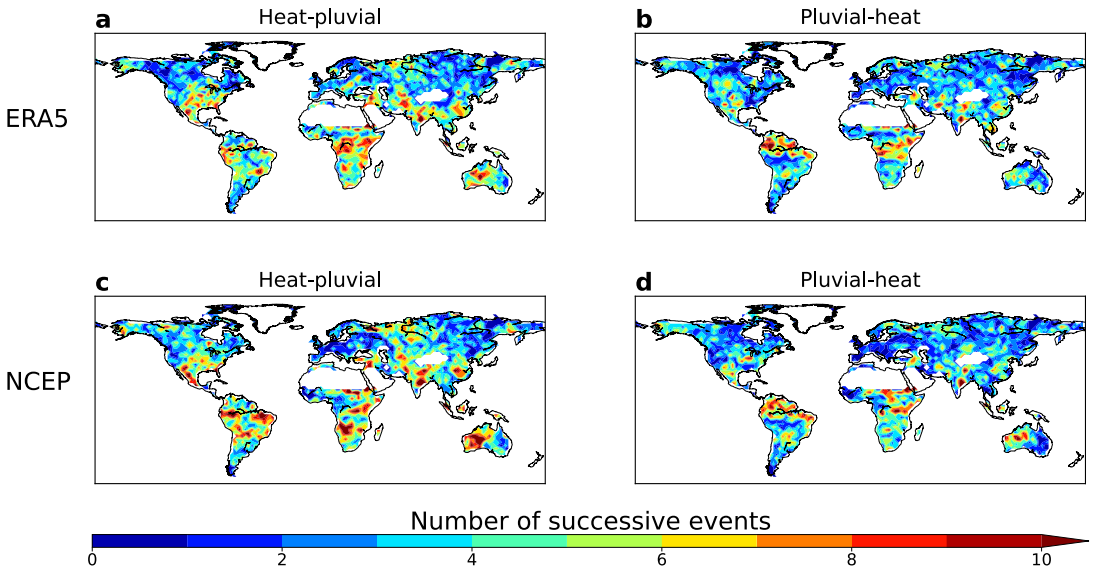

Figure 5.3 Frequency of successive heat-pluvial and pluvial-heat events within 7 days during 1956–2023 when employing the 95th percentiles to define heat and pluvial extremes. a, b Maps showing the total number of successive heat-pluvial and successive pluvial-heat events, respectively. The dataset used here is ERA5. c, d Same as a, b but for NCEP dataset.

5.2 Spatiotemporal changes in successive events and warming effect

I investigate the spatiotemporal changes in the frequency of temporally compounding heat and pluvial events from 1956 to 2023, by comparing the first (1956–1989) and second (1990–2023) 34-year periods, as shown in Figure 5.4a and Figure 5.5. In most regions, a higher frequency of successive heat-pluvial events is observed in the later (1990–2023) period compared to the earlier period (1956–1989). A rising trend in event frequency is identified in most parts of South America, Sub-Saharan Africa, South Asia, and North Australia, with 20 or more events during the latest 34-year period.

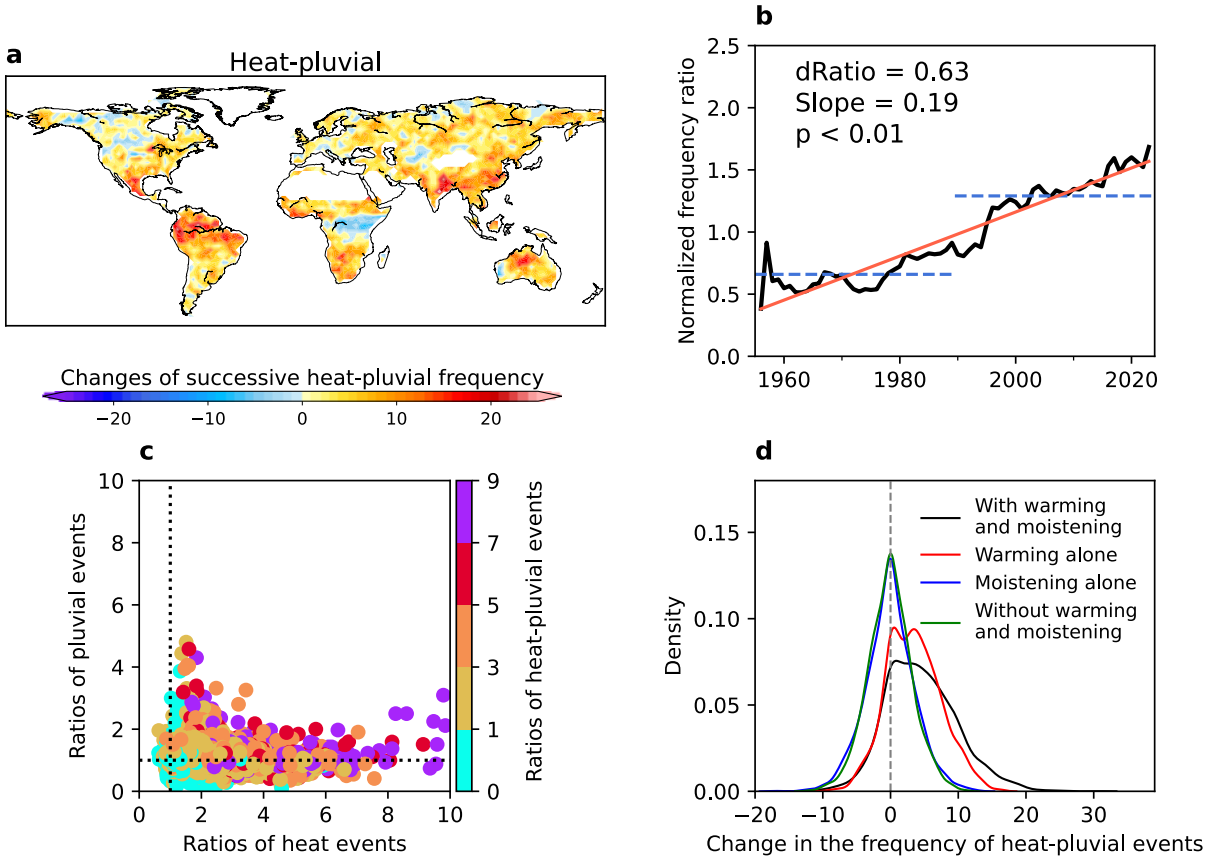

Figure 5.4 Spatiotemporal changes and decomposition in the frequency of successive heat-pluvial events within 7 days. a Spatial change in successive heat-pluvial events between the two 34-year periods (recent, 1990–2023 minus past, 1956–1989). b Annual time series of the normalized frequency ratio of successive heat-pluvial events. Black line is the annual normalized frequency ratio based on ERA5. A 10-year moving window was used to smooth the data. Blue dashed line is

the 34-year average. dRatio is the difference between the averages during 1956–1989 and 1990–2023. Red line represents the linear trend. Slope is the linear trend using the Sen-slope method (unit, decade). c The relationship between the changes in successive events and changes in individual extremes. Color circles show bin-averaged ratios of heat-pluvial events corresponding to ratios of individual extremes. d Decomposition of the frequency of heat-pluvial events due to warming/moistening effects. It shows the probability density function of the global mean changes in the frequency of heat-pluvial events between the two 34-year periods, based on raw observational data (black), data with moistening signal removed (red), data with warming signal removed (blue) and data with both warming and moistening signals removed (green). In general, the spatial patterns and temporal trends of ERA5 and NCEP are in good agreement (Figure 5.5 and Figure 5.6). However, there are some noticeable discrepancies over the eastern United States and sub-Saharan Africa, which may be attributed to data uncertainty and complex relationship between heat and convection, or potentially related to statistical effects from sequential events. The overall frequency of temporally compounding heat and pluvial events has seen a statistically significant (Mann–Kendall test, $p < 0.05$) increase for both event subcategories, with an increase of about 20% per decade (Figure 5.4b and Figure 5.6).

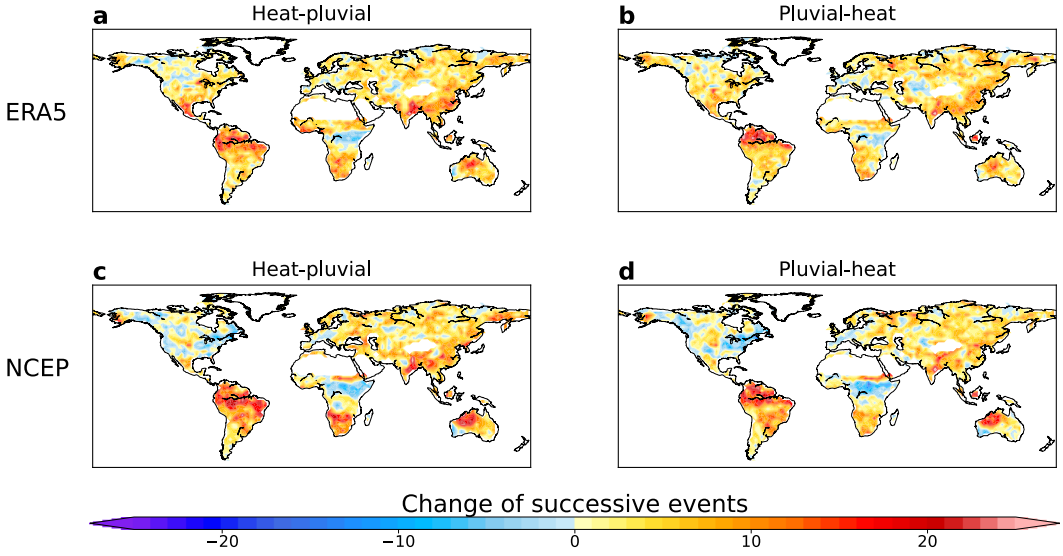

Figure 5.5 Spatial change in the frequency of successive events within 7 days between the two 34-year periods (recent, 1990–2023 minus past, 1956–1989). a, b Spatial changes in successive heat-

pluvial and pluvial-heat events, respectively. The dataset used for a and b is ERA5. c, d Same as a, b but for NCEP dataset.

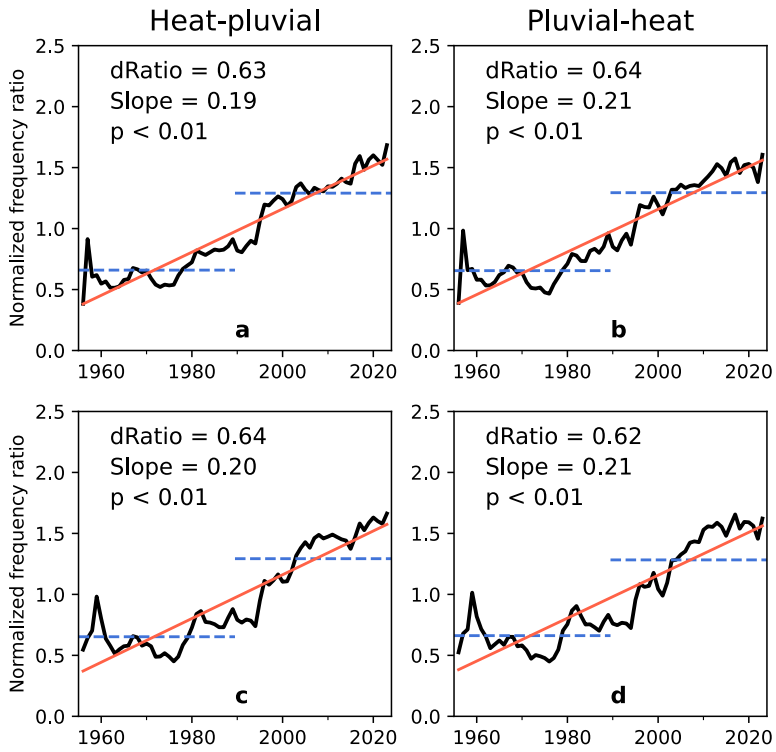

Figure 5.6 Annual change in the frequency of successive events within 7 days based on two different datasets during 1956–2023. A 10-year moving window was used to smooth the data. a, b Time series of the normalized frequency ratio in successive heat-pluvial and pluvial-heat events, respectively. The dataset used for a and b is ERA5. c, d Same as a, b but for NCEP dataset.

To explore further how the increases in individual extremes contribute to successive heat and pluvial events, I analyze the relationship between the changes in compound events and changes in individual extremes at the grid level between the two 34-year periods (Figure 5.4c, Figure 5.7 and Figure 5.8). In general, the upward trend in heat-pluvial event frequency is an expected consequence of these upward trends in univariate hazard frequencies. Specifically, as the frequency of individual heat events increases, there is a simultaneous rise in the occurrence of compound heat-pluvial events across more areas. However, the frequency of individual pluvial events does not exhibit a corresponding increase in these areas (Figure 5.9). This suggests that the increase in successive heat-pluvial events is primarily affected by changes in heat events, and is

consistent with the findings for successive pluvial-heat events, as well as with other work suggesting that increases in heat dominate the trends in many compound events involving temperature and another variables (Gu et al., 2022; Liu et al., 2022; Yin et al., 2022).

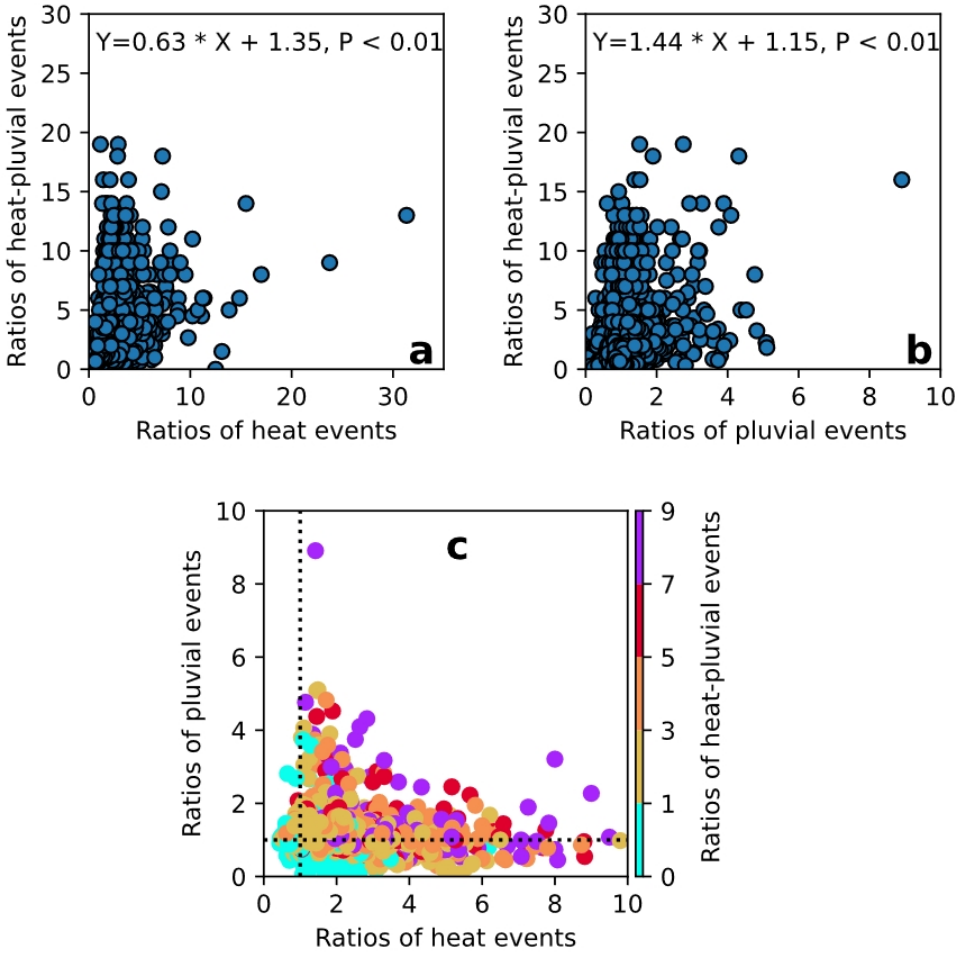

Figure 5.7 Relationship between the changes in successive heat-pluvial events and changes in individual extremes. Grid-based scatterplots between the ratio of heat-pluvial and heat (a), and between heat-pluvial and pluvial events (b). Colored circles in (c) show bin-averaged ratios of heat-pluvial events corresponding to ratios of individual extremes. The ratio is calculated as dividing number of events during the recent 34-year periods (1990–2023) by those in the past three decades (1956–1989).

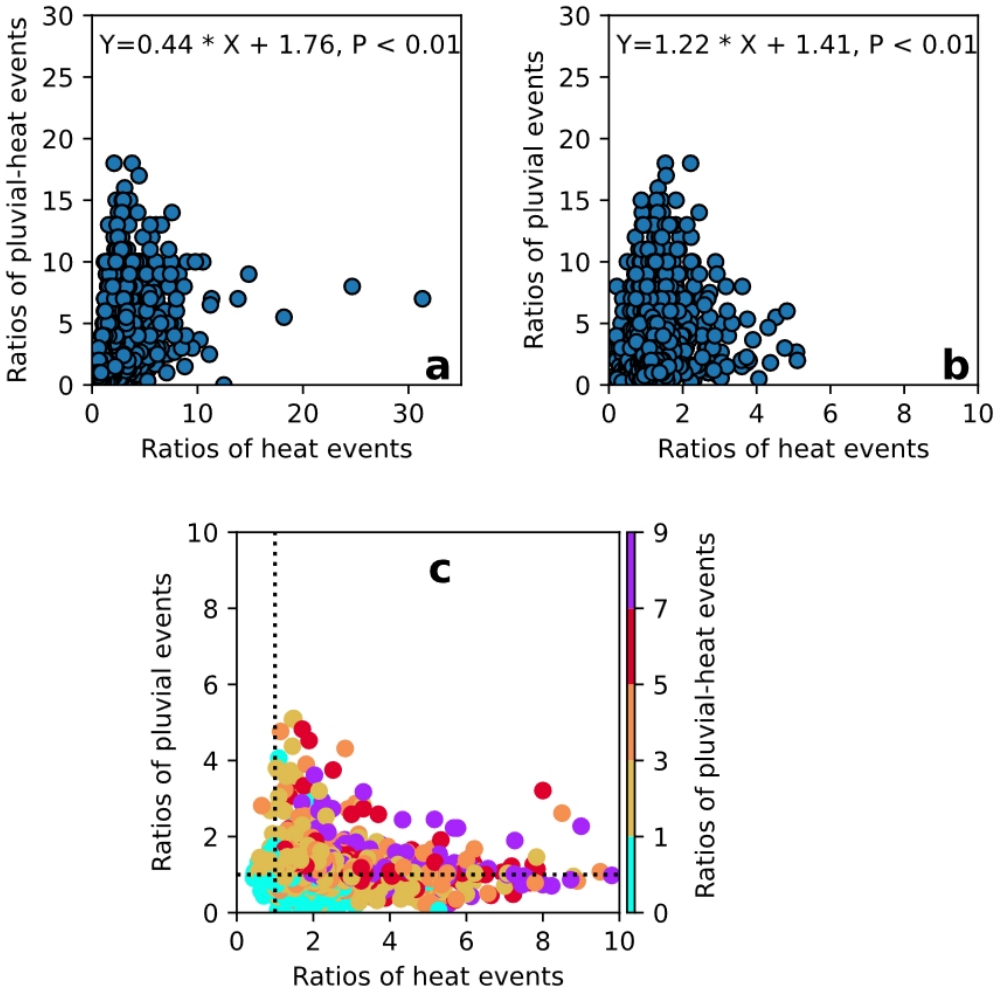

Figure 5.8 Same with Figure 5.7 but for successive pluvial-heat events.

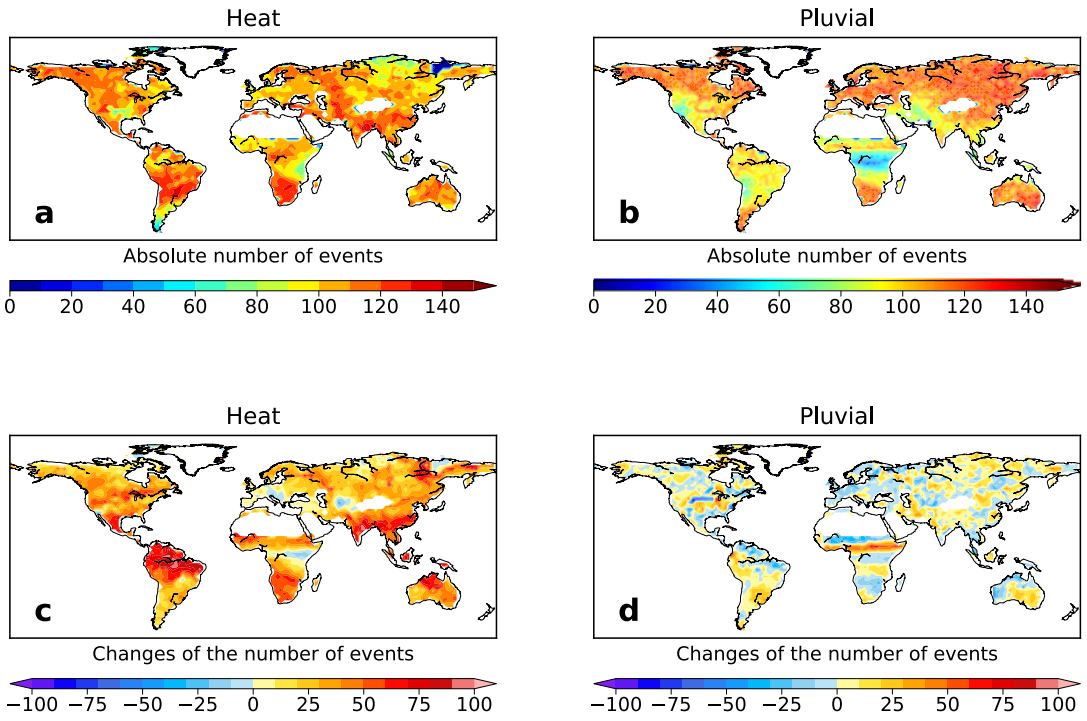

Figure 5.9 Frequency and change of individual events. a and b show the spatial pattern of the frequency of heat (left column) and pluvial (right column) during 1956–2023. c and d are the change of the heat and pluvial frequency over 1990–2023 relative to 1956–1989.

To explain the increased trend of successive heat and pluvial events, I conduct a decomposition analysis to disentangle the relative importance of the effects of warming and moistening on the trends of successive heat and pluvial events (Figure 5.4d and Figure 5.10). I find that the observed trends in heat-pluvial or pluvial-heat events can be reproduced by considering the influence of warming, specifically the change of wet-bulb temperature. In other words, the changes in these events can primarily be explained by the effect of warming alone (Figure 5.4d). The effect of warming is especially prominent in South America, South Asia, and North Australia, which are co-located with hotspots in Figure 5.4a, while moistening without warming has little effect (Figure 5.10 and Figure 5.11). In other words, once the warming effect has been removed there is no 'residual' increase in successive events. Therefore, it is the increased heat extremes under a warming climate that have made successive heat-pluvial and pluvial-heat events occur more frequently in recent decades.

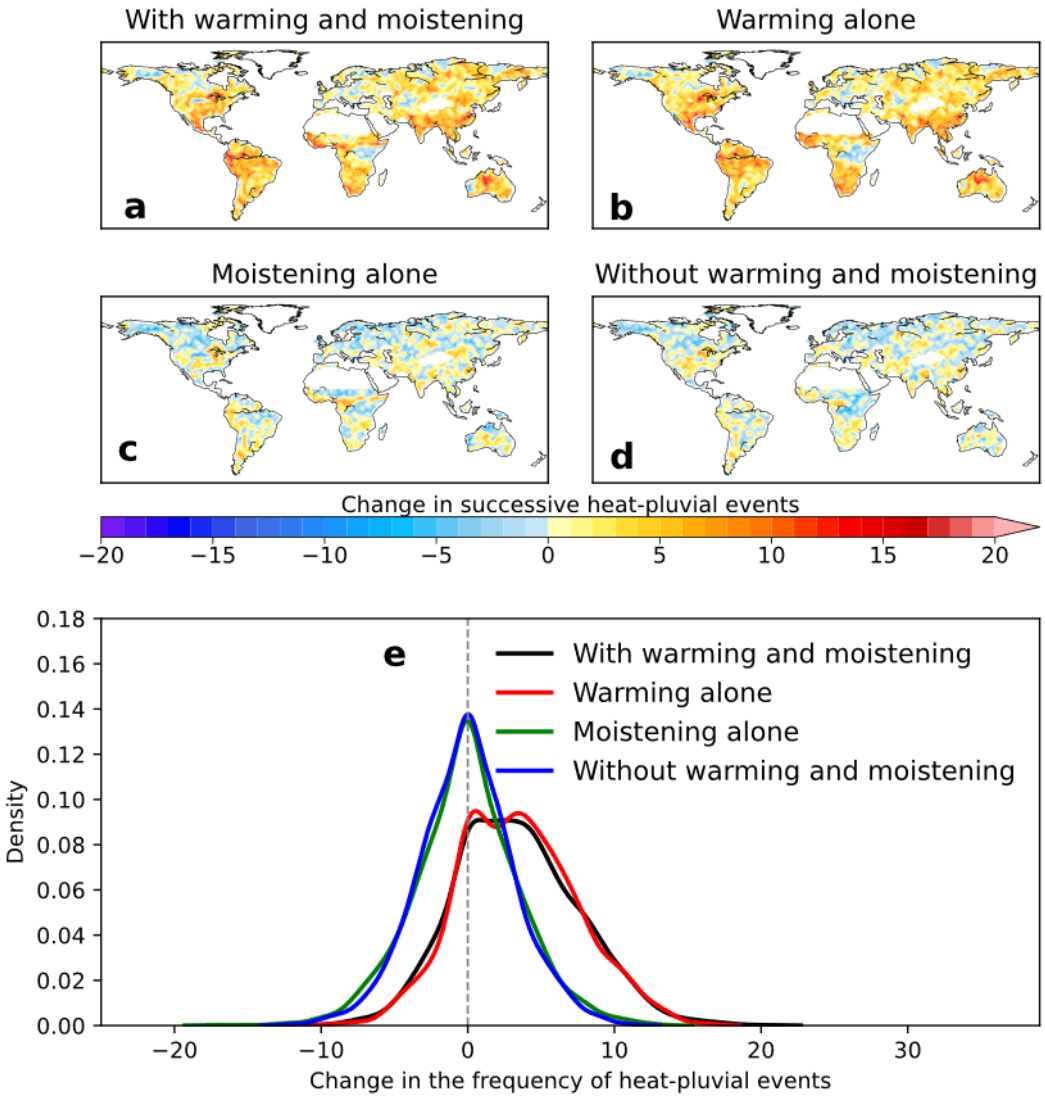

Figure 5.10 Driver of the trends of successive heat-pluvial events. The changes in the frequency of heat-pluvial events between the two 34-year periods, based on raw observational data (a), data with moistening signal removed (b), data with warming signal removed (c) and data with both warming and moistening signals removed (d). e shows the probability density function of the global mean frequency of successive events in a, b, c, and d.

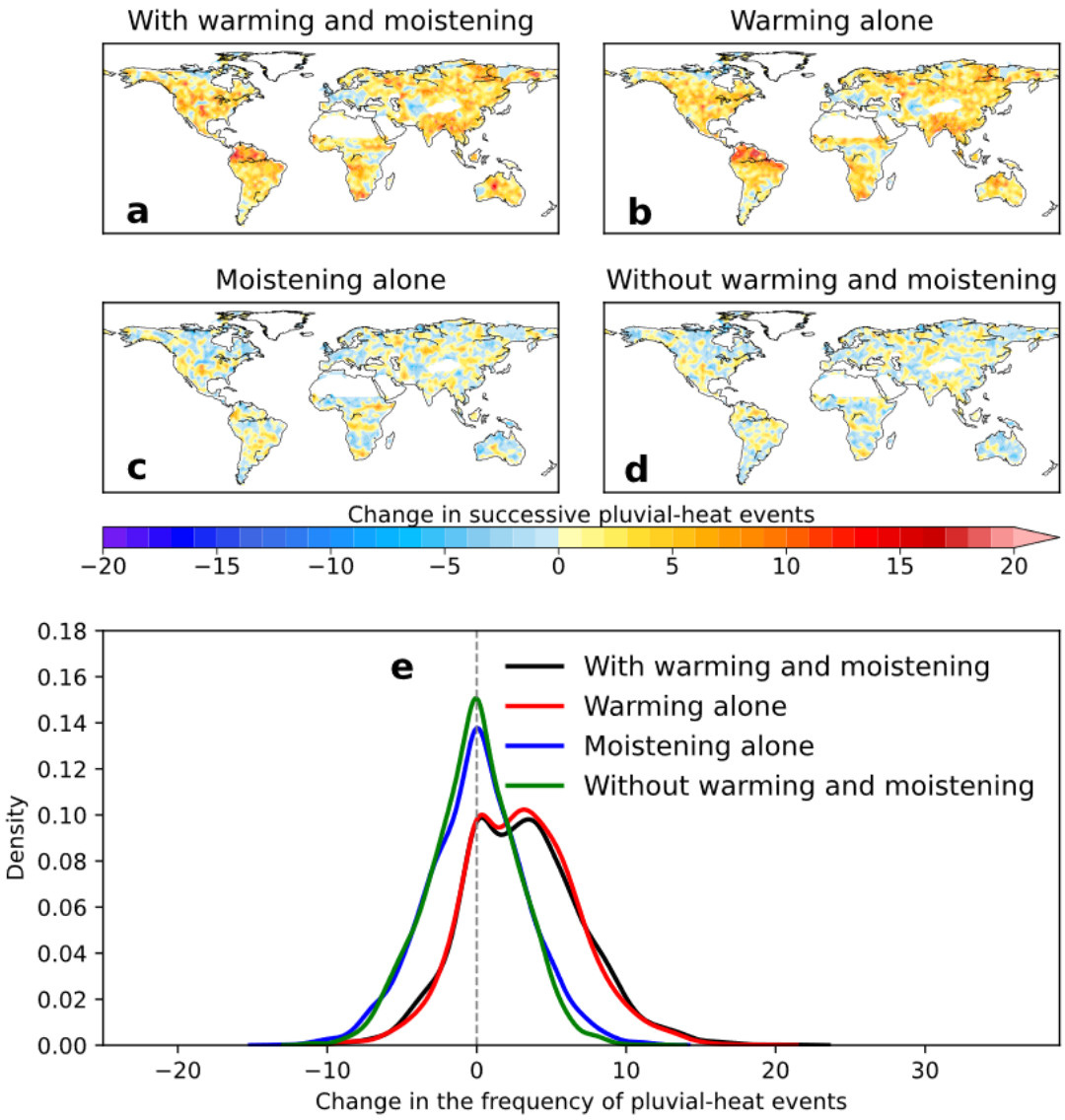

Figure 5.11 Same with Figure 5.10 but for successive pluvial-heat events.

5.3 Possible factor affecting the transitions between heat and pluvial events

In this section, I further examine the influence of VPD on transitions between heat and pluvial events. To address the issue of multiple hypothesis testing resulting from spatial dependence, I have conducted a field significance test to determine whether the differences in VPD between heat-pluvial and heat-without-pluvial events are statistically significant or not. I find significant differences in VPD exist between heat-pluvial and heat-without-pluvial events for about 85% of grid cells at the p=0.05 level (Figure 5.12), as well as a similar number for the comparison between pluvial-heat and heat-without-pluvial events using FDR test (Figure 5.13). Importantly, I reveal that small and negative VPD anomalies are linked to the transition from heat to pluvial (Figure 5.12a and Figure 5.12c), while high positive VPD anomalies accompany the transition from pluvial to heat (Figure 5.12b and Figure 5.12c). I find reduced VPD anomalies are associated with an increased probability of subsequent pluvial events. This is because lower VPD values, indicating higher humidity, create conditions that are more conducive to precipitation. Low VPD can alleviate some of the effects of extreme temperatures on plant health (Grossiord et al., 2020; Novick et al., 2016), and the high moisture content can supply the fuel for pluvial events, especially of a convective nature. On the contrary, increased VPD anomalies imply high atmospheric aridity, related to the termination of pluvial events and the abrupt onset of heat events. This finding echoes the observational evidence that high VPD enhances atmospheric demand for water, depleting soil moisture and simultaneously heating the atmospheric boundary layer (Teuling et al., 2013; Zhou et al., 2019).

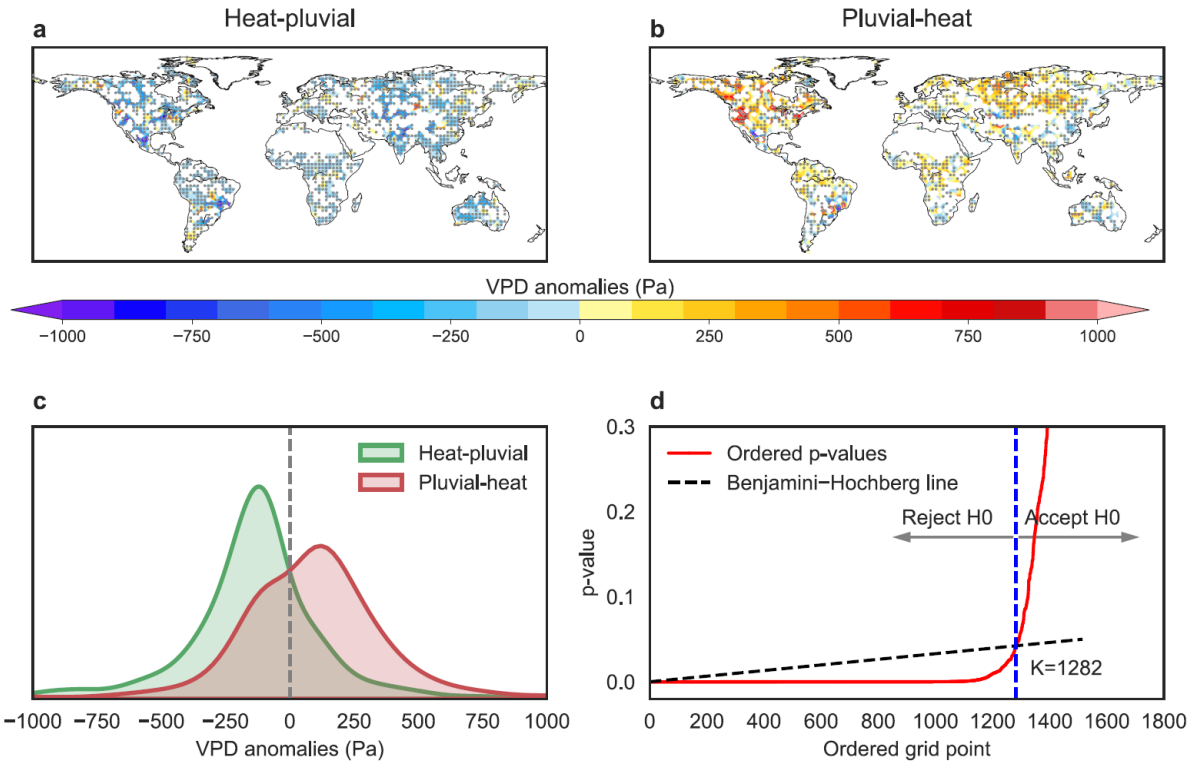

Figure 5.12 The behavior of VPD anomalies in the transition between heat and pluvial events. a represents VPD anomalies between heat events followed by pluvial events (heat-pluvial) and heat events not followed by pluvial events (heat-without-pluvial). b represents VPD anomalies between pluvial events followed by heat events (pluvial-heat) and pluvial events not followed by heat events (pluvial-without-heat). Grid points that meet local statistical significance at the 0.05 level are shown as grey circles, while the ones that meet the FDR criterion by having a sufficiently small p-value are marked by grey points. c is the probability density function of the map a (green line) and b (red line) for the VPD anomalies causing the transition between heat and pluvial events. d is the FDR for testing field significance of VPD anomalies (Pa) between heat-pluvial and heat-without-pluvial events.

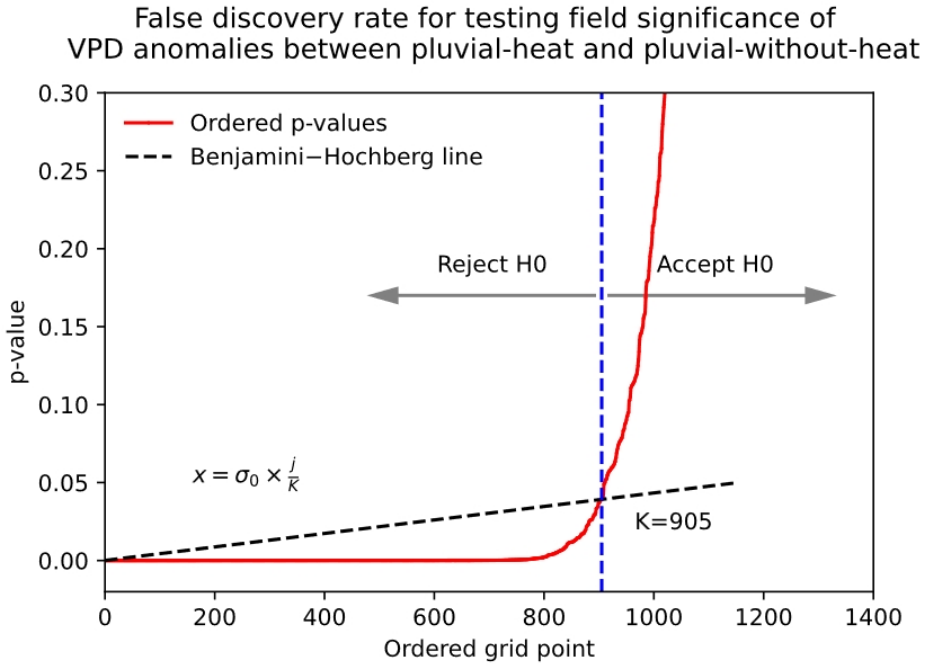

Figure 5.13 Result of the false discovery rate (FDR) for checking the field significance of VPD anomalies (Pa) between pluvial events followed by heat events (i.e., pluvial-heat) and pluvial events not followed by heat events (i.e., pluvial-without-heat).

5.4 Verification, sensitivity analysis and discussions of heat-pluvial and pluvial-heat events

5.4.1 Sensitivity analysis of data sources, time intervals and thresholds

To ensure the consistency and robustness of the analysis, I conduct multiple sensitivity analyses related to data sources, time intervals and thresholds, and alternative event definition. I verify the above-mentioned conclusions using alternative ERA5 and NCEP datasets with daily temporal resolution and global coverage. To avoid physical inconsistency among different data products, I use all essential variables from the same source for event identification rather than combining variables from alternative sources.

To perform the sensitivity test of thresholds, I also define the heat (pluvial) events as the top 5% of all TW (weighted average of precipitation) values (above the 95th percentile threshold). As expected, the use of a more extreme percentile largely reduces the number of successive heat-pluvial and pluvial-heat events, and thus the global average number of successive heat-pluvial events during 1956–2023 decreases to 2.8 and 2.3, respectively. Despite the considerable difference in the frequency of events, the significant increases in the frequency of heat-pluvial and pluvial-heat events are consistent in all three datasets (Figure 5.14).

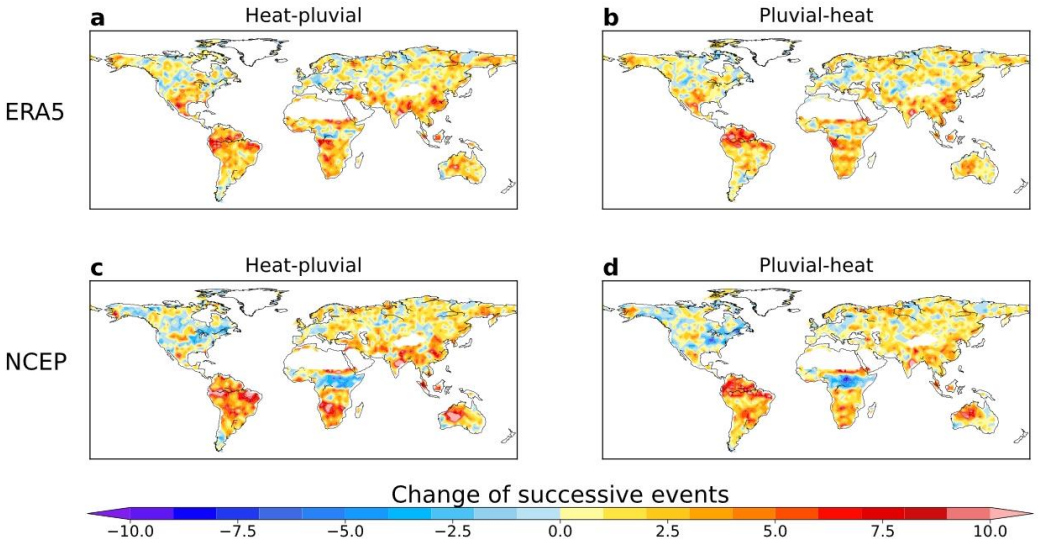

Figure 5.14 Spatial change between the two 34-year periods (recent, 1986–2023 minus past, 1956–1989) in the frequency of successive events within 7 days. Same as Figure 5.5 but a more extreme percentile is used for event definition (95th). In the main section of this study, a 7-day time interval

(time lag between heat and pluvial events) is adopted as an example for the identification of successive heat and pluvial events, which represents a relatively short time span for disaster preparedness and recovery. To test the sensitivity of different choices of prescribed settings, I also consider other potential impact-related time intervals between heat and pluvial events (5 days, 3 days, and 1 day). Although the frequency of successive heat-pluvial and pluvial-heat events is very sensitive to the choice of extreme thresholds and time lags (Figure 5.15, Figure 5.16, Figure 5.17, and Figure 5.18), the main results of increased trends in successive heat-pluvial and pluvial-heat events are robust. Disagreement between datasets has the largest effect on the results for eastern United States and sub-Saharan Africa regions.

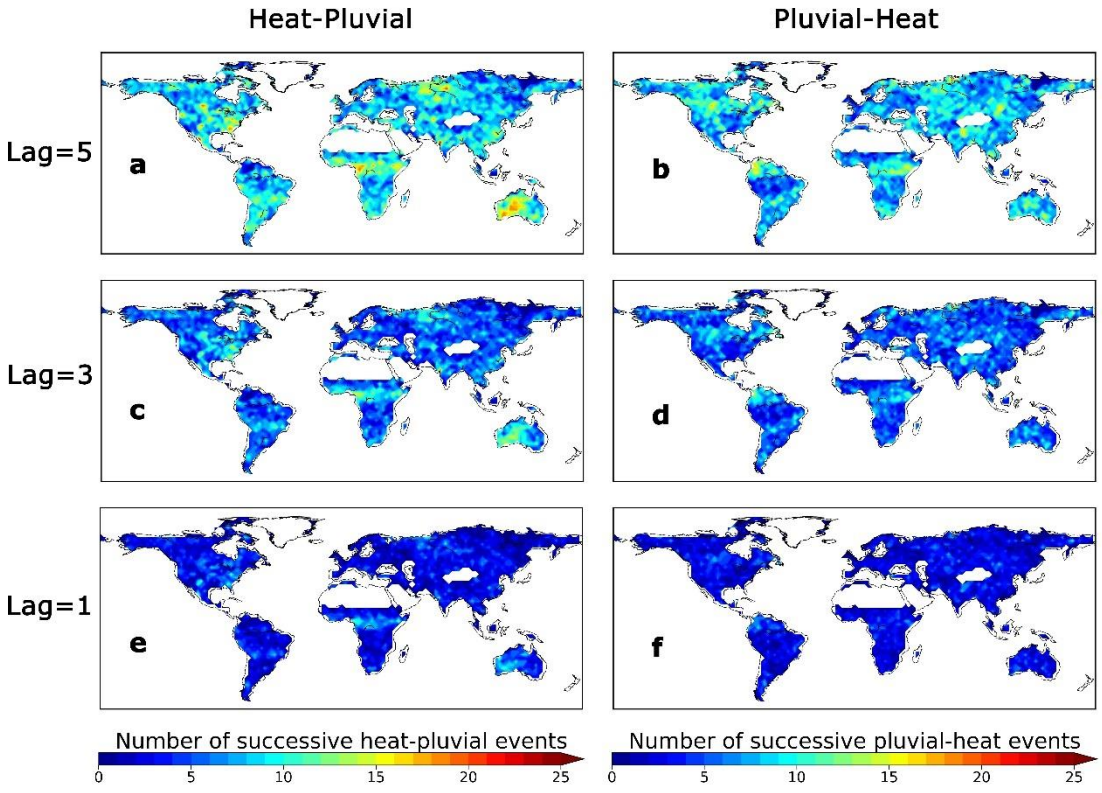

Figure 5.15 ERA5-based frequency of successive heat-pluvial and successive pluvial-heat events during 1956–2023 with the time lag of 5-day, 3-day, and 1-day, respectively. The dataset used here is ERA5.

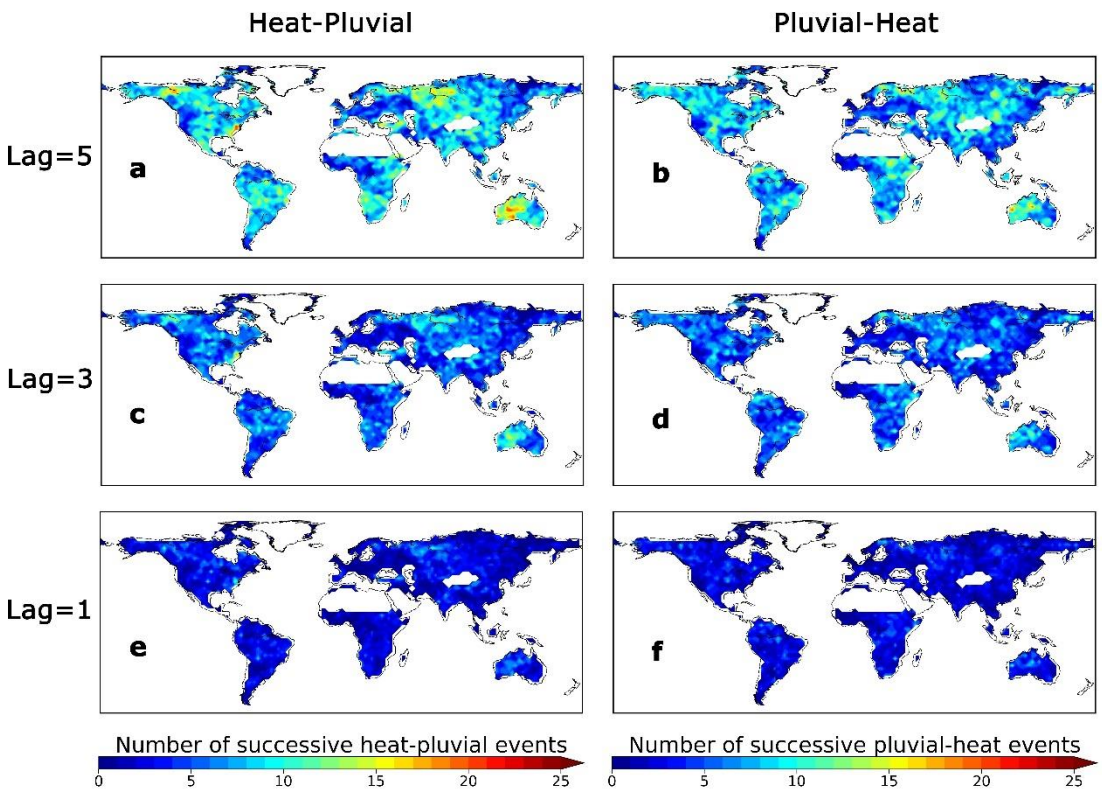

Figure 5.16 NCEP-based frequency of successive heat-pluvial and successive pluvial-heat events during 1956–2023 with the time lag of 5-day, 3-day, and 1-day, respectively. The dataset used here is NCEP.

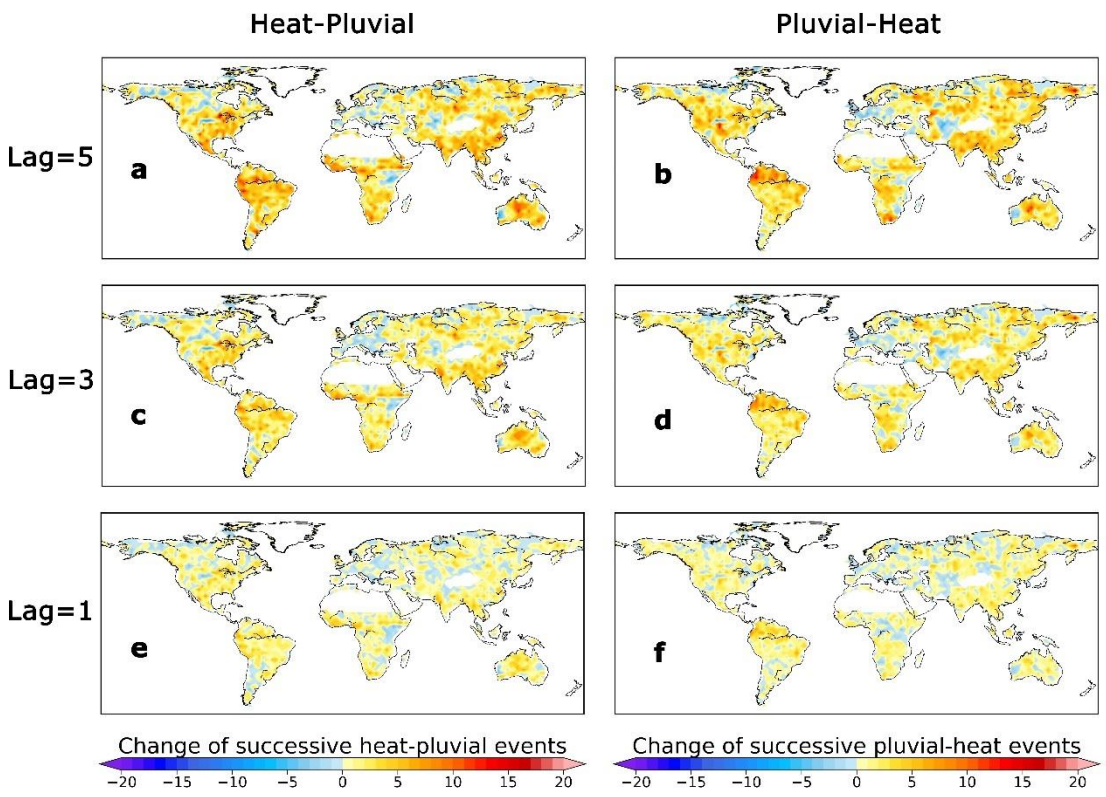

Figure 5.17 ERA5-based spatial change between the two 34-year periods (recent, 1990–2023 minus past, 1956–1989) in the frequency of successive events with the time lag of 5-day, 3-day and 1-day, respectively. The dataset used here is ERA5.

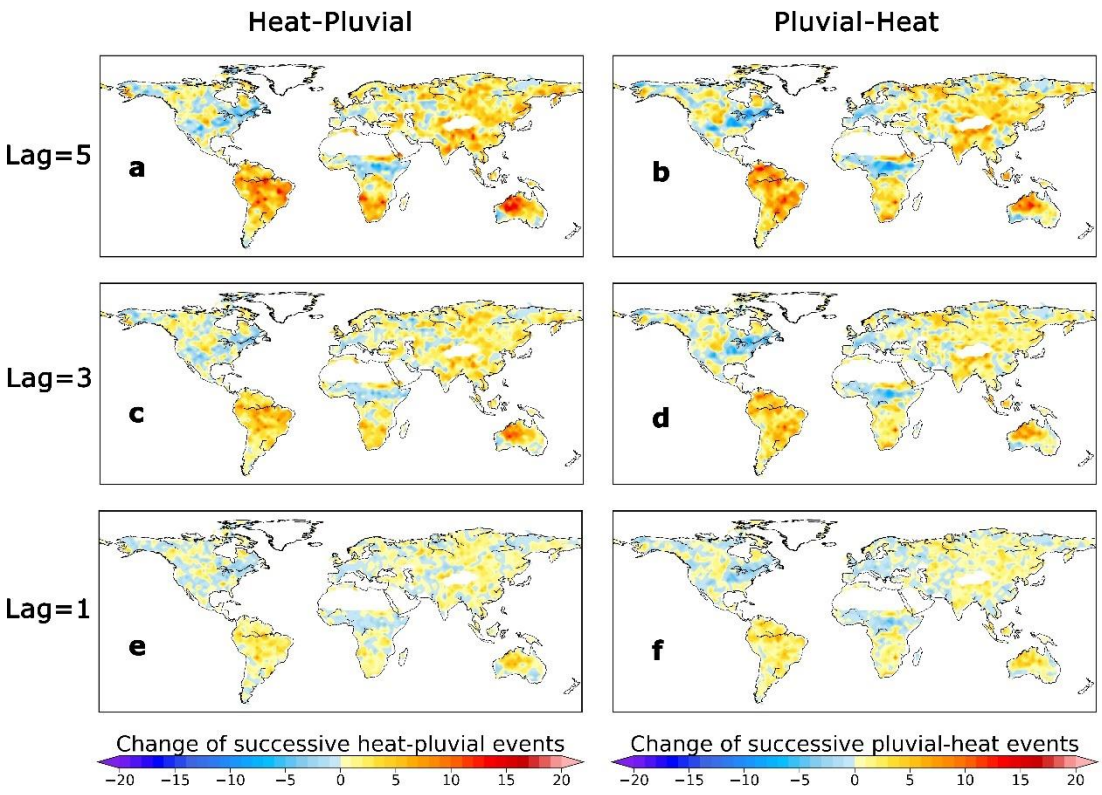

Figure 5.18 NCEP-based spatial change between the two 34-year periods (recent, 1990–2023 minus past, 1956–1989) in the frequency of successive events with the time lag of 5-day, 3-day and 1-day, respectively. The dataset used here is NCEP.

5.4.2 Field significance test using two alternative methods

The study aimed to determine whether there were significant differences in VPD between heat-pluvial and heat-without-pluvial events. To do this, I use field significance tests, which confirmed that the observed differences are not due to random chance or measurement error, but rather reflected real differences between the two types of events. To ensure the reliability of the analysis, I also use two alternative methods: Walker's test and moving block bootstrapping-based multivariate test, both of which provide consistent results (Figure 5.19, Figure 5.20 and Figure 5.21).

When assessing field significance using Walker's test, the grey points in Figure 5.13 locate the same 1293 grid elements with p-values smaller enough to meet Walker's criterion. In other words, among 1516 local tests, there are 85.29% grid points have passed the field significance test,

which indicates that statistically field significant differences in VPD exist between heat-pluvial and heat-without-pluvial at the field significance level of 0.05. For moving block bootstrapping-based multivariate test, as shown in Figure 5.19, it can be observed that the field statistic d_i^* obtained from the ERA5 dataset is significantly lower than the values obtained from 1000 moving blocks bootstrap realizations. This indicates strong statistical significance of the field. In terms of VPD anomalies between pluvial events followed by heat events (pluvial-heat) and pluvial events not followed by heat events (pluvial-without-heat), the results are also significant. Combining Figure 5.20 and Figure 5.21, I also show that statistically field significant differences in VPD exist between pluvial-heat and pluvial-without-heat at the field significance level of 0.05.

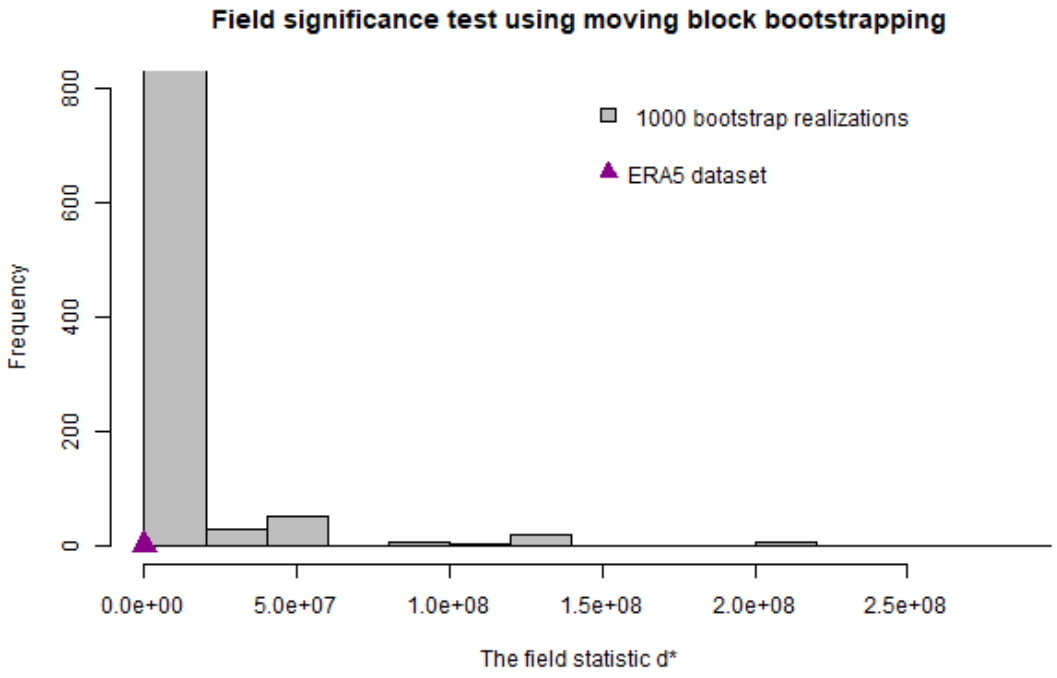

Figure 5.19 Result of moving block bootstrapping for testing field significance of VPD anomalies (Pa) between heat events followed by pluvial events (i.e., heat-pluvial) and heat events not followed by pluvial events (i.e., heat-without-pluvial).The histogram represents the distribution of results from 1000 moving blocks bootstrap realizations of the field statistic d_i^* and the purple triangle represents the test statistic d from the observed data.

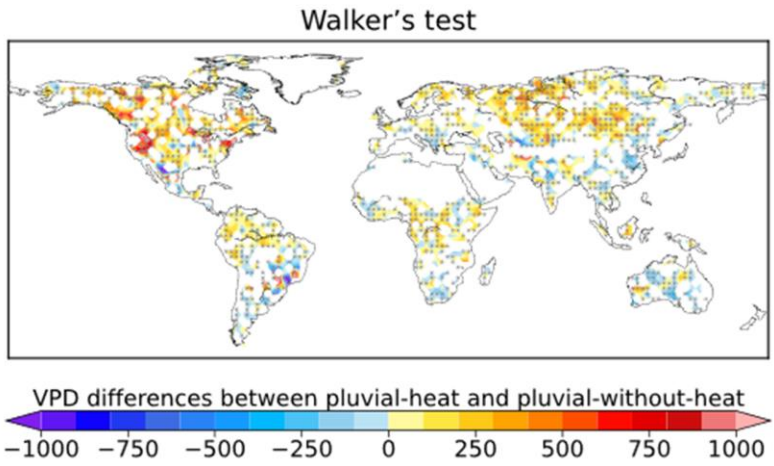

Figure 5.20 Result of Walker's test to check the field significance of VPD anomalies (Pa) between pluvial events followed by heat events (i.e., pluvial-heat) and pluvial events not followed by heat events (i.e., pluvial-without-heat).Grid points that satisfy local statistical significance at the $\alpha_0 = 0.05$ level are shown as grey circles, while the ones that meet Walker's criterion by having a sufficiently small p-value are marked by grey points.

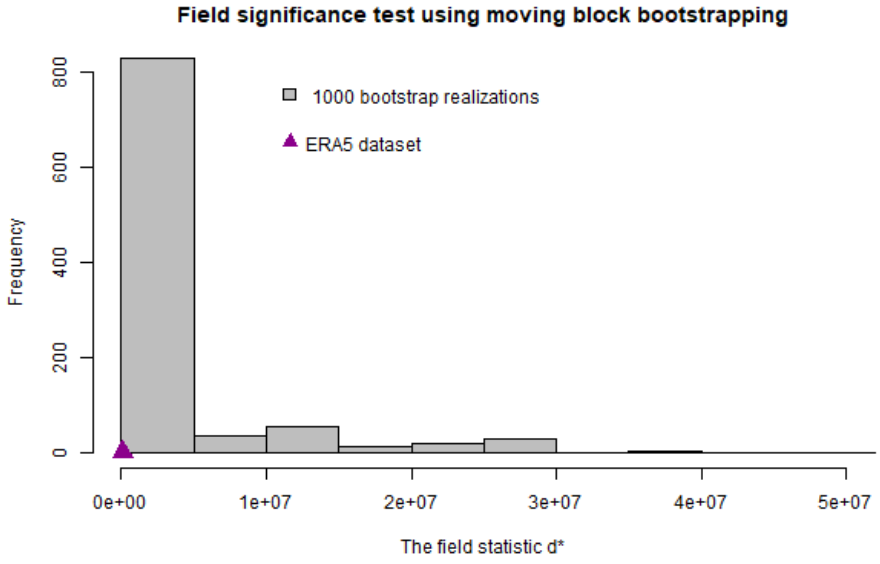

Figure 5.21 Result of moving block bootstrapping for testing field significance of VPD anomalies (Pa) between pluvial events followed by heat events (i.e., pluvial-heat) and pluvial events not followed by heat events (i.e., pluvial-without-heat).The histogram represents the distribution of results from 1000 moving blocks bootstrap realizations of the field statistic d_i^* and the purple triangle represents the test statistic d from the observed data.

5.5 Discussions and summary of the chapter

Humid heat and pluvial flooding are serious weather extremes by themselves, but when occurring sequentially at the same location, they can cause more severe consequences than an isolated extreme event. While extreme heat or pluvial flooding alone has attracted considerable attention over the past decades (Fischer et al., 2021; Martin, 2018; Sun et al., 2021; Wang et al., 2021b), the global climatology of successive heat and pluvial events remains unclear.

In this chapter, I perform a comprehensive global assessment of heat-pluvial and pluvial-heat events. The order of these events matters: when heat precedes, the soil becomes parched, hindering water absorption and resulting in flash floods during subsequent rainfall. Conversely, when heavy rainfall occurs first, it damages infrastructure, making it challenging to cope with subsequent heat waves. Through analyzing both event sequences, the chapter helps gain a deeper understanding of the risks associated with each sequence. Based on two datasets, I reveal the baseline frequencies and spatiotemporal changes of successive extremes. The findings demonstrate the increased risk of rapid transition between heat and pluvial events in a warmer climate in recent decades. Hotspots are centered in West Australia, East North America, Sub-Saharan Africa, and North Asia. I find that more frequent heat extremes due to a warming climate have resulted in a higher incidence of heat-pluvial and pluvial-heat events. Furthermore, the findings demonstrate that notable VPD anomalies are typically observed in the transitions between heat and pluvial events.

Extreme temporally compound events are often rare, and their occurrence can be coincidental due to chance. This chapter highlights the value of using bootstrap resampling-based significance tests, a method that has been overlooked in previous studies (Chen et al., 2021; Zhang & Villarini, 2020). Specifically, it is crucial to consider autocorrelation when randomly sampling time series of precipitation and temperature. This consideration is particularly significant when defining events based on a sequence of consecutive hot or wet days. The moving-blocks bootstrapping method used in this chapter accounts for the uncertainty in temporally correlated event coincidence by generating a set of surrogate time series that have the same statistical properties, including temporal covariance structure or temporal correlation, as the original time series (Vogel & Shallcross, 1996).

The chapter indicates that VPD plays a vital role in temporally compounding heat and pluvial events, which are often ignored in previous compound events. Importantly, I highlight the asymmetric impacts of VPD on the rapid transitions between heat and pluvial extremes, which could provide a reference and insight into early warning and anticipation of emerging temporally compounding hydrological hazards. The physical mechanisms underlying compound heat and pluvial events are complex. While detecting and presenting a global assessment of two emerging compound extremes is the priority and focus on this chapter, identifying the process-based evolution and underlying mechanisms of the rapid transition from extreme heat to pluvial or vice versa from a physical standpoint is an important and challenging task. Future studies should be undertaken to further investigate these mechanisms and help advance our understanding of compound hazards.

Chapter 6. Conclusion and future work

This chapter synthesizes research findings and suggests future directions in compound hydrometeorological studies.

6.1 Research conclusions

In this dissertation, a variety of approaches have been developed to improve the detection and attribution of emerging compound hydrometeorological risks. Specifically, a novel vine copula ensemble machine learning approach, combining the advantages of state-of-the-art machine learning methods, has been developed to reconstruct temporally-continuous coastal flooding induced by storm surges and sea level rise. Bayesian hierarchical models have been proposed for probabilistic modeling to estimate storm surges and sea level rise in regions without tidal gauge stations. Statistical methods for multi-hazard analysis of compound flood risks in coastal areas have been developed. A framework for detection, attribution, and projection analysis has been used to investigate consecutive heat waves and heavy rainfall. This marks the first attempt to investigate a newly identified category of temporally compound events. Lastly, my work leads to a comprehensive global analysis of compound humid heat and pluvial flooding, utilizing the moving-blocks bootstrap test and innovative field significance tests I introduce for enhanced accuracy in the detection and attribution of compound hydrometeorological events.

The research presented in this thesis offers a multi-scale analysis of compound hydrometeorological risks, integrating insights from local, regional, and global perspectives to provide a comprehensive understanding of these emerging hazards in a warming climate. In Chapter 3, the probabilistic modeling approach developed in this chapter enhances hydrometeorological prediction in data-sparse regions, provides insights into the joint impact of multiple drivers on flood risk. By focusing on Hong Kong's coastal flood risks, the understanding compound flood events at a local scale is underscore. The scope is then broadened to a regional scale in Chapter 4. The findings emphasize the growing risk of shorter, intense heat waves followed by heavy rainfall. Examination of CHWHR events across China allows for the identification of key spatial character, and further enhance our understanding on temporal dynamics of compound extremes in different climate zones. Finally, Chapter 5 expands the

analysis to a global scale, investigating the two-direction shifts between hot and wet extremes. Both heat-pluvial and pluvial-heat events are included in the scope, and this global perspective reveals broader patterns and trends, demonstrating the global nature of these risks. The identification of statistically significant correlations between these events and global warming further provides critical insights for global climate risk assessments. Together, these chapters demonstrate that the scale of analysis, from local to global, significantly influences the detection, attribution, and mitigation of compound hydrometeorological risks.

The dissertation yields the following findings and contributions:

(1) I propose a vine copula ensemble model for accurate continuous storm surge and sea level reconstruction. This model fills a crucial gap left by tide gauge measurements, which often lack long-time records for trend detection and extreme value analysis. It not only outperforms individual machine learning models but also offers enhanced flexibility in selecting modeling structures, resulting in improved alignment with observed data and better capture of variability in storm surges and sea level reconstruction. Furthermore, the integration of machine learning models enhances the accuracy of uncertainty quantification compared to relying on a single model. This is vital for reliable storm surges and sea level predictions, aiding decision-makers in implementing effective mitigation measures to manage risks in coastal areas.

(2) I introduce a Bayesian Hierarchical Modeling (BHM) framework that enhances spatially-continuous storm surge and sea level estimation, overcoming data sparsity limitations. By leveraging information from nearby tide gauges, the BHM provides predictions in ungauged areas, ensuring comprehensive insights where observations are lacking. Its consistent and accurate performance, validated across multiple experiments, underscores its reliability in data-sparse regions. Furthermore, the BHM enables a thorough assessment of uncertainties, empowering decision-makers with deeper insights into storm surge and sea level variability and risk. Its probabilistic predictions aid in establishing risk thresholds, facilitating better preparedness and protection against storm surges and sea level rise. By establishing risk thresholds and integrating probabilistic predictions, decision-makers can accurately evaluate and mitigate coastal flood risks.

(3) I conduct a comprehensive analysis of compound flood risk assessment, focusing on the concurrent occurrence of storm surge, heavy rainfall, and sea level rise. By examining the

complex links between these factors, I reveal their joint impact on escalating coastal flood risk in Hong Kong. Specifically, I identify significant increases and positive dependences among extreme storm surges, sea level rise, and heavy rainfall, indicating a risk of compound flooding. Furthermore, I demonstrate the heightened risk and severity in compound flood events, revealing significant increases in return levels for both heavy rainfall and extreme storm surges when these factors coincide. These findings underscore the urgent need to address multi-hazard flood risk, particularly in densely populated and infrastructure-rich coastal urban cities.

(4) I present new evidence on the compounding effect of consecutive heat waves and heavy rainfall. Through coincidence detection, attribution analysis, and climate projection, I reveal the probability of occurrence, underlying mechanisms, and future trends of these events. Importantly, my findings emphasize a higher likelihood of hotter and shorter heat waves followed by heavy rainfall, which can be associated with atmospheric convection and moisture convergence. Furthermore, climate projections indicate that these events will occur with greater frequency and suddenness in the future, exacerbating the compounded risk. These findings underscore the imperative of proactive measures to mitigate the dual risks posed by these extremes. Specifically, my work highlights the importance of early warning systems and preparedness strategies to address potential hazards, particularly flash flooding, when a short-duration but high-intensity heat wave is witnessed.

(5) I offer the first and most comprehensive assessment of the rapid shifts between hot and wet extremes, investigating both combinations of temporally compounding hazards: humid heat preceding pluvial flooding (heat-pluvial) and pluvial flooding followed by humid heat (pluvial-heat). I have identified growing threats from compound heat-pluvial and pluvial-heat events in a warmer world. These successive extremes occur more frequently within warm seasons, with a statistically significant increase in frequency attributed to global warming. Furthermore, I have explored the influence of vapor pressure deficit (VPD), revealing correlations between heat-pluvial (pluvial-heat) events and VPD anomalies. These findings are statistically significant, underscored by robust methodologies like moving-blocks bootstrap resampling and field significance tests. My contributions shed light on the escalating risks posed by compound hot and wet extremes, offering vital insights for understanding and addressing the challenges of emerging compound hydrometeorological risks.

6.2 Future work

In this dissertation, the proposed vine copula ensemble models employ a one-way coupling method, integrating outputs from deep learning models such as Long Short-Term Memory, Random Forest, and Convolutional Neural Network as inputs. While this approach offers advantages, it poses limitations concerning potential inefficiencies in information transfer and integration between models. Future research could benefit from adopting a more integrated approach, combining various models into a bidirectionally cohesive framework. This can ensure a streamlined exchange of compound hydrometeorological extreme information, overcoming the constraints of the one-way coupling method and enhancing the predictive accuracy of compound hydrometeorological hazards.

Regarding the Bayesian hierarchical models utilized in this dissertation, while they improve upon the traditional single-point modeling approach, their current limitation lies in considering only nearby locations and the continental shelf's characteristics as covariates. Future enhancements can focus on integrating a broader array of climatic variables into these models. These variables could include temperature, precipitation, wind speed, humidity, atmospheric pressure, and so on. Additionally, it's vital to broaden the use of these models in areas often impacted by hydroclimate-related hazards, particularly in locations with limited observational data, such as regions lacking adequate in-situ stations.

In studying consecutive heat wave and heavy rainfall events, efforts have been made to explore large-scale atmospheric variables including convective available potential energy, convective inhibition, and vertically integrated moisture divergence on these phenomena. It's been observed that shorter duration, yet more intense, heat waves are often followed by heavy rainfall. This finding is pivotal for the development of early warning systems and proactive strategies to address such events. Based on the above findings, future work can focus on creating real-time early warning systems for compound events forecast. These systems would be adept at rapidly processing real-time hydroclimatic data, enabling them to issue timely alerts for the likelihood of consecutive heat wave and heavy rainfall events.

In my research on temporally compounding events involving humid heat and pluvial flooding, the significant role of vapor pressure deficit in driving rapid transitions between these

extremes has been highlighted. However, despite this important finding, comprehensively understanding the physical mechanisms at play in these compound humid heat and pluvial flood events remains a complex challenge. Future research may be directed towards a more thorough investigation of the underlying physical mechanisms driving these sequential events. This includes delving into drivers like teleconnections and land-atmosphere coupling by developing advanced process-based climate simulation models and causal inference approaches. Such in-depth exploration is vital for advancing our knowledge of these complex phenomena and enhancing our ability to predict, manage, and mitigate their impacts.

Finally, future work can conduct in-depth assessments of the socio-economic impacts of compound hydrometeorological events through real-world case studies. While traditional risk assessments have primarily concentrated on the frequency, duration, intensity, and impact of individual hazards, the emergence of compound events underscores the necessity to consider multivariate hazards and adopt impact-based methodologies. An interdisciplinary approach, integrating insights from climatology, hydrology, economics, and social sciences, is crucial to unravel the complex interactions between these events and their socio-economic consequences. Such a comprehensive understanding of the socio-economic impacts of compound extremes can significantly enhance the development of mitigation and adaptation strategies, thereby effectively addressing the emerging risks associated with compound hydrometeorological extremes in a warming climate.

References

Alipour, A., Yarveysi, F., Moftakhari, H., Song, J. Y., & Moradkhani, H. (2022). A multivariate scaling system is essential to characterize the tropical cyclones' risk. Earth's Future, 10(5), e2021EF002635. https://doi.org/10.1029/2021EF002635

Arns, A., Wahl, T., Wolff, C., Vafeidis, A. T., Haigh, I. D., Woodworth, P., et al. (2020). Non-linear interaction modulates global extreme sea levels, coastal flood exposure, and impacts. Nature Communications, 11(1), 1918. https://doi.org/10.1038/s41467-020-15752-5

BBC News. (2020). UK heatwave: Thunderstorms and flash floods after scorching heat, available at: https://www.bbc.com/news/uk-53760283, last access: 25 April 2021.

Beck, H. E., Wood, E. F., Pan, M., Fisher, C. K., Miralles, D. G., Dijk, A. I. J. M. van, et al. (2019). MSWEP V2 Global 3-Hourly 0.1° Precipitation: Methodology and Quantitative Assessment. Bulletin of the American Meteorological Society, 100(3), 473–500. https://doi.org/10.1175/BAMS-D-17-0138.1

Beck, N., Genest, C., Jalbert, J., & Mailhot, M. (2020). Predicting extreme surges from sparse data using a copula-based hierarchical Bayesian spatial model. Environmetrics, 31(5), e2616. https://doi.org/10.1002/env.2616

Benjamini, Y., & Hochberg, Y. (1995). Controlling the false discovery rate: a practical and powerful approach to multiple testing. Journal of the Royal Statistical Society: Series B (Methodological), 57(1), 289–300. https://doi.org/10.1111/j.2517-6161.1995.tb02031.x

Berg, P., Moseley, C., & Haerter, J. O. (2013). Strong increase in convective precipitation in response to higher temperatures. Nature Geoscience, 6(3), 181–185. https://doi.org/10.1038/ngeo1731

Bevacqua, E., De Michele, C., Manning, C., Couasnon, A., Ribeiro, A. F. S., Ramos, A. M., et al. (2021). Guidelines for studying diverse types of compound weather and climate events. Earth's Future, 9(11), e2021EF002340. https://doi.org/10.1029/2021EF002340

Bevacqua, E., Maraun, D., Vousdoukas, M. I., Voukouvalas, E., Vrac, M., Mentaschi, L., & Widmann, M. (2019). Higher probability of compound flooding from precipitation and storm surge in Europe under anthropogenic climate change. Science Advances, 5(9), eaaw5531. https://doi.org/10.1126/sciadv.aaw5531

Bevacqua, E., Vousdoukas, M. I., Zappa, G., Hodges, K., Shepherd, T. G., Maraun, D., et al. (2020). More meteorological events that drive compound coastal flooding are projected under climate change. Communications Earth & Environment, 1(1), 1–11. https://doi.org/10.1038/s43247-020-00044-z

Bloemendaal, N., Muis, S., Haarsma, R. J., Verlaan, M., Irazoqui Apecechea, M., de Moel, H., et al. (2019). Global modeling of tropical cyclone storm surges using high-resolution forecasts. Climate Dynamics, 52(7), 5031–5044. https://doi.org/10.1007/s00382-018-4430-x

Boschat, G., Pezza, A., Simmonds, I., Perkins, S., Cowan, T., & Purich, A. (2015). Large scale and sub-regional connections in the lead up to summer heat wave and extreme rainfall events in eastern Australia. Climate Dynamics, 44(7), 1823–1840. https://doi.org/10.1007/s00382-014-2214-5

Boumis, G., Moftakhari, H. R., & Moradkhani, H. (2023). Storm surge hazard estimation along the US Gulf Coast: A Bayesian hierarchical approach. Coastal Engineering, 185, 104371. https://doi.org/10.1016/j.coastaleng.2023.104371

Brooks, H. E., Doswell, C. A., & Cooper, J. (1994). On the environments of tornadic and nontornadic mesocyclones. Weather and Forecasting, 9(4), 606–618. https://doi.org/10.1175/1520-0434(1994)009<0606:OTEOTA>2.0.CO;2

Bulletin of China marine disaster. (2023). Bulletin of China marine disaster (2012–2022). Ministry of Natural Resources of the People's Republic of China, available at: http://www.mnr.gov.cn/sj/sjfw/hy/gbgg/zghyzhgb/ , last access: 11 April 2023.

Buzan, J. R., Oleson, K., & Huber, M. (2015). Implementation and comparison of a suite of heat stress metrics within the Community Land Model version 4.5. Geoscientific Model Development, 8(2), 151–170. https://doi.org/10.5194/gmd-8-151-2015

Calafat, F. M., & Marcos, M. (2020). Probabilistic reanalysis of storm surge extremes in Europe. Proceedings of the National Academy of Sciences, 117(4), 1877–1883. https://doi.org/10.1073/pnas.1913049117

Calafat, F. M., Wahl, T., Tadesse, M. G., & Sparrow, S. N. (2022). Trends in Europe storm surge extremes match the rate of sea-level rise. Nature, 603(7903), 841–845. https://doi.org/10.1038/s41586-022-04426-5

Cappucci, M. (2019). Storms deluge New York city, abruptly ending sweltering heat wave, available at: https://www.washingtonpost.com/weather/2019/07/23/flooding-rain-deluges-new-york-city-abruptly-ending-sweltering-heat-wave/, last access: 25 April 2022.

Casanueva, A., Kotlarski, S., Herrera, S., Fernández, J., Gutiérrez, J. M., Boberg, F., et al. (2016). Daily precipitation statistics in a EURO-CORDEX RCM ensemble: added value of raw and bias-corrected high-resolution simulations. Climate Dynamics, 47(3), 719–737. https://doi.org/10.1007/s00382-015-2865-x

Chang, C., Lei, Y., Sui, C., Lin, X., & Ren, F. (2012). Tropical cyclone and extreme rainfall trends in East Asian summer monsoon since mid-20th century. Geophysical Research Letters, 39(18). https://doi.org/10.1029/2012GL052945

Chatlani, S., & Madden, P. (2021). 9 dead from excessive heat in New Orleans in wake of Hurricane Ida. Retrieved May 26, 2022, from https://www.wwno.org/news/2021-09-08/11-dead-from-excessive-heat-in-new-orleans-in-wake-of-hurricane-ida

Chen, H., Wang, S., & Wang, Y. (2020a). Exploring Abrupt Alternations Between Wet and Dry Conditions on the Basis of Historical Observations and Convection-Permitting Climate Model Simulations. Journal of Geophysical Research: Atmospheres, 125(9), e2019JD031982. https://doi.org/10.1029/2019JD031982

Chen, J., Dai, A., Zhang, Y., & Rasmussen, K. L. (2020b). Changes in convective available potential energy and convective inhibition under global warming. Journal of Climate, 33(6), 2025–2050. https://doi.org/10.1175/JCLI-D-19-0461.1

Chen, Y., Liao, Z., Shi, Y., Tian, Y., & Zhai, P. (2021). Detectable increases in sequential flood-heatwave events across China during 1961–2018. Geophysical Research Letters, 48(6), e2021GL092549. https://doi.org/10.1029/2021GL092549

Cid, A., Camus, P., Castanedo, S., Méndez, F. J., & Medina, R. (2017). Global reconstructed daily surge levels from the 20th Century Reanalysis (1871–2010). Global and Planetary Change, 148, 9–21. https://doi.org/10.1016/j.gloplacha.2016.11.006

Cid, A., Wahl, T., Chambers, D. P., & Muis, S. (2018). Storm surge reconstruction and return water level estimation in Southeast Asia for the 20th century. Journal of Geophysical Research: Oceans, 123(1), 437–451. https://doi.org/10.1002/2017JC013143

Coles, S., Heffernan, J., & Tawn, J. (1999). Dependence Measures for Extreme Value Analyses. Extremes, 2(4), 339–365. https://doi.org/10.1023/A:1009963131610

Cowan, T., Wheeler, M. C., Alves, O., Narsey, S., de Burgh-Day, C., Griffiths, M., et al. (2019). Forecasting the extreme rainfall, low temperatures, and strong winds associated with the northern Queensland floods of February 2019. Weather and Climate Extremes, 26, 100232. https://doi.org/10.1016/j.wace.2019.100232

Davies-Jones, R. (2008). An efficient and accurate method for computing the wet-bulb temperature along pseudoadiabats. Monthly Weather Review, 136(7), 2764–2785. https://doi.org/10.1175/2007MWR2224.1

Day, J. A., Fung, I., & Liu, W. (2018). Changing character of rainfall in eastern China, 1951–2007. Proceedings of the National Academy of Sciences, 115(9), 2016–2021. https://doi.org/10.1073/pnas.1715386115

De Dominicis, M., Wolf, J., van Hespen, R., Zheng, P., & Hu, Z. (2023). Mangrove forests can be an effective coastal defence in the Pearl River Delta, China. Communications Earth & Environment, 4(1), 1–13. https://doi.org/10.1038/s43247-022-00672-7

De Ruiter, M. C., Couasnon, A., Homberg, M. J. C., Daniell, J. E., Gill, J. C., & Ward, P. J. (2020). Why we can no longer ignore consecutive disasters. Earth's Future, 8(3). https://doi.org/10.1029/2019EF001425

Deltares, D. (2013). Delft3D-FLOW Simulation of multi-dimensional hydrodynamic flows and transport phenomena, including sediments. Delft Hydraulics, Delft.

Deng, K., Jiang, X., Hu, C., & Chen, D. (2020). More frequent summer heat waves in southwestern China linked to the recent declining of Arctic sea ice. Environmental Research Letters, 15(7), 074011. https://doi.org/10.1088/1748-9326/ab8335

Donat, M. G., Lowry, A. L., Alexander, L. V., O'Gorman, P. A., & Maher, N. (2016). More extreme precipitation in the world's dry and wet regions. Nature Climate Change, 6(5), 508–513. https://doi.org/10.1038/nclimate2941

Donges, J. F., Schleussner, C. F., Siegmund, J. F., & Donner, R. V. (2016). Event coincidence analysis for quantifying statistical interrelationships between event time series. The European Physical Journal Special Topics, 225(3), 471–487. https://doi.org/10.1140/epjst/e2015-50233-y

Duethmann, D., Blöschl, G., & Parajka, J. (2020). Why does a conceptual hydrological model fail to correctly predict discharge changes in response to climate change? Hydrology and Earth System Sciences, 24(7), 3493–3511. https://doi.org/10.5194/hess-24-3493-2020

Emanuel, K. (2003). Tropical Cyclones. Annual Review of Earth and Planetary Sciences, 31(1), 75–104. https://doi.org/10.1146/annurev.earth.31.100901.141259

Fang, J., Wahl, T., Fang, J., Sun, X., Kong, F., & Liu, M. (2021). Compound flood potential from storm surge and heavy precipitation in coastal China: dependence, drivers, and impacts. Hydrology and Earth System Sciences, 25(8), 4403–4416. https://doi.org/10.5194/hess-25-4403-2021

Feng, D., Tan, Z., Xu, D., & Leung, L. R. (2023). Understanding the compound flood risk along the coast of the contiguous United States. Hydrology and Earth System Sciences, 27(21), 3911–3934. https://doi.org/10.5194/hess-27-3911-2023

Fernández-Montblanc, T., Vousdoukas, M. I., Ciavola, P., Voukouvalas, E., Mentaschi, L., Breyiannis, G., et al. (2019). Towards robust pan-European storm surge forecasting. Ocean Modelling, 133, 129–144. https://doi.org/10.1016/j.ocemod.2018.12.001

Fischer, E. M., Seneviratne, S. I., Lüthi, D., & Schär, C. (2007). Contribution of land-atmosphere coupling to recent European summer heat waves. Geophysical Research Letters, 34(6). https://doi.org/10.1029/2006GL029068

Fischer, E. M., Sippel, S., & Knutti, R. (2021). Increasing probability of record-shattering climate extremes. Nature Climate Change, 1–7. https://doi.org/10.1038/s41558-021-01092-9

Fotheringham, A. S., Brunsdon, C., & Charlton, M. (2002). Geographically weighted regression: the analysis of spatially varying relationships. Wiley.

Fowler, H. J., Lenderink, G., Prein, A. F., Westra, S., Allan, R. P., Ban, N., et al. (2021). Anthropogenic intensification of short-duration rainfall extremes. Nature Reviews Earth & Environment, 1–16. https://doi.org/10.1038/s43017-020-00128-6

Gallien, T. W., Kalligeris, N., Delisle, M.-P. C., Tang, B.-X., Lucey, J. T. D., & Winters, M. A. (2018). Coastal Flood Modeling Challenges in Defended Urban Backshores. Geosciences, 8(12), 450. https://doi.org/10.3390/geosciences8120450

Gao, L., Du, H., Huang, H., Zhang, L., & Zhang, P. (2023). Modelling the compound floods upon combined rainfall and storm surge events in a low-lying coastal city. Journal of Hydrology, 627, 130476. https://doi.org/10.1016/j.jhydrol.2023.130476

Giorgi, F., Im, E.-S., Coppola, E., Diffenbaugh, N. S., Gao, X. J., Mariotti, L., & Shi, Y. (2011). Higher hydroclimatic intensity with global warming. Journal of Climate, 24(20), 5309–5324. https://doi.org/10.1175/2011JCLI3979.1

Grimaldi, S., Schumann, G. J.-P., Shokri, A., Walker, J. P., & Pauwels, V. R. N. (2019). Challenges, opportunities, and pitfalls for global coupled hydrologic-hydraulic modeling of floods. Water Resources Research, 55(7), 5277–5300. https://doi.org/10.1029/2018WR024289

Grossiord, C., Buckley, T. N., Cernusak, L. A., Novick, K. A., Poulter, B., Siegwolf, R. T. W., et al. (2020). Plant responses to rising vapor pressure deficit. New Phytologist, 226(6), 1550–1566. https://doi.org/10.1111/nph.16485

Gu, L., Chen, J., Yin, J., Slater, L. J., Wang, H.-M., Guo, Q., et al. (2022). Global increases in compound flood-hot extreme hazards under climate warming. Geophysical Research Letters, 49(8), e2022GL097726. https://doi.org/10.1029/2022GL097726

Haigh, I. D., Marcos, M., Talke, S. A., Woodworth, P. L., Hunter, J. R., Hague, B. S., et al. (2021). GESLA Version 3: A major update to the global higher-frequency sea-level dataset. Geoscience Data Journal, n/a(n/a). https://doi.org/10.1002/gdj3.174

Hart, R. E., Maue, R. N., & Watson, M. C. (2007). Estimating local memory of tropical cyclones through MPI anomaly evolution. Monthly Weather Review, 135(12), 3990–4005. https://doi.org/10.1175/2007MWR2038.1

He, X., & Sheffield, J. (2020). Lagged compound occurrence of droughts and pluvials globally over the past seven decades. Geophysical Research Letters, 47(14), e2020GL087924. https://doi.org/10.1029/2020GL087924

He, Y. H., Mok, H. Y., & Lai, E. S. T. (2016). Projection of sea-level change in the vicinity of Hong Kong in the 21st century. International Journal of Climatology, 36(9), 3237–3244. https://doi.org/10.1002/joc.4551

Held, I. M., & Soden, B. J. (2006). Robust responses of the hydrological cycle to global warming. Journal of Climate, 19(21), 5686–5699. https://doi.org/10.1175/JCLI3990.1

Hersbach, H., Bell, B., Berrisford, P., Hirahara, S., Horányi, A., Muñoz-Sabater, J., et al. (2020). The ERA5 global reanalysis. Quarterly Journal of the Royal Meteorological Society, 146(730), 1999–2049. https://doi.org/10.1002/qj.3803

Hong Kong Observatory. (2012). Typhoon 5-6 (Average Number of Tropical Cyclones), available at https://www.hko.gov.hk/en/education/tropical-cyclone/forecasting/00161-typhoon-56-average-number-of-tropical-cyclones.html. Retrieved February 29, 2024, from

Hong Kong Observatory. (2023). Climate Change in Hong Kong - Mean sea level, available at https://www.hko.gov.hk/en/climate_change/obs_hk_sea_level.htm. Retrieved February 29, 2024, from https://www.hko.gov.hk/en/climate_change/obs_hk_sea_level.htm

Hotelling, H. (1933). Analysis of a complex of statistical variables into principal components. Journal of Educational Psychology, 24(6), 417–441. https://doi.org/10.1037/h0071325

Houze Jr., R. A. (2012). Orographic effects on precipitating clouds. Reviews of Geophysics, 50(1). https://doi.org/10.1029/2011RG000365

Howard, T., Lowe, J., & Horsburgh, K. (2010). Interpreting century-scale changes in Southern North Sea storm surge climate derived from coupled model simulations. Journal of Climate, 23(23), 6234–6247. https://doi.org/10.1175/2010JCLI3520.1

Issa, A., Ramadugu, K., Mulay, P., Hamilton, J., Siegel, V., Harrison, C., et al. (2018). Deaths related to Hurricane Irma — Florida, Georgia, and North Carolina, September 4–October 10, 2017. MMWR. Morbidity and Mortality Weekly Report, 67(30), 829–832. https://doi.org/10.15585/mmwr.mm6730a5

ITV Weather. (2020). Two months' rain could fall in three hours as heatwave triggers thunderstorms, available at: https://www.itv.com/news/2020-08-10/two-months-rain-could-fall-in-three-hours-as-heatwave-triggers-thunderstorms, last access: 25 April 2022.

Jafarzadegan, K., Moradkhani, H., Pappenberger, F., Moftakhari, H., Bates, P., Abbaszadeh, P., et al. (2023). Recent advances and new frontiers in riverine and coastal flood modeling. Reviews of Geophysics, 61(2), e2022RG000788. https://doi.org/10.1029/2022RG000788

Jane, R., Cadavid, L., Obeysekera, J., & Wahl, T. (2020). Multivariate statistical modelling of the drivers of compound flood events in south Florida. Natural Hazards and Earth System Sciences, 20(10), 2681–2699. https://doi.org/10.5194/nhess-20-2681-2020

Ji, T., Li, G., Liu, Y., Liu, R., & Zhu, Y. (2021). Spatiotemporal features of storm surge activity and its response to climate change in the southeastern coastal area of China in the past 60 years. Journal of Geophysical Research: Atmospheres, 126(4), e2020JD033234. https://doi.org/10.1029/2020JD033234

Kalnay, E., Kanamitsu, M., Kistler, R., Collins, W., Deaven, D., Gandin, L., et al. (1996). The NCEP/NCAR 40-Year Reanalysis Project. Bulletin of the American Meteorological Society, 77(3), 437–472. https://doi.org/10.1175/1520-0477(1996)077<0437:TNYRP>2.0.CO;2

Kawase, H., Imada, Y., Tsuguti, H., Nakaegawa, T., Seino, N., Murata, A., & Takayabu, I. (2020). The heavy rain event of July 2018 in Japan enhanced by historical warming. Bulletin of the American Meteorological Society, 101(1), S109–S114. https://doi.org/10.1175/BAMS-D-19-0173.1

Kendall, M. G. (1975). Rank correlation methods (4th ed., 2d impression). London: Griffin.

Krige DG. (1951). A statistical approach to some basic mine valuation problems on the Witwatersrand. Journal of the Chemical, Metallurgical and Mining Society of South Africa, December, 119–139

Kulp, S. A., & Strauss, B. H. (2019). New elevation data triple estimates of global vulnerability to sea-level rise and coastal flooding. Nature Communications, 10(1), 4844. https://doi.org/10.1038/s41467-019-12808-z

Kyprioti, A. P., Adeli, E., Taflanidis, A. A., Westerink, J. J., & Tolman, H. L. (2021). Probabilistic storm surge estimation for landfalling hurricanes: advancements in computational efficiency using Quasi-Monte Carlo techniques. Journal of Marine Science and Engineering, 9(12), 1322. https://doi.org/10.3390/jmse9121322

Lai, Y., Li, J., Chen, Y. D., Chan, F. K. S., Gu, X., & Huang, S. (2023). Compound floods in Hong Kong: Hazards, triggers, and socio-economic consequences. Journal of Hydrology: Regional Studies, 46, 101321. https://doi.org/10.1016/j.ejrh.2023.101321

Lau, W. K. M., & Kim, K.-M. (2012). The 2010 Pakistan flood and Russian heat wave: teleconnection of hydrometeorological extremes. Journal of Hydrometeorology, 13(1), 392–403. https://doi.org/10.1175/JHM-D-11-016.1

Lenderink, G., Barbero, R., Loriaux, J. M., & Fowler, H. J. (2017). Super-Clausius–Clapeyron scaling of extreme hourly convective precipitation and its relation to large-scale atmospheric conditions. Journal of Climate, 30(15), 6037–6052. https://doi.org/10.1175/JCLI-D-16-0808.1

Lepore, C., Veneziano, D., & Molini, A. (2015). Temperature and CAPE dependence of rainfall extremes in the eastern United States. Geophysical Research Letters, 42(1), 74–83. https://doi.org/10.1002/2014GL062247

Li, M., Yao, Y., Luo, D., & Zhong, L. (2019). The linkage of the large-scale circulation pattern to a long-lived heatwave over mideastern China in 2018. Atmosphere, 10(2), 89. https://doi.org/10.3390/atmos10020089

Li, Z., He, Y., Wang, P., Theakstone, W. H., An, W., Wang, X., et al. (2012). Changes of daily climate extremes in southwestern China during 1961–2008. Global and Planetary Change, 80–81, 255–272. https://doi.org/10.1016/j.gloplacha.2011.06.008

Liang, M. S., & Julius, S. (2017). On the coastal topography and storm surge for infrastructure risk assessment and adaptation, 232–240. https://doi.org/10.1061/9780784480618.023

Liao, Z., Chen, Y., Li, W., & Zhai, P. (2021). Growing threats from unprecedented sequential flood-hot extremes across China. Geophysical Research Letters, 48(18), e2021GL094505. https://doi.org/10.1029/2021GL094505

Liu, M., Yin, Y., Wang, X., Ma, X., Chen, Y., & Chen, W. (2022). More frequent, long-lasting, extreme and postponed compound drought and hot events in eastern China. Journal of Hydrology, 614, 128499. https://doi.org/10.1016/j.jhydrol.2022.128499

Liu, X., Tang, Q., Liu, W., Yang, H., Groisman, P., Leng, G., et al. (2019). The asymmetric impact of abundant preceding rainfall on heat stress in low latitudes. Environmental Research Letters, 14(4), 044010. https://doi.org/10.1088/1748-9326/ab018a

Liu, X., Tang, Q., Zhang, X., Groisman, P., Sun, S., Lu, H., & Li, Z. (2017). Spatially distinct effects of preceding precipitation on heat stress over eastern China. Environmental Research Letters, 12(11), 115010. https://doi.org/10.1088/1748-9326/aa88f8

Lu, E. (2009). Determining the start, duration, and strength of flood and drought with daily precipitation: Rationale. Geophysical Research Letters, 36(12). https://doi.org/10.1029/2009GL038817

Luettich, R. A. (Richard A., Westerink, J. J., & Scheffner, N. W. (1992). ADCIRC : an advanced three-dimensional circulation model for shelves, coasts, and estuaries. Report 1, Theory and methodology of ADCIRC-2DD1 and ADCIRC-3DL (Report). This Digital Resource was created from scans of the Print Resource. Coastal Engineering Research Center (U.S.). Retrieved from https://erdc-library.erdc.dren.mil/jspui/handle/11681/4618

Mann, H. B. (1945). Nonparametric tests against trend. Econometrica: Journal of the Econometric Society, 245–259.

Martin, E. R. (2018). Future projections of global pluvial and drought event characteristics. Geophysical Research Letters, 45(21), 11,913-11,920. https://doi.org/10.1029/2018GL079807

Martzikos, N. T., Prinos, P. E., Memos, C. D., & Tsoukala, V. K. (2021). Key research issues of coastal storm analysis. Ocean & Coastal Management, 199, 105389. https://doi.org/10.1016/j.ocecoaman.2020.105389

Massmann, A., Gentine, P., & Lin, C. (2019). When Does Vapor Pressure Deficit Drive or Reduce Evapotranspiration? Journal of Advances in Modeling Earth Systems, 11(10), 3305–3320. https://doi.org/10.1029/2019MS001790

Matos, J. P., Ferreira, F., Mendes, D., & Matos, J. S. (2023). Evaluating Compound Flooding Risks in Coastal Cities under Climate Change—The Maputo Case Study, in Mozambique. Sustainability, 15(19), 14497. https://doi.org/10.3390/su151914497

Matthews, T., Byrne, M., Horton, R., Murphy, C., Pielke Sr, R., Raymond, C., et al. (2022). Latent heat must be visible in climate communications. WIREs Climate Change, e779. https://doi.org/10.1002/wcc.779

Matthews, T., Wilby, R. L., & Murphy, C. (2019). An emerging tropical cyclone–deadly heat compound hazard. Nature Climate Change, 9(8), 602–606. https://doi.org/10.1038/s41558-019-0525-6

Min, S.-K., Jo, S.-Y., Seong, M.-G., Kim, Y.-H., Son, S.-W., Byun, Y.-H., et al. (2022). Human contribution to the 2020 summer successive hot-wet extremes in South Korea. Bulletin of the American Meteorological Society, 8. https://doi.org/10.1175/BAMS-D-21-0144.1

Moftakhari, H. R., Salvadori, G., AghaKouchak, A., Sanders, B. F., & Matthew, R. A. (2017). Compounding effects of sea level rise and fluvial flooding. Proceedings of the National Academy of Sciences. https://doi.org/10.1073/pnas.1620325114

Molnar, P., Fatichi, S., Gaál, L., Szolgay, J., & Burlando, P. (2015). Storm type effects on super Clausius-Clapeyron scaling of intense rainstorm properties with air temperature. Hydrology and Earth System Sciences, 19, 1753–1766. https://doi.org/10.5194/hess-19-1753-2015

Mora, C., Dousset, B., Caldwell, I. R., Powell, F. E., Geronimo, R. C., Bielecki, C. R., et al. (2017). Global risk of deadly heat. Nature Climate Change, 7(7), 501–506. https://doi.org/10.1038/nclimate3322

Muis, S., Apecechea, M. I., Dullaart, J., de Lima Rego, J., Madsen, K. S., Su, J., et al. (2020). A high-resolution global dataset of extreme sea levels, tides, and storm surges, including future projections. Frontiers in Marine Science, 7. https://doi.org/10.3389/fmars.2020.00263

Muis, S., Verlaan, M., Winsemius, H. C., Aerts, J. C. J. H., & Ward, P. J. (2016). A global reanalysis of storm surges and extreme sea levels. Nature Communications, 7(1), 11969. https://doi.org/10.1038/ncomms11969

Mukherjee, S., & Mishra, A. K. (2021). Increase in compound drought and heatwaves in a warming world. Geophysical Research Letters, 48(1), e2020GL090617. https://doi.org/10.1029/2020GL090617

Nelsen, R. B. (2006). An Introduction to copulas. New York, NY: Springer. https://doi.org/10.1007/0-387-28678-0

Novick, K. A., Ficklin, D. L., Stoy, P. C., Williams, C. A., Bohrer, G., Oishi, A. C., et al. (2016). The increasing importance of atmospheric demand for ecosystem water and carbon fluxes. Nature Climate Change, 6(11), 1023–1027. https://doi.org/10.1038/nclimate3114

Parker, T. J., Berry, G. J., & Reeder, M. J. (2013). The influence of tropical cyclones on heat waves in Southeastern Australia. Geophysical Research Letters, 40(23), 6264–6270. https://doi.org/10.1002/2013GL058257

Pawlowicz, R., Beardsley, B., & Lentz, S. (2002). Classical tidal harmonic analysis including error estimates in MATLAB using T_TIDE. Computers & Geosciences, 28(8), 929–937. https://doi.org/10.1016/S0098-3004(02)00013-4

Perkins, S. E., & Alexander, L. V. (2013). On the measurement of heat waves. Journal of Climate, 26(13), 4500–4517. https://doi.org/10.1175/JCLI-D-12-00383.1

Perkins-Kirkpatrick, S. E., & Lewis, S. C. (2020). Increasing trends in regional heatwaves. Nature Communications, 11(1), 3357. https://doi.org/10.1038/s41467-020-16970-7

Petoukhov, V., Rahmstorf, S., Petri, S., & Schellnhuber, H. J. (2013). Quasiresonant amplification of planetary waves and recent Northern Hemisphere weather extremes. Proceedings of the National Academy of Sciences, 110(14), 5336–5341. https://doi.org/10.1073/pnas.1222000110

Qiang, Y., He, J., Xiao, T., Lu, W., Li, J., & Zhang, L. (2021). Coastal town flooding upon compound rainfall-wave overtopping-storm surge during extreme tropical cyclones in Hong Kong. Journal of Hydrology: Regional Studies, 37, 100890. https://doi.org/10.1016/j.ejrh.2021.100890

Raghavendra, A., Dai, A., Milrad, S. M., & Cloutier-Bisbee, S. R. (2019). Floridian heatwaves and extreme precipitation: future climate projections. Climate Dynamics, 52(1), 495–508. https://doi.org/10.1007/s00382-018-4148-9

Ramos-Valle, A. N., Curchitser, E. N., & Bruyère, C. L. (2020). Impact of tropical cyclone landfall angle on storm surge along the Mid-Atlantic Bight. Journal of Geophysical Research: Atmospheres, 125(4), e2019JD031796. https://doi.org/10.1029/2019JD031796

Randall, D. A., Cess, R. D., Blanchet, J. P., Boer, G. J., Dazlich, D. A., Genio, A. D. D., et al. (1992). Intercomparison and interpretation of surface energy fluxes in atmospheric general

circulation models. Journal of Geophysical Research: Atmospheres, 97(D4), 3711–3724. https://doi.org/10.1029/91JD03120

Raymond, C., Horton, R. M., Zscheischler, J., Martius, O., AghaKouchak, A., Balch, J., et al. (2020). Understanding and managing connected extreme events. Nature Climate Change, 10(7), 611–621. https://doi.org/10.1038/s41558-020-0790-4

Raymond, C., Matthews, T., & Horton, R. M. (2020). The emergence of heat and humidity too severe for human tolerance. Science Advances, 6(19), eaaw1838. https://doi.org/10.1126/sciadv.aaw1838

Raymond, C., Matthews, T., Horton, R. M., Fischer, E. M., Fueglistaler, S., Ivanovich, C., et al. (2021). On the controlling factors for globally extreme humid heat. Geophysical Research Letters, 48(23), e2021GL096082. https://doi.org/10.1029/2021GL096082

Reich, B. J., & Shaby, B. A. (2012). A hierarchical max-stable spatial model for extreme precipitation. The Annals of Applied Statistics, 6(4), 1430–1451. https://doi.org/10.1214/12-AOAS591

Ridder, N. N., Pitman, A. J., Westra, S., Ukkola, A., Hong, X. D., Bador, M., et al. (2020). Global hotspots for the occurrence of compound events. Nature Communications, 11(1), 5956. https://doi.org/10.1038/s41467-020-19639-3

Santiago-Collazo, F. L., Bilskie, M. V., & Hagen, S. C. (2019). A comprehensive review of compound inundation models in low-gradient coastal watersheds. Environmental Modelling & Software, 119, 166–181. https://doi.org/10.1016/j.envsoft.2019.06.002

Seeley, J. T., & Romps, D. M. (2015). Why does tropical convective available potential energy (CAPE) increase with warming? Geophysical Research Letters, 42(23), 10,429-10,437. https://doi.org/10.1002/2015GL066199

Shang, W., Ren, X., Duan, K., & Zhao, C. (2020). Influence of the South Asian high-intensity variability on the persistent heavy rainfall and heat waves in Asian monsoon regions. International Journal of Climatology, 40(4), 2153–2172. https://doi.org/10.1002/joc.6324

Shepard, D. (1968). A two-dimensional interpolation function for irregularly-spaced data. In Proceedings of the 1968 23rd ACM national conference, 517-524.

Shimpo, A., Takemura, K., Wakamatsu, S., Togawa, H., Mochizuki, Y., Takekawa, M., et al. (2019). Primary factors behind the heavy rain event of July 2018 and the subsequent heat wave in Japan. Sola, advpub. https://doi.org/10.2151/sola.15A-003

Shimura, T., Pringle, W. J., Mori, N., Miyashita, T., & Yoshida, K. (2022). Seamless projections of global storm surge and ocean waves under a warming climate. Geophysical Research Letters, 49(6), e2021GL097427. https://doi.org/10.1029/2021GL097427

Siegmund, J. F., Siegmund, N., & Donner, R. V. (2017). CoinCalc—A new R package for quantifying simultaneities of event series. Computers & Geosciences, 98, 64–72. https://doi.org/10.1016/j.cageo.2016.10.004

Skarha, J., Gordon, L., Sakib, N., June, J., Jester, D. J., Peterson, L. J., et al. (2021). Association of power outage with mortality and hospitalizations among Florida nursing home residents after hurricane Irma. JAMA Health Forum, 2(11), e213900. https://doi.org/10.1001/jamahealthforum.2021.3900

Sklar, M. (1959). Fonctions de répartition à N dimensions et leurs marges. Publications Del'institut De Statistique De L'université De Paris 8:229–231

Small, C., & Nicholls, R. J. (2003). A Global Analysis of Human Settlement in Coastal Zones. Journal of Coastal Research, 19(3), 584–599.

Speizer, S., Raymond, C., Ivanovich, C., & Horton, R. M. (2022). Concentrated and intensifying humid heat extremes in the IPCC AR6 Regions. Geophysical Research Letters, 49(5), e2021GL097261. https://doi.org/10.1029/2021GL097261

Sukhovey, V. F., & Camara, T. (1995). Thermal advection in the tropical Atlantic upper layer. Physical Oceanography, 6(6), 399–410. https://doi.org/10.1007/BF02197465

Sun, H., Zhang, X., Ruan, X., Jiang, H., & Shou, W. (2024). Mapping Compound Flooding Risks for Urban Resilience in Coastal Zones: A Comprehensive Methodological Review. Remote Sensing, 16(2), 350. https://doi.org/10.3390/rs16020350

Sun, Q., Miao, C., AghaKouchak, A., & Duan, Q. (2017). Unraveling anthropogenic influence on the changing risk of heat waves in China. Geophysical Research Letters, 44(10), 5078–5085. https://doi.org/10.1002/2017GL073531

Sun, Q., Miao, C., Duan, Q., Ashouri, H., Sorooshian, S., & Hsu, K.-L. (2018). A Review of Global Precipitation Data Sets: Data Sources, Estimation, and Intercomparisons. Reviews of Geophysics, 56(1), 79–107. https://doi.org/10.1002/2017RG000574

Sun, Q., Zhang, X., Zwiers, F., Westra, S., & Alexander, L. V. (2021). A global, continental, and regional analysis of changes in extreme precipitation. Journal of Climate, 34(1), 243–258. https://doi.org/10.1175/JCLI-D-19-0892.1

Swain, D. L., Horton, D. E., Singh, D., & Diffenbaugh, N. S. (2016). Trends in atmospheric patterns conducive to seasonal precipitation and temperature extremes in California. Science Advances, 2(4), e1501344. https://doi.org/10.1126/sciadv.1501344

Tadesse, M., & Wahl, T. (2021). A database of global storm surge reconstructions. Scientific Data, 8(1), 125. https://doi.org/10.1038/s41597-021-00906-x

Tadesse, M., Wahl, T., & Cid, A. (2020). Data-driven modeling of global storm surges. Frontiers in Marine Science, 7. https://doi.org/10.3389/fmars.2020.00260

Talke, S. A., Familkhalili, R., & Jay, D. A. (2021). The Influence of Channel Deepening on Tides, River Discharge Effects, and Storm Surge. Journal of Geophysical Research: Oceans, 126(5), e2020JC016328. https://doi.org/10.1029/2020JC016328

Tao, S., & Ding, Y. (1981). Observational evidence of the influence of the Qinghai-Xizang (Tibet) Plateau on the occurrence of heavy rain and severe convective storms in China. Bulletin of the American Meteorological Society, 62(1), 23–30. https://doi.org/10.1175/1520-0477(1981)062<0023:OEOTIO>2.0.CO;2

Tellman, B., Sullivan, J. A., Kuhn, C., Kettner, A. J., Doyle, C. S., Brakenridge, G. R., et al. (2021). Satellite imaging reveals increased proportion of population exposed to floods. Nature, 596(7870), 80–86. https://doi.org/10.1038/s41586-021-03695-w

Teuling, A. J., Van Loon, A. F., Seneviratne, S. I., Lehner, I., Aubinet, M., Heinesch, B., et al. (2013). Evapotranspiration amplifies European summer drought. Geophysical Research Letters, 40(10), 2071–2075. https://doi.org/10.1002/grl.50495

Toyoda, M., Mori, N., Kim, S., Shibutani, Y., & Yoshino, J. (2023). Assessment of compound occurrence of storm surge and river flood in Ise and Mikawa Bays, Japan using a framework of atmosphere–ocean–river coupling. Natural Hazards. https://doi.org/10.1007/s11069-023-06362-7

Trenberth, K. E., Dai, A., Rasmussen, R. M., & Parsons, D. B. (2003). The changing character of precipitation. Bulletin of the American Meteorological Society, 84(9), 1205–1218. https://doi.org/10.1175/BAMS-84-9-1205

UNDRR, & CRED. (2020). Human cost of disasters: An overview of the last 20 years, 2000-2019. UN Office for Disaster Risk Reduction (UNDRR), Centre for Research on the Epidemiology of Disaster (CRED).

Utsumi, N., Seto, S., Kanae, S., Maeda, E. E., & Oki, T. (2011). Does higher surface temperature intensify extreme precipitation? Geophysical Research Letters, 38(16). https://doi.org/10.1029/2011GL048426

Ventura, V., Paciorek, C. J., & Risbey, J. S. (2004). Controlling the proportion of falsely rejected hypotheses when conducting multiple tests with climatological data. Journal of Climate, 17(22), 4343–4356. https://doi.org/10.1175/3199.1

Vogel, R. M., & Shallcross, A. L. (1996). The moving blocks bootstrap versus parametric time series models. Water Resources Research, 32(6), 1875–1882. https://doi.org/10.1029/96WR00928

Wahl, T., Jain, S., Bender, J., Meyers, S. D., & Luther, M. E. (2015). Increasing risk of compound flooding from storm surge and rainfall for major US cities. Nature Climate Change, 5(12), 1093–1097. https://doi.org/10.1038/nclimate2736

Wallace, J. M. (1975). Diurnal variations in precipitation and thunderstorm frequency over the conterminous United States. Monthly Weather Review, 103(5), 406–419. https://doi.org/10.1175/1520-0493(1975)103<0406:DVIPAT>2.0.CO;2

Wang, G., Wang, D., Trenberth, K. E., Erfanian, A., Yu, M., Bosilovich, M. G., & Parr, D. T. (2017). The peak structure and future changes of the relationships between extreme precipitation and temperature. Nature Climate Change, 7(4), 268–274. https://doi.org/10.1038/nclimate3239

Wang, J., & Liu, P. L.-F. (2021). Numerical study on impacts of a concurrent storm-tide-tsunami event in Macau and Hong Kong. Coastal Engineering, 170, 104000. https://doi.org/10.1016/j.coastaleng.2021.104000

Wang, K., Yang, Y., Reniers, G., & Huang, Q. (2021a). A study into the spatiotemporal distribution of typhoon storm surge disasters in China. Natural Hazards, 108(1), 1237–1256. https://doi.org/10.1007/s11069-021-04730-9

Wang, P., Yang, Y., Tang, J., Leung, L. R., & Liao, H. (2021b). Intensified humid heat events under global warming. Geophysical Research Letters, 48(2), e2020GL091462. https://doi.org/10.1029/2020GL091462

Wang, S. S. Y., Kim, H., Coumou, D., Yoon, J.-H., Zhao, L., & Gillies, R. R. (2019). Consecutive extreme flooding and heat wave in Japan: Are they becoming a norm? Atmospheric Science Letters, 20(10), e933. https://doi.org/10.1002/asl.933

Wang, S., Jiao, S., & Xin, H. (2013). Spatio-temporal characteristics of temperature and precipitation in Sichuan Province, Southwestern China, 1960–2009. Quaternary International, 286, 103–115. https://doi.org/10.1016/j.quaint.2012.04.030

Wang, Z., Yang, S., Duan, A., Hua, W., Ullah, K., & Liu, S. (2019). Tibetan Plateau heating as a driver of monsoon rainfall variability in Pakistan. Climate Dynamics, 52(9), 6121–6130. https://doi.org/10.1007/s00382-018-4507-6

Wasko, C. (2021). Review: can temperature be used to inform changes to flood extremes with global warming? Philosophical Transactions of the Royal Society A: Mathematical, Physical and Engineering Sciences, 379(2195), 20190551. https://doi.org/10.1098/rsta.2019.0551

Weaver, R. J., & Slinn, D. N. (2010). Influence of bathymetric fluctuations on coastal storm surge. Coastal Engineering, 57(1), 62–70. https://doi.org/10.1016/j.coastaleng.2009.09.012

WEF. (2020). The Global Risks Report 2020, available at: https://www.weforum.org/reports/the-global-risks-report-2020, last access: 25 December 2023.

Wilks, D. S. (1997). Resampling hypothesis tests for autocorrelated fields. Journal of Climate, 10(1), 65–82. https://doi.org/10.1175/1520-0442(1997)010<0065:RHTFAF>2.0.CO;2

Wilks, D. S. (2006). On "field significance" and the false discovery rate. Journal of Applied Meteorology and Climatology, 45(9), 1181–1189. https://doi.org/10.1175/JAM2404.1

Wilks, D. S. (2016). "The stippling shows statistically significant grid points": how research results are routinely overstated and overinterpreted, and what to do about it. Bulletin of the American Meteorological Society, 97(12), 2263–2273. https://doi.org/10.1175/BAMS-D-15-00267.1

Wong, M. C., Mok, H. Y., & Lee, T. C. (2011). Observed changes in extreme weather indices in Hong Kong. International Journal of Climatology, 31(15), 2300–2311. https://doi.org/10.1002/joc.2238

Wu, S., Wu, Y., & Wen, J. (2019). Future changes in precipitation characteristics in China. International Journal of Climatology, 39(8), 3558–3573. https://doi.org/10.1002/joc.6038

Xu, K., Wang, C., & Bin, L. (2023). Compound flood models in coastal areas: a review of methods and uncertainty analysis. Natural Hazards, 116(1), 469–496. https://doi.org/10.1007/s11069-022-05683-3

Yin, J., Slater, L., Gu, L., Liao, Z., Guo, S., & Gentine, P. (2022). Global increases in lethal compound heat stress: hydrological drought hazards under cimate change. Geophysical Research Letters, 49(18), e2022GL100880. https://doi.org/10.1029/2022GL100880

You, J., & Wang, S. (2021). Higher probability of occurrence of hotter and shorter heat waves followed by heavy rainfall. Geophysical Research Letters, 48(17), e2021GL094831. https://doi.org/10.1029/2021GL094831

You, J., Wang, S., Zhang, B., Raymond, C., & Matthews, T. (2023). Growing threats from swings between hot and wet extremes in a warmer world. Geophysical Research Letters, 50(14), e2023GL104075. https://doi.org/10.1029/2023GL104075

Yuan, W., Zheng, Y., Piao, S., Ciais, P., Lombardozzi, D., Wang, Y., et al. (2019). Increased atmospheric vapor pressure deficit reduces global vegetation growth. Science Advances, 5(8), eaax1396. https://doi.org/10.1126/sciadv.aax1396

Zhai, P., Zhang, X., Wan, H., & Pan, X. (2005). Trends in total precipitation and frequency of daily precipitation extremes over China. Journal of Climate, 18(7), 1096–1108. https://doi.org/10.1175/JCLI-3318.1

Zhang, B., & Wang, S. (2021). Probabilistic characterization of extreme storm surges induced by tropical cyclones. Journal of Geophysical Research: Atmospheres, 126(3), e2020JD033557. https://doi.org/10.1029/2020JD033557

Zhang, B., Wang, S., & Wang, Y. (2021). Probabilistic projections of multidimensional flood risks at a convection-permitting scale. Water Resources Research, 57(1), e2020WR028582. https://doi.org/10.1029/2020WR028582

Zhang, B., Wang, S., Moradkhani, H., Slater, L., & Liu, J. (2022). A vine copula-based ensemble projection of precipitation intensity–duration–frequency curves at sub-daily to multi-day time scales. Water Resources Research, 58(11), e2022WR032658. https://doi.org/10.1029/2022WR032658

Zhang, W., & Villarini, G. (2020). Deadly compound heat stress-flooding hazard across the central United States. Geophysical Research Letters, 47(15), e2020GL089185. https://doi.org/10.1029/2020GL089185

Zhang, Y. J., Ye, F., Stanev, E. V., & Grashorn, S. (2016). Seamless cross-scale modeling with SCHISM. Ocean Modelling, 102, 64–81. https://doi.org/10.1016/j.ocemod.2016.05.002

Zhang, Y., & Najafi, M. R. (2020). Probabilistic Numerical Modeling of Compound Flooding Caused by Tropical Storm Matthew Over a Data-Scarce Coastal Environment. Water Resources Research, 56(10), e2020WR028565. https://doi.org/10.1029/2020WR028565

Zhao, Y., Zhu, J., & Xu, Y. (2014). Establishment and assessment of the grid precipitation datasets in China for recent 50 years. Journal of the Meteorological Sciences, 34(4), 414-420 (in Chinese). https://doi.org/10.3969/2013jms.0008

Zheng, F., Westra, S., Leonard, M., & Sisson, S. A. (2014). Modeling dependence between extreme rainfall and storm surge to estimate coastal flooding risk. Water Resources Research, 50(3), 2050–2071. https://doi.org/10.1002/2013WR014616

Zhou, S., Williams, A. P., Berg, A. M., Cook, B. I., Zhang, Y., Hagemann, S., et al. (2019). Land–atmosphere feedbacks exacerbate concurrent soil drought and atmospheric aridity. Proceedings of the National Academy of Sciences, 116(38), 18848–18853. https://doi.org/10.1073/pnas.1904955116

Zhou, T., & Yu, R. (2005). Atmospheric water vapor transport associated with typical anomalous summer rainfall patterns in China. Journal of Geophysical Research: Atmospheres, 110(D8). https://doi.org/10.1029/2004JD005413

Zijl, F., Verlaan, M., & Gerritsen, H. (2013). Improved water-level forecasting for the Northwest European Shelf and North Sea through direct modelling of tide, surge and non-linear interaction. Ocean Dynamics, 63(7), 823–847. https://doi.org/10.1007/s10236-013-0624-2

Zscheischler, J., Martius, O., Westra, S., Bevacqua, E., Raymond, C., Horton, R. M., et al. (2020). A typology of compound weather and climate events. Nature Reviews Earth & Environment, 1(7), 333–347. https://doi.org/10.1038/s43017-020-0060-z

Zscheischler, J., Westra, S., van den Hurk, B. J. J. M., Seneviratne, S. I., Ward, P. J., Pitman, A., et al. (2018). Future climate risk from compound events. Nature Climate Change, 8(6), 469–477. https://doi.org/10.1038/s41558-018-0156-3